Experiments on the Formation of Rippled Icicles

by

John Ladan

A thesis submitted in conformity with the requirements
for the degree of Doctor of Philosophy

Department of Physics
University of Toronto

Experiments on the Formation of Rippled Icicles

John Ladan
Doctor of Philosophy

Department of Physics
University of Toronto
2023

Abstract

Icicles are a common sight during winter weather, hanging from rooftops, railings and other structures from which water drips. The long slender shape of an icicle develops through a highly non-equilibrium process in which supercooled water flows down its surface, partially freezing along the way. This is an example of "wet ice growth." The growth rate is dictated by how quickly latent heat released by freezing can be transported away from the ice surface. The cooling of the liquid is greater at the tip, causing the tip to grow faster, leading its elongated form.

Many icicles are observed to have a rippled pattern along their length with a near universal wavelength of 9 mm. Rippled icicles often have a foggy appearance with small bubbles visible in the interior. While measurements of icicle ripples date back to at least 1933, the mechanism through which they form has eluded physicists. It has previously been shown that the existence and amplitude of ripples depends on the presence of impurities in the source water, but no existing model for icicle ripples includes impurities. The problem of how icicle ripples form in the presence of impurities is the focus of this thesis.

A pre-existing model for the rippling instability was extended to include physical effects of impurities. A linear stability analysis was performed on this model, and found that it did not predict ripples. The stability of the model is not sensitive to changes in concentration, so it is unlikely that such a model will ever agree with experiment.

In order to better understand the role of impurities in wet ice formation, we grew icicles using various chemical species as the impurity for concentrations between 0–43.9 mMol/kg. The changes in morphology from impurities were only affected by the molar concentration, showing that icicle ripples are a colligative phenomenon, depending only on the number of molecules.

One of the impurities used was sodium fluorescein, a fluorescent dye that fluoresces when dissolved in water. The liquid flowing down the surface of icicles was observed directly using this dye. Contrary to previous models, we find that the ice is incompletely wetted by the liquid phase, and that the whole process is much more stochastic than has been previously assumed. In addition, the presence of impurities modifies the wetting properties of the ice surface, while the emerging topography interacts with the liquid distribution.

Using the fluorescent dye, we also observed the location of impurities trapped inside of icicles. All of the impurities are found inside small spherical inclusions. The inclusions are organized into chevron patterns aligned with the peaks of the ripples. Within the chevrons, a substructure of layered crescent-shaped structures is observed, suggestive of cyclic wetting and freezing. We also examine the crystal grain structure of laboratory icicles, with and without impurities.

These observations must inform any successful model of an impurity-driven rippling instability. Our results have general implications for the morphological evolution of many natural, gravity-driven, wet ice growth processes.

Acknowledgements

First and foremost, I must acknowledge the patience, guidance and support of my supervisor Stephen Morris. Without his persistence and guidance, none of these insights into icicle growth would exist.

Next, I would like to thank my committee members Nicolas Grisouard and Mathew Wells for their advice. In fact it was Nicolas's suggestion to pursue the surface water experiment in more detail.

I also must acknowledge Dr. Matteo Bertagni and Prof. Carlo Camporeale for the thoughtful discussion and insights into the analysis of the morphological instability problem. Particular thanks is given to Matteo for continuing with the weakly nonlinear analysis presented in his thesis.

Finally I'd like to thank John Wettlaufer, Grae Worster, Andrew Wells, and Lasse Makkonen for showing interest in my research and engaging in thoughtful discussions.

This work was supported by the Natural Sciences and Engineering Research Council of Canada.

Included published work

This thesis includes content that was previously published by the author. The contents of Chapter 6 were published in New Journal of Physics [1] and Chapter 7 was published in Phys. Rev. E [2].

Contents

List of Tables

List of Figures

Listings

Chapter 1

Introduction

Icicles are a common sight in colder climates, hanging from snowy roofs on a sunny day. Their distinctive long slender shape stands out from other ice and snow in urban settings. Icicles in nature may be smooth and transparent, or foggy with a rippled surface. A few examples of rippled icicles are shown in Figure 1.1. While icicles are commonly seen as harmless decoration, they can also become hazardous by weighing down structures like power lines [3], or as falling hazards when they detach. Such structural icing is an important consideration for civil and aerospace engineering [4, 5]. Icicles are also a common feature in marine icing, in which sea spray causes ice accretion on ships and structures. Marine icing poses significant safety concerns for shipping in cold climates [6]. Despite their ubiquity in nature and urban settings, there are still open questions in the physics of icicle formation with impurities. In particular, the mechanism by which ripples form on the surface is unknown. The formation of rippled icicles, and the role of impurities in icicle growth is the focus of this thesis.

Icicles are an example of "wet ice growth", in which liquid water flows and freezes over a growing surface of ice [7]. The morphology of ice formed through wet ice growth presents a challenging free-boundary problem. Wet ice growth is found during atmospheric ice build-up on aircraft [4] and power lines [3] in humid or foggy conditions, or during freezing rain events [8]. It also plays a role in the growth of hailstones [9, 10] in clouds.

In the particular case of icicles, they form from water dripping off an overhang in a sub-freezing atmosphere. Growth begins when a drop of water freezes on the supporting structure. As water continues to flow, it collects in a pendent drop at the tip of the icicle, which partially freezes as it is cooled by the surrounding air, gradually increasing the icicle's length. Along the length of an icicle, some of the water will

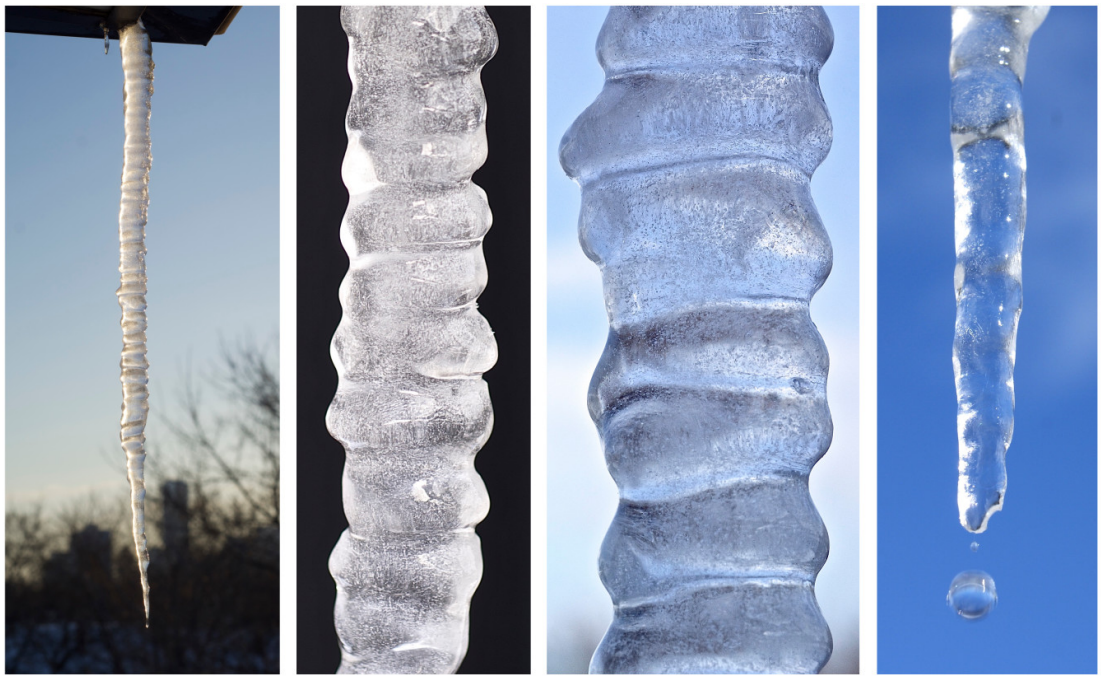

Figure 1.1: Various images of natural icicles. The first image shows a complete icicle from root to tip. The next two images show detailed views of typical ripple patterns. The final image shows a tip shedding a mm-scale droplet.

freeze to the surface, increasing the icicle's radius, and releasing latent heat to the atmosphere. The amount of cooling is greater in the pendant drop than along the icicle's length, so the icicle's length grows faster than its diameter [11], leading to an elongated shape.

Only icicles grown from impure water exhibit ripples about their circumference [12]. The concentration of impurities needed for ripples to form is as small as 20 ppm NaCl – less than tap-water, and 1700 times lower than seawater. While atmospheric precipitation is typically quite pure, many naturally occurring icicles on structures nevertheless exhibit clear effects of impurities, and water can take up impurities as it flows over structures [12]. Due to the importance of marine ice in shipping and coastal structures, the majority of research in icicles grown with impurities focuses on marine ice grown with seawater concentrations near 35 ppt NaCl [13, 14, 15, 16, 17], much higher than applicable to typical freshwater icicles.

The ripples seen on icicles are observed to have a universal wavelength of $\sim$9 mm [18, 19, 12, 20]. Remarkably, this wavelength is not affected by the atmospheric conditions, flow rate of source water, or amount of dissolved impurities in the source water. During the formation of icicles grown with concentrations below 320 ppm NaCl, the

ripples consistently migrate upwards. Above 320 ppm NaCl, the behaviour of ripples becomes more dynamic and unpredictable, migrating either upwards or downwards, with ripples splitting apart or merging with neighbours. Rippled icicles usually have a "foggy" appearance with many small inclusions seen in their interior.

The most significant effect of dissolved impurities in ice formation that may play a role in ripple formation is freezing point depression. Freezing point depression is a consequence of the entropy of mixing in a solution [21]: the presence of dissolved molecules in a mixture increases the entropy compared pure water, which lowers the equilibrium temperature between solid and liquid. For ideal solutions, this is a colligative phenomenon, meaning that the amount of freezing point depression only depends on the number of dissolved molecules, not on the chemical properties such as charge or mass.

As a result of freezing point depression, binary mixtures such as saline water are known to exhibit a microscopic morphological instability as they freeze, known as the Mullins-Sekerka instability [22]. The solid front is stabilized by the latent heat transport through the solid, while the rejection of solute from the solid causes an accumulation of impurities at the surface contributing to the instability. At low solute concentrations, the solidifying front undergoes stable planar growth. At higher concentrations of solute, the front velocity is faster than the transport of solute, and the *constitutional undercooling* instability appears, forming either a *cellular* solid or *dendritic* solid.

Wettlaufer applied the Mullins-Sekerka instability to low-concentration H_2O-NaCl mixture with applications to sea ice, which is known to have a cellular structure [23]. In the case of sea ice, water is cooled by the cold atmosphere with all latent heat released through the solid ice. At the concentrations considered for icicles in this thesis, the theory suggests that the freezing surface of ice would undergo stable planar growth. However, in the cross-sections of icicles that we show in Chapter 7, there is cellular ice with impurities trapped inside of small inclusions of liquid water, causing the foggy appearance. Dendritic growth is also possible without impurities due to a supercooling instability when the majority of latent heat is transported through the liquid water rather than the ice [24]. This type of ice is often called "spongy" or "mushy" ice.

Previous attempts to model icicles have attributed the ripples to a pattern-forming morphological instability [25, 26, 27, 28, 29, 30, 31, 32], but those models do not include impurities, and so cannot accurately explain or predict ripples. In other applications, similar models have proven fruitful, such as for steps on ice formed

on inclines [33], or stalactite morphology [34]. The dependence of icicle ripples on impurities has not yet been explained through theory.

In this thesis, we explore the icicle rippling instability through theory and experiment. We first extend Ueno's morphological model of icicle ripple growth [29] to incorporate impurities, and perform a linear instability analysis in Chapter 2. The linear stability analysis showed that this thin-film model of icicle growth is insensitive to the concentration of impurities, and cannot explain the formation of icicle ripples. A series of experiments were performed using the apparatus described in Chapter 3 to produce laboratory-grown icicles. The morphological effects of concentration and species of impurity were studied in Chapter 5 using a set of 128 icicles. By using fluorescent dye as the impurity, we were able to observe and measure the behaviour of liquid water on the surface of icicles in Chapter 6. The pattern and content of brine inclusions seen inside of icicles are examined in Chapter 7. The observations of surface liquid and inclusions provide novel insights, which will be important for future models of wet ice growth.

1.1 History of icicle research

There are very few studies of icicles before the 1980's. According to Maeno *et al.* [19], these reports focused on the crystalline structure and were not quantitative. Possibly the earliest paper observing icicle ripples is due to Torahiko Terada in an essay (Japanese) in 1933 [35]. Later, Hatakeyama and Nemoto measured a 9 mm ripple wavelength [36] in 1958. Outside of Japan, Laudise and Barns observed the grain orientation in harvested natural icicles [37], and in 1980, Knight observed "air bubbles" in "wrinkled" icicles that looked like growth rings [38]. Knight also suggested that ripples formed due to rapid freezing, comparing icicle growth to spongy hailstone growth. Geer grew some icicles in 1981, observing them and taking pictures throughout [39]. One observation Geer made is that water flowing down a previously inactive icicle will flow in a thin rivulet, and "Successive water drops will follow the same path as long as the track surface dose not completely freeze between flows." This observation does not appear to be repeated elsewhere, until we observed this more quantitatively in our wetting experiments [1].

The first quantitative study of icicles was performed by Maeno and Takahashi (1984) in which they grew icicles in a cold room, monitoring temperature, flow rate, and growth rates [40]. In addition to the lab-grown icicles, the harvested natural icicles, and measured an average ripple wavelength of 9.0 mm [18]. Maeno and Taka-

hashi also observed a pattern of air bubbles inside of rippled icicles that formed a pattern matching the ripples on the surface. They proposed the same mechanism of ripple formation as Knight.

A summary of the observations of Knight, Geer, and Maeno was published by Jearl Walker in his "Amateur Scientist Column" in Scientific American [41], which highlighted the curious properties of ice and the questions still open about their formation.

1.1.1 Theories

Based on their observations, Maeno and Takahashi enumerates three modes of icicle growth [40]. Those modes, illustrated in Figure 1.2 are:

Mode 1 a pendent drop collects at the tip, and freezes around its perimeter to increase length;

Mode 2 water *flowing* down the outside surface cools, and partially freezes, increasing the radius;

Mode 3 water is trapped in the core of the icicle, eventually freezing to solidify the core.

A curious feature of icicles is that a central column of water is exposed at the tip of growing icicles. This water column is due to the outer edge of the pendant drop freezing first, followed by the slower *mode 3* growth.

The first mathematical model of icicle growth was proposed by Makkonen [11] in order to model the elongated form of icicles. In this model, liquid water flows over the surface, cooled by the surrounding atmosphere. Because the water experiences greater heat loss at the tip than on its sides, the elongation rate is faster than the radial growth rate. The growth rates of icicles can be calculated by considering a balance between the water flux and heat flux. Makkonen's model of icicle growth agrees with the experiments performed by Maeno *et al.* [19]

Simultaneously to Makkonen, Johnson and Lozowski began developing computational models of icicle growth [42] and conducted their own cold room experiments. Chung and Lozowski extended the model to marine icicles, which form seawater spray [14]. Lozowski also created stochastic computational models based on this and Szilder's work [5, 43] in his research on structural icing [5, 17, 42].

More recently, attention has been given to more accurate models of heat flux to the air surrounding icicles. Short *et al.* considered how natural air convection would affect

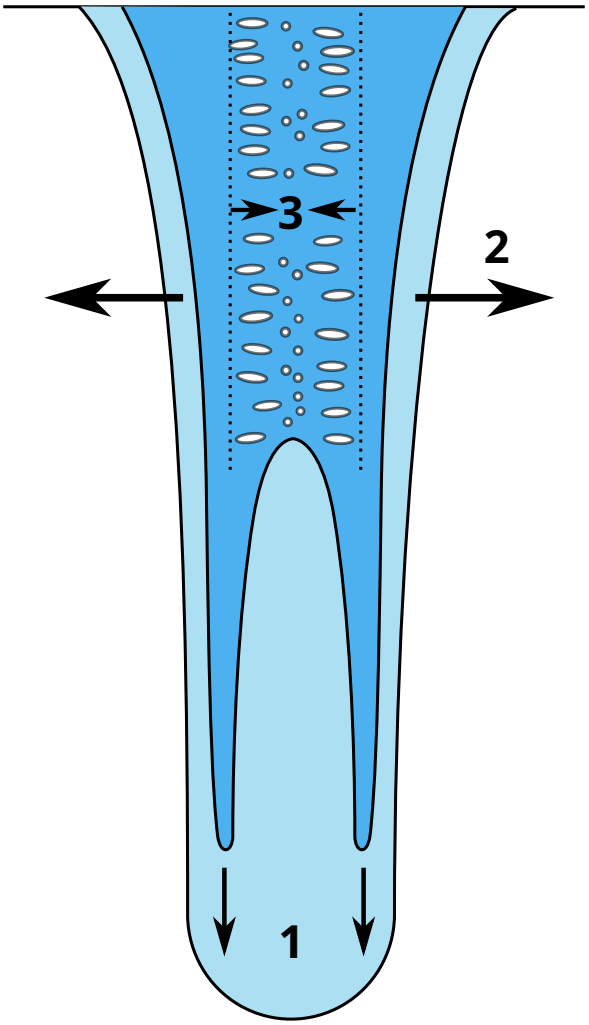

Figure 1.2: The three modes of icicle growth described by Maeno *et al.* [40]. First an icicle grows in length as the pendant drop freezes, then it grows in width as water flowing over the surface partially freezes. Finally, the liquid contained in the core freezes, trapping dissolved gases.

the latent heat flux from icicles, and found a self-similar shape [44]. This self-similar shape was confirmed experimentally by Chen *et al.* [45]. Neufeld created a boundary layer model of heat-transport around melting ice, confirmed by experiment [46]. He found that there was no need to model the thin film of liquid in order to predict the morphology of a melting cylinder of ice.

On the subject of ripples, mechanisms of ripple growth were proposed in early studies of icicles. Knight [38] proposed that ripples were related to crystal orientation and draining. Maeno [18, 19] theorized that ripples were caused by rapid freezing at the peaks, because of thinner water and greater heat flux to atmosphere. The "air bubbles" he observed inside icicles pointed to this spongy ice and rapid freezing. Through the experiments conducted in Chapter 7, it is our opinion that the rapid freezing mechanism does not explain ripple formation, because radial growth is actually quite slow, and we found that the "air bubbles" were actually pockets of impure water.

The first continuum theory of icicle ripples is due to Ogawa *et al.* [25]. Subsequently, in a series of papers, Ueno *et al.* [26, 27, 28, 30, 31, 29] elaborated upon a physically similar model using different approximations and different assumptions about thermal boundary conditions, some of which are unphysical in nature. Ueno *et al.* also explored several different heat transfer mechanisms in the surrounding air, going beyond simple diffusion. These models both produce a linear instability whose most unstable mode is a traveling ripple with a wavelength close to the observed universal wavelength. The Ogawa model predicts that the ripples should travel downward, while the Ueno model predicts upward motion. Experimentally, ripples are observed to travel upward at lower impurity concentrations, and downward for higher concentrations [12]. An analogous, but chemically more complex model has been proposed to explain ripples on stalactites [34]. Bertagni and Camporeale performed a weakly nonlinear stability analysis for pure water icicles, using a similar model of icicle growth developed in collaboration with the author, and found that there is no morphological instability [47]. Bertagni's results are discussed further in Chapter 2.5.

In the work of both Ogawa and Ueno, the water is assumed to be pure. However, the experiments performed by Chen and Morris established that ripples do not form without impurities in the water [12, 20], falsifying both the Ogawa and Ueno models.

Furthermore, nearly all work on icicle growth has assumed that an icicle is fully ensheathed in a thin film of water flowing over the surface [44, 25, 26, 27, 28, 30, 31, 29, 34]. The thermodynamics associated with the spreading coefficient shows that

a quasi-liquid layer is present on ice [48], which has been used to justify a uniform liquid flow over the surface. However the liquid flow is shown not to be uniform in our experimental observations in Chapter 6. Instead, it descends in rivulets, leaving the majority of the ice surface exposed.

1.2 Outline

We extended the thin-film ripple theory developed by Ueno *et al.* to include impurities and performed a linear stability analysis, as presented in Chapter 2. In order to ensure the physical accuracy of the model, the boundary conditions were all derived anew, referring to mushy layer theory [49] for the conditions at the ice-water interface, and using the models by Makkonen [11] and Neufeld [46] for the thermal flux at the water-air interface. The details of the physical model derivation are presented in Appendix A. The linear perturbation was calculated numerically using power-series solutions of the differential equations, following a similar method that Camporeale *et al.* used for stalactite growth [34].

We found that the physically correct thin-film model is unstable for all wavelengths, and has very little dependence on the concentration of the source water. This in born out in the thermal and concentration boundary conditions – the coefficients associated with concentration are insignificant compared to those of temperature. Our analysis indicated that such a model cannot accurately explain the mechanics of ripple formation on icicles.

To better understand the role of impurities in icicle formation we grew and measured approximately 130 icicles. The icicles were grown and monitored in an improved icicle machine that we built based on the machine used by Chen in his experiments [45, 12]. The icicle machine, described in Chapter 3, grows icicles on a slowly rotating support with controlled temperatures and feed-water flow rate. Images were taken of the icicles 16 times per revolution at fixed orientations, so that a full 3D view of the icicle can be reconstructed throughout its growth. The icicles could also be removed after growing for further analysis, including measuring cross-sections to examine their interior.

Along with the icicle machine, a Python library was developed to measure the icicle morphology from the roughly 700 pictures taken for each icicle. The edge-extraction algorithm, and methods to measure the radius, length and rippled topography are explained in Chapter 4.

In Chapter 5, we present a statistical study of the morphology of 128 icicles grown

in our icicle machine. We consider the radial and elongation rates as affected by concentration and species of impurity, as well as the ripple wavelength and amplitude. The species of dissolved solid was found to have no effect on the morphology of icicles. The morphology only depended on the molar concentration of molecules inside the liquid, which shows that icicle ripples are a colligative phenomenon.

To gain more insight into the behaviour of impurities, a dye was used as the instability-triggering impurity. This allowed direct observation of the liquid distribution on the surface of icicles, and inside the ice. Our experiments on the distribution of water on the surface of icicles are presented in Chapter 6. The water on the surface of icicles was observed to descend periodically in thin rivulets, not in a uniform layer around the circumference. The surface was never uniformly covered in liquid except for a short region near the tip, violating a fundamental assumption of the thin-film ripple model. The amount of water retained on the icicle surface increased as the concentration of impurities increased, and had a tendency to sit in pools on the upper surface of ripples. The pools of liquid remained longer, and spread out more broadly when the concentration of impurities was higher. The flow and distribution of liquid on the surface of icicles is critical for understanding icicle ripple formation.

The fluorescent dye also allowed for direct observation of the impurities trapped inside the ice. The impurities were seen to collect in pockets of liquid, previously assumed to be air bubbles. Our observations of the inclusions inside of icicles are presented in Chapter 7. The amount of inclusions also increase with concentration. With distilled water, there are only a few thin crescents of inclusions. As the concentration increases, more crescents appear, forming a chevron pattern in the cross-sections, matching the ripples on the surface. Above 300 ppm NaCl, the resulting icicles are fully saturated with liquid inclusions, forming entirely mushy ice with no pattern in the cross-section.

Finally, a discussion of the experimental results and their implications is presented in Chapter 8. We discuss how our observations of the distribution of surface liquid and its interaction with exposed cellular ice changes the understanding of wet ice formation at low concentrations of impurities. We propose a new model of cyclic wetting and freezing to explain the mechanism of ripple formation in wet ice growth with impurities.

Chapter 2

Thin-film Theory

This chapter includes work that was presented as a poster at the 14th International Conference on the Physics and Chemistry of Ice [50]. The non-dimensionalization presented in Section 2.2 was produced in collaboration with Matteo Bertagni and Carlo Camporeale.

As discussed in Section 1.1.1, a model for icicle ripple formation was developed by Ogawa *et al.* [25] and Ueno *et al.* [26, 27, 28, 30, 31, 29] Both of these models are based upon a thin-film flow of water on a vertical surface. There is a wealth of theory and analysis on the stability of such thin-films [51, 52], and similar models have been successfully applied to other morphological phenomena, such as cyclic ice steps [33] and stalactite formation [34]. While both the Ogawa and Ueno models find a morphological instability matching the wavelength of icicle ripples, neither model includes physical effects from impurities in the source water. Therefore, they cannot accurately explain the formation of ripples on icicles.

In this chapter, we extend the Ueno model to include impurities. In the generalized model, we included impurities by adding the physics of impurity transport; the advection and diffusion of concentration and its associated boundary conditions. All of the boundary conditions are derived from physical conservation laws. Notably, the generalized thin-film model couples the temperature and concentration at the growing ice water interface to include the effect of freezing point depression. Our linear instability analysis of the model demonstrates that even with the inclusion of impurities, a thin-film model cannot not explain ripples on the surface. This is due to the fact that the coupling between the temperature and concentration fields is weak.

The model we developed was also studied by Bertagni [47] using a weakly nonlinear stability analysis. When the limiting case of pure water was considered, he found that

the ice surface is stable for all wavelengths, matching the experiments by Chen and Morris [12]. Unfortunately, it is not possible to apply that analysis when impurities are present, because of the accumulation of impurities down the icicle's length.

Both the Ogawa and Ueno models treat the emergence of the ripples as the outworking of a linear instability away from a simplified basic parabolic shear flow state. The problem is treated as axisymmetric, so that the icicle is assumed to be covered by a uniform sheath of flowing liquid water in the basic flow state. The overall shape of the icicle is ignored and it is treated as planar. These models both produce a linear instability whose most unstable mode is a traveling ripple with a wavelength close to the observed universal wavelength. However, some of the boundary conditions used by Ueno *et al.* for the temperature are not physically accurate. In particular, the temperature of the ice water interface is left unconstrained [30], when it should be at the melting point due to local thermal equilibrium. The Ogawa model does constrain the temperature of the ice-water interface to be equal to the melting temperature of ice. This boundary condition, if generalized to include freezing point depression, would be the same as the one used in our generalized thin-film model developed below. The Ogawa and Ueno models also differ in the way they treat the surface tension at the free water surface, and in the details of the long wavelength approximation.

The generalized model presented here uses the same axisymmetric and planar ice assumptions as the Ogawa and Ueno models. The model produces an instability, but fails to predict a wavelength because the growth rate of the fastest growing linear mode diverges at short wavelengths. At present, there have no convergent, axisymmetric continuum linear stability theory based on a simplified basic flow state which also accounts for impurities.

The rest of this chapter presents the generalized thin-film model of icicle growth with impurities, and the linear stability analysis of the ice surface. We first explain the physically derived thin-film model in Section 2.1, with full details of the derivation left to Appendix A. The full model is complicated, with several conflicting length and time scales, so it is non-dimensionalized in Section 2.2 for subsequent analysis. The linear stability analysis is presented in Section 2.3 through a long series of calculations, following the procedures used by Ueno for icicles [26, 27, 28, 29, 30, 31, 32], and Camporeale *et al.* for stalactites [34].

The results of the linear stability analysis were first presented at the 14^{th} conference on the Physics and Chemistry of Ice [50]. These results are included in Section 2.4, and a discussion of the implications to future modelling of the icicle ripple problem follows in Section 2.5.

2.1 Physical thin-film model

The thin-film model of icicle growth presented here is an extension of the model used by Ueno, Farzaneh *et al.* [26, 27, 28, 29, 30, 31, 32] In this model, the icicle is fully-ensheathed in a thin film of water descending flowing down the icicle. Assuming axial symmetry, and a sufficiently large radius, the model can be reduced to a 2-D open-channel flow, driven by gravity.

Our model, which is illustrated in Figure 2.1, differs from Ueno's, both in the inclusion of impurities in the water, and a careful derivation of thermal boundary equations from local thermodynamic equilibrium, and cooling from diffusion, evaporation and radiation.

As is often the case, all of the most significant physics to the problem emerge in the boundary conditions. In particular, for the study of icicles with impurities, constitutional undercooling at the ice-water interface is necessary. The latent heat is released as the ice wall freezes is described by the Stéfan boundary condition. Rejection of impurities from the ice produces a similar boundary condition for the concentration. Because the ice is fully coated in a film of water, heat can only escape to the atmosphere, so the latent heat is released through the liquid film to the atmosphere. This fact also ensures that the temperature inside the ice is at the melting point. Unlike heat or dissolved gasses, the dissolved solid impurities cannot travel into the atmosphere, so they are trapped in the liquid film.

The equations of the thin-film model are presented below, with a fully detailed derivation in Appendix A. In the following presentation, we use the subscripts t, x, y to indicate partial derivatives. The governing equations for the flow, temperature and concentration of the liquid thin-film are:

$$\vec{\mathbf{u}}_t + (\vec{\mathbf{u}} \cdot \nabla)\vec{\mathbf{u}} = -\frac{1}{\rho_{\mathrm{w}}}\nabla p + \nu \nabla^2 \vec{\mathbf{u}} + \vec{\mathbf{g}}\,, \tag{2.1a}$$

$$\nabla \cdot \vec{\mathbf{u}} = 0\,, \tag{2.1b}$$

$$T_t + (\vec{\mathbf{u}} \cdot \nabla)T = \kappa_{\mathrm{w}} \nabla^2 T\,, \tag{2.1c}$$

$$C_t + (\vec{\mathbf{u}} \cdot \nabla)C = D \nabla^2 C\,, \tag{2.1d}$$

using the notation described in Table 2.1. These governing equations are quite standard: The flow is governed by gravity driven incompressible Navier-Stokes flow (2.1a, 2.1b), and temperature follows the advection-diffusion equation (2.1c). The concentration is treated as a passive tracer, so it also follows the advection-diffusion equation (2.1d).

All of the crucial details in icicle growth appear in the boundary equations. There

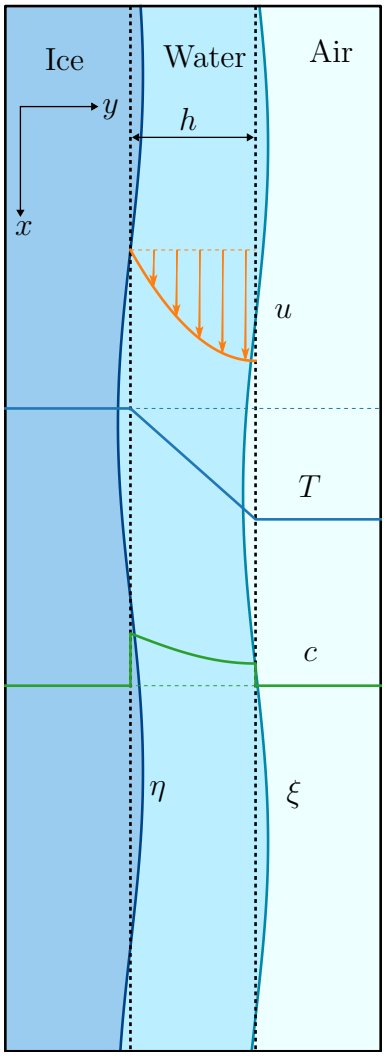

Figure 2.1: A cartoon of the thin-film flow model. In the equilibrium solution, the water descends in a parabolic sheer flow with depth h (nominally 0.1 mm), and has a linear temperature profile. The air is assumed well mixed in the far-field, with advective, evaporative and radiative cooling. A sinusoidal perturbation is applied to the ice surface, η, and air surface, ξ, then analyzed with linear stability theory.

Table 2.1: Symbols used in the dimensional thin-film model.

Symbol	Definition
x	Coordinate pointing down the icicle surface
y	Coordinate pointing radially outwards from the icicle surface
θ	Angle of the ice surface measured from vertical
$u(x,y,t)$	Velocity in the x direction
$v(x,y,t)$	Velocity in the y direction
$p(x,y,t)$	Pressure inside the film
$T(x,y,t)$	Temperature
$C(x,y,t)$	Concentration
$\eta(x,t)$	The ice-water boundary
$\xi(x,t)$	The water-air boundary
ν	Kinematic viscosity of water
$\hat{\mathbf{n}}$	Normal unit vector of the surface (either η or ξ depending on context)
$\hat{\mathbf{t}}$	Tangent unit vector of the surface
$\mathcal{K}$	Curvature of the surface
$\underline{\tau}$	The stress rate tensor for liquid
$\rho_{\mathrm{w}}, \rho_{\mathrm{i}}$	Density of water, ice
$\kappa_{\mathrm{w}}, \kappa_{\mathrm{i}}$	Thermal diffusivity of water, ice
Λ_{w}, Λ_{i}	Thermal conductivity of water, ice
c_p	Heat capacity of water at constant pressure
D	Mass diffusivity of impurities
J_{AD}, J_R, J_H	Thermal flux due to advection/diffusion of air, radiation, evaporation
T_{m}	Freezing point of water (0°C)
$T_L(C)$	The liquidus (freezing point at concentration C)
m	The slope of the liquidus
L	Specific latent heat of fusion
γ	Surface tension of water
γ_i	Surface energy between ice and water
$r_\rho = \rho_{\mathrm{i}}/\rho_{\mathrm{w}}$	Ratio of densities between ice and water
$r_\Lambda = \Lambda_{\mathrm{i}}/\Lambda_{\mathrm{w}}$	Ratio of thermal conductivities between ice and water
h	Average thickness of the liquid film
$\bar{V}$	Average velocity of ice-water surface
U	Surface velocity of the liquid film
k_0	nominal ripple wavenumber
σ	Growth rate of perturbation
k	Wavenumber of perturbation

are 11 boundary equations in total. First, the boundary conditions for flow are:

$$\text{no-slip:} \qquad \hat{\mathbf{t}} \cdot \vec{\mathbf{u}}|_{y=\eta} = 0\,, \tag{2.2a}$$

$$\text{undercooling:} \qquad \hat{\mathbf{n}} \cdot \vec{\mathbf{u}}|_{y=\eta} = (1 - r_\rho)\eta_t\,, \tag{2.2b}$$

$$\text{kinematic:} \qquad \xi_t + (u|_{y=\xi})\xi_x = v|_{y=\xi}\,, \tag{2.2c}$$

$$\text{lateral stress:} \qquad \hat{\mathbf{n}} \cdot \underline{\tau} \cdot \hat{\mathbf{t}}|_{y=\xi} = 0\,, \tag{2.2d}$$

$$\text{normal stress:} \qquad \hat{\mathbf{n}} \cdot \underline{\tau} \cdot \hat{\mathbf{n}}|_{y=\xi} + \gamma\mathcal{K}|_{y=\xi} = -p_{\text{atm}}\,. \tag{2.2e}$$

The usual "no-slip" condition (see [53] or [54]) must be split into normal and tangential components, because of absorption of liquid water onto the advancing wall of ice. The no-slip condition, equation (2.2a), states that the fluid velocity tangential to the ice-water boundary must be zero, while the "freezing" condition (2.2b) describes the effect of water absorption on the flow. The freezing condition is derived from a conservation of mass consistent with mushy-layer theory [49]. Because we are modelling moving boundaries, the surface stresses are left in their tensor forms in equations (2.2d, 2.2e), where $\underline{\tau}$ is the stress tensor.

The boundary equations for the concentration and temperature are:

$$\text{Stéfan:} \qquad (\rho_{\text{i}} L + 2\mathcal{K}\gamma_{\text{i}})\eta_t = (\Lambda_{\text{i}}\nabla T_{\text{i}} - \Lambda_{\text{w}}\nabla T_{\text{w}}) \cdot \hat{\mathbf{n}}\,, \tag{2.3a}$$

$$\text{undercooling:} \qquad T|_{y=\eta} = T_{\text{m}}\left(1 + 2\mathcal{K}\frac{\gamma_{\text{i}}}{\rho_{\text{i}} L}\right) - mC|_{y=\eta} \tag{2.3b}$$

$$\text{T continuity:} \qquad T_{\text{w}}|_{y=\xi} = T_{\text{a}}|_{y=\xi} \tag{2.3c}$$

$$\text{heat flux:} \qquad -\Lambda_{\text{w}}\hat{\mathbf{n}} \cdot \nabla T|_{y=\xi} = J_{AD} + J_R + J_H\,, \tag{2.3d}$$

$$\text{impurity rejection:} \qquad C|_{y=\eta}\,\eta_t = -D\,\hat{\mathbf{n}} \cdot \nabla C|_{y=\eta}\,, \tag{2.3e}$$

$$\text{impurity trapping:} \qquad \hat{\mathbf{n}} \cdot \nabla C|_{y=h+\xi} = 0\,. \tag{2.3f}$$

The Stéfan condition (2.3a) limits the rate of freezing, balancing the release of latent heat, $\rho_i L\eta_t$, with the heat transport at the surface. The "undercooling", "impurity-rejection", and "impurity-trapping" conditions capture the effect of dissolved impurities. Constitutional undercooling and the Gibbs-Thomson effect [55] are included in equation (2.3b). Equations (2.3e) and (2.3f) are derived from conservation of mass: we assume all impurities are contained in the liquid water, so there is zero flux between air and water, but the rejection of impurities from the ice appears as an influx proportional to the rate of ice growth. This has a similar effect to the Stéfan condition (2.3a), in which latent heat is released from the ice surface as water freezes. The

derivation of the impurity boundary equations is explained in Appendix A.

The boundary condition for temperature at the air is the most complicated to model, because it incorporates heat flux between the water film and the surrounding turbulent air. We chose to use a one-dimensional heat flux model based on the work by Neufeld [46], which accurately models the heat flux due to advection, evaporation and radiation. The crux of that heat-transport model is heat diffusion across a thin boundary layer of air surrounded by turbulently mixed air. Neufeld found that evaporative cooling was significant and proportional to diffusive heat transport. However, the relative humidity in the icicle-machine is above 90%, so evaporation is less significant for our lab-grown icicles.

With so many variables, equations, and parameters, we need to perform a careful non-dimensionalization to simplify the problem. The resulting model is summarized in the next section, with details in Appendix B.

2.2 Non-dimensionalization

A careful non-dimensionalization was carried out to properly assess which mechanisms and parameters are the most significant in ripple formation. For the rest of the chapter, quantities are understood to be dimensionless unless noted otherwise.

During the non-dimensionalization, we adopt a reference frame which moves with the ice surface at velocity $\bar{V}$. The variable scales are defined as follows, with tildes indicating the dimensional (physical) quantities.

$$\begin{aligned} \tilde{x} &= x\frac{h}{\mu} & \tilde{y} &= hy + \bar{V}\tilde{t} & \tilde{t} &= \frac{h}{\bar{V}}t \\ \tilde{u} &= Uu & \tilde{v} &= \mu U v + \bar{V} & \tilde{p} &= Pp + p_{\text{atm}} \\ \tilde{T} &= \Delta T T + T_{\text{m}} & C &= \Delta C c\,, \end{aligned} \tag{2.4}$$

where h is the average depth of the water film, $\bar{V}$ is the average velocity of the ice surface (i.e. average radial growth rate of the icicle), U is the fluid velocity at the air, and p_{atm} is atmospheric pressure. The temperature scale, ΔT is the temperature difference across the liquid film (typically a few milliKelvin), and the concentration scale is related to temperature through the liquidus slope $\Delta C = \Delta T/m$. The aspect ratio, μ, is defined in (2.6).

The other variables that need to be non-dimensionalized are the moving boundaries, $y = \eta(x,t)$, and $y = \xi(x,t)$. The ice and water surfaces are defined by the

functions

$$\tilde{\eta}(\tilde{x},\tilde{t}) = \bar{V}\tilde{t} + \eta_0\eta(x,t) \qquad \tilde{\xi}(\tilde{x},\tilde{t}) = h + \bar{V}\tilde{t} + \eta_0\xi(x,t)\,, \tag{2.5}$$

where η_0 is the non-dimensional amplitude of η, and we assume that ξ has a similar size of variation.

After these scales are introduced, two aspect ratios emerge,

$$\mu = k_0 h\,, \qquad \delta = k_0\eta_0\,, \tag{2.6}$$

where k_0 is the typical wavenumber, corresponding to a wavelength of approximately 10 mm, matching the ripples. The ratio $\mu \approx 6\times10^{-2}$ compares the film thickness to the variation in x (the ripple wavelength). The ratio $\delta \ll 1$ is the small-ripple approximation, and will be used as the perturbation parameter.

There are also two separate time scales in the model, τ is the hydrodynamic timescale for the flow, and τ_F characterizes the rate of freezing. The ratio between these timescales is

$$\bar{\mathrm{v}} = \mu\frac{\tau}{\tau_F} = \frac{\bar{V}}{\mu U}\,, \qquad \text{where} \tag{2.7}$$

$$\tau = \frac{h}{\mu U} = \frac{1}{kU}\,, \qquad \text{and} \qquad \tau_F = \frac{h}{\bar{V}} = (r_\rho \mu \mathrm{Pe}\,\mathcal{S}\,)^{-1}\,. \tag{2.8}$$

The dimensionless numbers Pe and $\mathcal{S}$ are summarized in Table 2.2 along with the other numbers that emerge from the non-dimensionalization. The typical scales for icicle formation are described in Table 2.3. The non-dimensionalized thin-film model using the above scales and dimensionless parameters is presented below.

2.2.1 The non-dimensionalized thin-film model

When the scaling equations (2.4) are substituted into the Navier-Stokes equations (2.1a) and (2.1b), the governing equations for flow become,

$$\bar{\mathrm{v}}u_t + \mu(uu_x + vu_y) = -\mu p_x + \frac{1}{\mathrm{Re}}(\mu^2 u_{xx} + u_{yy} + 2)\,, \tag{2.9a}$$

$$\bar{\mathrm{v}}\mu v_t + \mu^2(uv_x + vv_y) = -p_y + \frac{\mu}{\mathrm{Re}}\left(\mu^2 v_{xx} + v_{yy} + 2\tan(\theta)\right)\,, \tag{2.9b}$$

$$u_x + u_y = 0\,. \tag{2.9c}$$

Table 2.2: The dimensionless numbers for the thin film model, with their definition and nominal values.

Name	Symbol	Definition	Value
Aspect ratio	μ	kh	6.28×10^{-2}
Time ratio	$\bar{\mathrm{v}}$	$\frac{\bar{V}}{U}$	4.8×10^{-5}
Reynolds	Re	$\frac{Uh}{\nu}$	0.36
Weber	We	$\frac{\rho_{\mathrm{w}} U^2 h}{\gamma}$	9.1×10^{-5}
Stéfan	$\mathcal{S}$	$\frac{L}{c_{\mathrm{p}} \Delta T}$	1000
Peclet	Pe	$\frac{Uh}{\kappa}$	4.8
Lewis	Le	$\frac{\kappa}{D_s}$	12

Table 2.3: Relevant scales to icicle growth.

Quantity	Symbol	Definition	Typical value
wavenumber	k		6.28 cm^{-1}
film thickness	h		0.1 mm
surface velocity	U	$gh^2 \cos(\theta)/2\nu$	2.7×10^{-2} m/s
mean growth rate	$\bar{V}$		1.3×10^{-6} m/s
pressure	P	$\rho_{\mathrm{w}} U^2$	
temperature gradient	ΔT	$\tilde{T}(\tilde{y}=h) - \tilde{T}(\tilde{y}=0)$	75 mK
melting point	T_{m}	$T_L(0)$	0°C
feedwater concentration	C_0		0 – 30 mMol/kg
concentration	ΔC	$\Delta T/m$	20 mMol/kg

With the understanding that $\bar{\mathrm{v}} \ll \mu \ll 1$, we see that the majority of terms are small and the equations simplify dramatically. This assumption will be used to find the equilibrium base state for the linear stability analysis in Section 2.3.1.

Doing the same substitution for the fluid boundary conditions 2.2, we find,

$$(y=\eta) \qquad u + \delta\eta_x\left(\mu v + \bar{\mathrm{v}}\right) = 0\,, \tag{2.10a}$$

$$(y=\eta) \qquad \mu^2 v + r_\rho \mu \bar{\mathrm{v}} - \mu\delta u\eta_x = \bar{\mathrm{v}}\delta(1-r_\rho)\eta_t\,, \tag{2.10b}$$

$$(y=\xi) \qquad \mu v = \delta\left(\frac{\bar{\mathrm{v}}}{\mu}\xi_t + u\xi_x\right)\,, \tag{2.10c}$$

$$(y=\xi) \qquad (u_y + \mu^2 v_x) + 2\mu\delta\xi_x(v_y - u_x) = 0\,, \tag{2.10d}$$

$$(y=\xi) \quad -p + \frac{2}{\mathrm{Re}}\left[\mu v_y - \delta\xi_x(u_y + \mu^2 v_x)\right] - \mu\frac{1}{\mathrm{We}}\delta\xi_{xx} = 0\,. \tag{2.10e}$$

By setting $\delta = 0$, the problem for a flat ice surface emerges. It is noteworthy that the freezing condition (2.10b) has a non-zero velocity, v, due to the adsorption of water into the ice.

Of course, the growth of an icicle is dictated by the temperature and concentration of the thin film. They follow the relatively rapid flow as passive tracers, with governing equations,

$$\bar{\mathrm{v}}T_t + \mu(uT_x + vT_y) = \frac{1}{\mathrm{Pe}}(\mu^2 T_{xx} + T_{yy})\,, \tag{2.11a}$$

$$\bar{\mathrm{v}}C_t + \mu(uC_x + vC_y) = \frac{1}{\mathrm{Le}\,\mathrm{Pe}}(\mu^2 C_{xx} + C_{yy})\,. \tag{2.11b}$$

The entirety of the icicle growth is modelled through the boundary conditions of the temperature and concentration fields,

$$(y=\eta) \qquad T = c\,, \tag{2.12a}$$

$$(y=\eta) \qquad -r_\rho \mathrm{Pe}\,\mathcal{S}\,\bar{\mathrm{v}}(\mu + \delta\eta_t) = \mu T_y - \mu^2\delta\eta_x T_x\,, \tag{2.12b}$$

$$(y=\xi) \qquad T_y + \mu\delta\eta_x T_x = \hat{j}(x,t)\,, \tag{2.12c}$$

$$(y=\eta) \qquad r_\rho \mathrm{Le}\,\mathrm{Pe}\,\bar{\mathrm{v}}\,(\mu + \delta\eta_t)\,c = -\mu c_y + \mu^2\delta c_x\eta_x\,, \tag{2.12d}$$

$$(y=\xi) \qquad (\mu + \delta\eta_t)\,c = -\mu\frac{\mathcal{S}}{\mathrm{Le}}\left(c_y - \mu\delta c_x\eta_x\right)\,. \tag{2.12e}$$

In the non-dimensionalization, the Gibbs-Thomson effect was determined to be neglible, so it is omitted in equations (2.12a) and (2.12b). In equation (2.12c), $J(x,t)$ is the dimensionless heat flux, $(J_A D + J_R + J_H)h/\Lambda_{\mathrm{w}}\Delta T$. While the full form is quite complicated, it will be linearised as part of the stability analysis, becoming a Robin

boundary condition.

The above model is used in the following Linear stability analysis. The dimensionless numbers are used to simplify the analysis with reasonable assumptions. The base state is found first by setting $\mu = \bar{\mathrm{v}} = \delta = 0$. Then the perturbation is carried out with $\mu = 1$, $\bar{\mathrm{v}} \sim 1$ and $\delta \ll 1$ as the perturbation parameter.

2.3 Linear stability analysis

In the rest of this chapter, we present the linear stability analysis performed on the thin-film model. This analysis follows the procedure by used by Ueno *et al.* [26, 27, 28, 29, 30, 31, 32], for ripples on ice, and Camporeale *et al.* [34] for stalactites.

The analysis starts by finding an equilibrium solution (the *base state*) to the boundary value problem in Section 2.3.1, by assuming terms of order $\mathcal{O}(\mu)$, $\mathcal{O}(\bar{\mathrm{v}})$, and $\mathcal{O}(\delta)$ negligible. The Navier stokes equations are converted into a single PDE using a stream function in Section 2.3.2, in preparation for the linear perturbation. A linear perturbation is then applied, using a Fourier mode perturbation,

$$\begin{aligned} q(x,y,t) &= q^{(0)}(x,y) + q^{(1)}(x,y,t) \\ &= q^{(0)}(x,y) + \hat{q}(y)\exp(\sigma t + ikx) \end{aligned}, \tag{2.13}$$

for all quantities $q \in \{\psi, c, T, p, \eta, \xi, j\}$, where $q^{(0)}$ is the equilibrium solution, and $q^{(1)}$ is the linear perturbation which is assumed sinusoidal with amplitude $\hat{q}$. This perturbation produces an Orr-Sommerfeld problem for the flow in Section 2.3.3, and parabolic cylinder equations for temperature and concentration in Section 2.3.4. The thin-film flow is assumed quasi-steady, and instabilities in the flow are ignored, which is typical of how the linear stability has been analysed previously [26, 34]. Because the Orr-Sommerfeld problem is independent of temperature and concentration, it is solved first using a power-series method, then the solution is used in the boundary value problems for the temperature and concentration perturbations, which are shown in matrix form in Section 2.3.5.

The effects of concentration on stability were examined, and we explain why the presence of impurities have negligible effect on morphology in the thin-film model in Section 2.4. Finally, we address how this model may be further extended, using mushy layer theory or a weakly linear analysis. However, these possible avenues would likely be unfruitful, because the observations of the water flow in Chapter 6 show that the fundamental assumption of a thin film flow does not match reality.

2.3.1 Base solution

In order to solve the base state, a simplifying assumption is made. That is, the problem is assumed to be translationally invariant in x. This assumption ignores any loss of film thickness due to freezing, as well as the accumulation of impurities down the length of an icicle. We also restrict our analysis to a vertical ice surface.

The base state is complicated by the accretion of water as the ice grows, and the accumulation of impurities down the length of the icicle. For the following analysis, we ignore the loss of water in the film, and the effects that impurity accumulation would have on the temperature. The effect of impurity accumulation was considered for the base state and subsequent analysis. It was found that there will be a small concentration gradient at the ice surface, with an exponential increase in concentration that doubles every 18.5 cm. This increase in concentration is at a much larger scale than ripples, so it shouldn't have a significant effect, but the gradient in y may affect the perturbation. For ease of readability, the exponential increase in concentration was omitted for the calculations presented in Sections 2.3.4, 2.3.5, and 2.4, but calculations that included the x-dependent concentration and temperature showed that it had negligible effect.

Base state for flow

The non-dimensionalization points to a parabolic-shear flow for the base state. Simplifying the model by setting $\bar{\mathrm{v}} = \mu = \delta = 0$, The equilibrium solution is found to be,

$$u^{(0)}(x, y, t) = y(2 - y) \tag{2.14a}$$

$$v^{(0)}(x, y, t) = 0 \tag{2.14b}$$

$$p^{(0)}(x, y, t) = 0\,, \tag{2.14c}$$

which is the same parabolic shear flow used by Ogawa *et al.* [25] and Ueno *et al.* [30, 31, 29]. The velocity $v^{(0)} = 0$ is a result of ignoring the loss of water due to freezing. This is a necessary simplification for the stability analysis. Including the loss of water would make $v^{(0)} = -\bar{\mathrm{v}}$, and also necessitate changes to the water surface ξ.

Temperature base state

After applying the same simplification to the temperature boundary value problem, it reduces to,

$$T^{(0)}_{yy} = 0 \tag{2.15a}$$

$$T^{(0)}(y=0) = c(y=0) \tag{2.15b}$$

$$T^{(0)}_{y}(y=1) = 1\,. \tag{2.15c}$$

This problem is easily solved, producing the linear base state,

$$T^{(0)} = -y - c_0\,. \tag{2.16}$$

where $c_0 = C_0/\Delta C$ is the dimensionless source water concentration. However, if the concentration is allowed to increase with x, then $c(x, y=0)$ is not constant. Using the x-dependent base state for concentration in equation (2.31) below, the base state for temperature becomes,

$$T^{(0)}(x,y) = -y - c_0 e^{\frac{\lambda}{\mathrm{Le\,Pe}}x}\,. \tag{2.17}$$

While the change in temperature would also affect the heat flux into the air, the actual changes in heat flux due to temperature variations at this scale is quite low (about 0.4%). Furthermore, we found that the effect of advection on temperature is negligible; using the same methods for the x-dependent concentration solution, the most persistent mode decays on a length-scale of 0.01 cm. Using the x-dependent form for temperature significantly complicates the linear perturbation with negligible effect on the stability, so we proceed using equation (2.16).

Concentration base state

When applied to the concentration boundary value problem, the simplification $\bar{\mathrm{v}} = \mu = \delta = 0$ produces a problem. When these small parameters are set to zero, the

boundary value problem for concentration is

$$c^{(0)}_{yy} = 0 \tag{2.18}$$

$$c^{(0)}_{y}(y=0) = -\frac{\mathrm{Le}}{\mathcal{S}}c \tag{2.19}$$

$$c^{(0)}_{y}(y=1) = 0\,, \tag{2.20}$$

which includes a contradiction. Because the general solution to the PDE is $c(x,y) = A(x)y + B(x)$, it is impossible to satisfy both boundary conditions. If the first condition is satisfied, then impurities would have to leave to the air, while satisfying the second condition would require that no impurities are rejected from the ice during freezing. Choosing the latter condition,

$$c^{(0)}(x,y) = c_0\,. \tag{2.21}$$

Using that base case for concentration prevents modelling any accumulation of impurities down the icicle. In particular, there is no variation in concentration across the liquid film. Because the concentration gradient at the ice surface may affect the stability, we perform a more careful solution of the base state below.

X-dependent concentration

Rather than neglecting all terms of order μ in equation (2.11b), we consider a dominant balance of terms. Doing so produces a non-degenerate boundary value problem for the base state,

$$y(2-y)c^{(0)}_{x} = (\mathrm{Le}\,\mathrm{Pe}\,)^{-1}c^{(0)}_{yy} \tag{2.22a}$$

$$c^{(0)}_{y}(y=0) = -\frac{\mathrm{Le}}{\mathcal{S}}c(y=0) \tag{2.22b}$$

$$c^{(0)}_{y}(y=1) = 0 \tag{2.22c}$$

$$c^{(0)}(x=0) = c_0\,, \tag{2.22d}$$

which can be solved through separation of variables, $c^{(0)}(x,y) = X(x)\mathcal{C}(y)$. The solution for X is simple,

$$X(x) = c_0 e^{\frac{\lambda}{\mathrm{Pe}\,\mathrm{Le}}x}\,, \tag{2.23}$$

but $\mathcal{C}$ is governed by a parabolic cylinder equation,

$$\mathcal{C}'' - \lambda y(2-y)\mathcal{C} = 0\,, \tag{2.24}$$

with boundary conditions

$$\mathcal{C}'(0) + \frac{\mathrm{Le}}{\mathcal{S}}\mathcal{C}(0) = 0 \tag{2.25}$$

$$\mathcal{C}'(1) = 0\,. \tag{2.26}$$

From Sturm-Liouville theory, we know there are values λ_n such that $\lambda_1 > \lambda_2 > ... \to -\infty$. Because concentration should increase in the x direction, we expect $\lambda_1 > 0$.

The parabolic cylinder equation will also appear in Section 2.3.4 for the perturbations of heat and concentration. Solving the parabolic cylinder equation is simpler with a change of variables $z = 1 - y$ and $Z(z) = \mathcal{C}(y)$, to transform it into the standard form,

$$Z'' + \mu(z^2 - 1)Z = 0\,, \tag{2.27}$$

with boundary conditions

$$Z'(1) - \bar{\mathrm{v}}\mathrm{Le}\,\mathrm{Pe}\,Z(1) = 0 \tag{2.28}$$

$$Z'(0) = 0\,, \tag{2.29}$$

which matches 19.1.3 in Abromowitz and Stegun [56]. There are even and odd solutions to equation (2.27), but the odd solution is eliminated by the second boundary condition, equation (2.29). The final solution is of the form,

$$Z(z) = e^{-\frac{i}{2}\sqrt{\mu}z^2}\,{}_1F_1\left(-\frac{i}{4}\sqrt{\mu} + \frac{1}{4};\ \frac{1}{2};\ i\sqrt{\mu}z^2\right) \tag{2.30}$$

where ${}_1F_1$ is a confluent hypergeometric function. The confluent hypergeometric functions are special functions defined by their power series representations, so we calculate it numerically from the power series using 100 terms. The graph of this concentration base state is shown in Figure 2.1. While the form of Z is technically known, λ must be calculated numerically from the boundary value problem. Using parameters from the experiments, we calculate $\lambda_1 \approx 0.0927$, which corresponds to a length scale of 27.4 cm, meaning that the concentration doubles every 18.5 cm. More

generally, using the relation $\bar{\mathrm{v}} = (\mathrm{Pe}\,\mathcal{S}\,)^{-1}$, $\lambda \propto \mathcal{S}\,/\mathrm{Le}\,$, so that $\lambda \approx (0.00556)\mathcal{S}\,/\mathrm{Le}\,$. The next eigenvalue, $\lambda_2 \approx -18.13$, shows that all other modes decay very quickly. The corresponding length scale is 0.14 cm, so it is reasonable to approximate $c^{(0)}$ by the first mode.

Finally, the x-dependent base state for concentration is,

$$c^{(0)}(x,y) = c_0 e^{\frac{\lambda}{\mathrm{Le}\,\mathrm{Pe}}x}\mathcal{C}(y)\,. \tag{2.31}$$

It is possible to perform a linear perturbation using that form, but the increase in concentration with x is of order $\mathcal{O}(\lambda/\mathrm{Le}\,\mathrm{Pe}\,)$, much smaller than other effects, and does not affect the stability. For the rest of the analysis, we use the limit $\lambda/\mathrm{Le}\,\mathrm{Pe} \to 0$, and base state for concentration,

$$c^{(0)}(x,y) = c_0\mathcal{C}(y)\,. \tag{2.32}$$

Now that the equilibrium solution is established, we can begin the perturbation. The first step is to use a stream function for the fluid dynamics, so that the perturbation of the flow is described by an Orr-Sommerfeld problem.

2.3.2 Stream function and vorticity

Following the methods of Ueno and Camporeale [34], the linear perturbation of a thin-film flow is best done using the stream function. In the rest of the linear stability analysis, we set the aspect ratio $\mu = 1$, because it does not affect the rest of the theory. Keeping $\bar{\mathrm{v}} \ll 1$ justifies the quasi-steady approximation used in the Orr-Sommerfeld problem.

We introduce the stream function ψ and vorticity ω as follows

$$u = \frac{\partial\psi}{\partial y}\,, \qquad v = -\frac{\partial\psi}{\partial x}\,, \tag{2.33}$$

$$\omega = \nabla\times\vec{\mathbf{u}} = -\nabla^2\psi \tag{2.34}$$

with $\nabla = (\partial_x, \partial_y)$. Following Camporeale *et al.* [34], it is convenient to define

$$\hat{\nabla} = (-\partial_y, \partial_x) \quad \text{so that} \quad \vec{\mathbf{u}} = -\hat{\nabla}\psi\,. \tag{2.35}$$

Taking the curl of the Navier-Stokes equations (2.9), eliminates the pressure and

gravity term to give the vorticity equation

$$\bar{\nu}\omega_t + (\vec{\mathbf{u}} \cdot \nabla)\omega = \frac{1}{\mathrm{Re}}\nabla^2\omega\,. \tag{2.36}$$

The pressure remains in the boundary conditions. $\nabla \cdot \vec{\mathbf{u}} = 0$ is solved identically in the stream function formulation of Equation (2.9), which is

$$\bar{\nu}\mathrm{Re}\,\nabla^2\psi_t + \mathrm{Re}\;\hat{\nabla}\psi \cdot \nabla^3\psi + \nabla^4\psi = 0\,. \tag{2.37}$$

Similarly, the two advection diffusion equations, Equations (2.11a) and (2.11b) become

$$\frac{1}{\mathcal{S}}T_t + \mathrm{Pe}\;\hat{\nabla}\psi \cdot \nabla T + \nabla^2 T = 0\,, \tag{2.38}$$

$$\frac{\mathrm{Le}}{\mathcal{S}}c_t + \mathrm{Le}\,\mathrm{Pe}\;\hat{\nabla}\psi \cdot \nabla c + \nabla^2 c = 0\,. \tag{2.39}$$

Equations (2.37 - 2.39) are the concise forms of the full equations of motion which we must solve perturbatively.

Equations for perturbed quantities

We assume that the amplitude of the topographic perturbation is growing as

$$\eta = \hat{\eta}\, e^{\sigma t}\, e^{ikx}, \tag{2.40}$$

with the growth rate σ allowed to be complex to allow for traveling structures. We will only keep the time dependence in the hatted quantities when it appears in the boundary conditions at the growing surface. All other fields respond instantaneously to the slowly evolving topography.

We can now insert the perturbed fields into the basic equations and linearise them. We use the quasi-steady approximation in these equations, because $\bar{v} \ll 1$ the most significant temporal term is $\mathrm{Le}\,/\mathcal{S} \approx 0.06$. The base state parts cancel out, leaving equations for just the perturbed quantities.

To lowest order, Equation (2.37) is

$$\mathrm{Re}\,[\hat{\nabla}\psi^{(0)} \cdot \nabla^3\psi^{(1)} + \hat{\nabla}\psi^{(1)} \cdot \nabla^3\psi^{(0)}] + \nabla^4\psi^{(1)} = 0 \tag{2.41}$$

while Equations (2.38 and 2.39) are

$$\mathrm{Pe}\,[\hat{\nabla}\psi^{(0)}\cdot\nabla T^{(1)}+\hat{\nabla}\psi^{(1)}\cdot\nabla T^{(0)}]+\nabla^2 T^{(1)}=0 \tag{2.42}$$

$$\mathrm{Le}\,\mathrm{Pe}\,[\hat{\nabla}\psi^{(0)}\cdot\nabla c^{(1)}+\hat{\nabla}\psi^{(1)}\cdot\nabla c^{(0)}]+\nabla^2 c^{(1)}=0 \tag{2.43}$$

As mentioned above, the first task is to solve the fluid mechanical problem, which is to say to find an equation for the stream function perturbation $\psi^{(1)}=\hat{\psi}(y)e^{ikx}$.

2.3.3 Orr-Sommerfeld problem for flow

Inserting the expansion equation (2.13) for ψ into equation (2.41) and doing a lot of tedious but straightforward algebra gives a 4th order ODE for the amplitude $\hat{\psi}(y)$ of the stream function perturbation,

$$\left[\left(\frac{\mathrm{d}^2}{\mathrm{d}y^2}-k^2\right)^2-ik\mathrm{Re}\,u^{(1)}\left(\frac{d^2}{dy^2}-k^2\right)-\;2ik\mathrm{Re}\right]\hat{\psi}=0\,. \tag{2.44}$$

This is a version of the Orr-Sommerfeld (OS) Equation from thin-film stability theory [51, 52], which was used in the analysis by Ueno *et al.* for icicles [26, 27, 28, 31, 30, 29] and Camporeale *et al.* for stalactites [34, 57]. It represents the perturbation to the fluid flow field caused by the topographic perturbation η, which will appear in the boundary conditions. We still have to deduce the boundary conditions on $\hat{\psi}$ from the boundary conditions on the Navier-Stokes equations to solve this equation. Then its solution can be used to force the advection diffusion equations (2.42) and (2.43).

Some previous treatments approximate the solution to the OS equation in the small-wavenumber limit, $k\to 0$, by dropping all terms of order $\mathcal{O}(k^2)$. Solving the OS equation this way gives

$$\hat{\psi}_{k\to 0}=\left\{\left[\frac{i\alpha}{6-i\alpha}\right]y^3+\left[\frac{3(2-i\alpha)}{6-i\alpha}\right]y^2-2y\right\}\hat{\eta}\,. \tag{2.45}$$

where $\alpha=\frac{k^3\mathrm{Re}}{\mathrm{We}}$. Instead of using the $k\to 0$ limit, we opt to use a power-series solution following Camporeale *et al.* [34]. This should provide higher accuracy for a wider range of wavenumbers.

The Orr-Sommerfeld equation (2.44) is a fourth order linear ODE with analytic coefficients in the domain of interest, $y\in[0,1]$, so by Fuchs theorem,

$$\hat{\psi}=A_0\hat{\psi}_0+A_1\hat{\psi}_1+A_2\hat{\psi}_2+A_3\hat{\psi}_3\,, \tag{2.46}$$

where each $\hat{\psi}_j$, for $j \in \{1,2,3,4\}$, is an analytic function. We can find a recursion relation for $\hat{\psi}_j$ by substituting a powerseries into equation (2.44).

Before doing so, we adopt a change of coordinates to make calculations simpler. Using the coordinate $z = 1 - y$ will be particularly useful for the temperature and concentration equations in following sections. In these coordinates, $u^{(0)} = 1 - z^2$. Using these coordinates, and substituting the power series $\hat{\psi}_j(z) = \sum_{n\geq 0} a_{j,n} z^n$, we find the recurrence relation,

$$\begin{aligned} a_{j,n+4} = \frac{n!}{(n+4)!}\Big[&(ik\mathrm{Re} + 2k^2)\frac{(n+2)!}{n!}a_{j,n+2} \\ &+ \left(k^4 + ik\mathrm{Re}\left(k^2 + (n+1)(n-2)\right)\right)a_{j,n} \\ &+ ik^3\mathrm{Re}\, a_{j,n-2}\Big]. \end{aligned} \tag{2.47}$$

for $n > 4$, where $a_{j,-2} = a_{j,-1} = 0$ for the first few coefficients. The first 4 terms in each function are somewhat arbitrary. Because the $\hat{\psi}_j$ are independent, we choose $a_{j,n} = 1$ if $j = n$ and $a_{j,n} = 0$ otherwise for $n < 4$.

For a sense of the general solution, the first few terms are

$$\begin{aligned} \hat{\psi}_0(z) &= 1 + \frac{k}{24}\left[i\mathrm{Re}\,(2-k^2) - k^3\right]z^4 + \mathcal{O}(z^6) \\ \hat{\psi}_1(z) &= z + \frac{k}{120}\left[i\mathrm{Re}\,(2-k^2) - k^3\right]z^5 + \mathcal{O}(z^7) \\ \hat{\psi}_2(z) &= z^2 + \frac{k}{12}(i\mathrm{Re} + 2k)z^4 + \mathcal{O}(z^6) \\ \hat{\psi}_3(z) &= z^3 + \frac{k}{20}(i\mathrm{Re} + 2k)z^5 + \mathcal{O}(z^7)\,. \end{aligned}$$

The coefficients A_j in equation (2.46) are found using the boundary conditions.

Boundary conditions for the stream function

The boundary equations are linearized by substituting a Taylor expansion in y for the stream function about $y = 0$ and $y = 1$. The Taylor expansion at the ice surface is

$$\hat{\psi}(\eta) = \hat{\psi}(0) + \hat{\psi}'(0)\hat{\eta} + \mathcal{O}(\hat{\eta}^2)\,, \tag{2.48}$$

where prime notation is used for the first derivative, $\hat{\psi}'(y) \doteq \frac{\mathrm{d}\hat{\psi}}{\mathrm{d}y}(y)$. The expansion at the air is similar,

$$\hat{\psi}(\xi) = \hat{\psi}(1) + \hat{\psi}'(1)\hat{\xi} + \mathcal{O}(\hat{\xi}^2)\,. \tag{2.49}$$

The power series solutions to the differential equations for temperature and concentration are expressed more naturally with a change of coordinates $z = 1 - y$, because $u^{(0)}(z) = 1 - z^2$. After linearization, the boundary conditions for $\hat{\psi}(z)$ are,

$$\hat{\psi}(1) = 0 \tag{2.50a}$$
$$\hat{\psi}'(1) = (2 - ik\bar{v})\hat{\eta} \tag{2.50b}$$
$$\hat{\psi}(0) = -\hat{\xi} \tag{2.50c}$$
$$\hat{\psi}''(0) = (2 + k^2)\hat{\xi} \tag{2.50d}$$
$$\hat{\psi}'''(0) = (3k^2 + ik\mathrm{Re}\,)\hat{\psi}'(0) - i\alpha\hat{\xi}\,. \tag{2.50e}$$

Substituting equation (2.46) into the boundary conditions given by equations (2.50a–e) gives a set of 5 linear equations in 6 variables, $\{A_0, A_1, A_2, A_3, \hat{\eta}, \hat{\xi}\}$. We solve for the first five in terms of $\hat{\xi}$. This can be presented as a matrix equation,

$$\begin{bmatrix} 1 & 0 & 0 & 0 & 0 \\ 0 & 0 & 2 & 0 & 0 \\ 0 & -(3k^2 + ik\mathrm{Re}\,) & 0 & 6 & 0 \\ \hat{\psi}_0(1) & \hat{\psi}_1(1) & \hat{\psi}_2(1) & \hat{\psi}_3(1) & 0 \\ \hat{\psi}_0'(1) & \hat{\psi}_1'(1) & \hat{\psi}_2'(1) & \hat{\psi}_3'(1) & -2 + ik\bar{v} \end{bmatrix} \begin{pmatrix} A_0 \\ A_1 \\ A_2 \\ A_3 \\ \hat{\eta} \end{pmatrix} = \begin{bmatrix} -1 \\ 2 + k^2 \\ ik^3 \frac{\mathrm{Re}}{\mathrm{We}} \\ 0 \\ 0 \end{bmatrix} \hat{\xi}\,. \tag{2.51}$$

The values we find are infinite-degree polynomials in k, so we are limited to finding them numerically. The perturbation amplitudes and phases can be related through the function $f(k)$ as,

$$\hat{\eta} = f\hat{\xi}\,, \tag{2.52}$$

where f is evaluated as a power series in k.

The next task is to use the solution for the stream function to force the advection-diffusion equations for the temperature and concentration perturbations.

2.3.4 Perturbation of temperature and concentration

Now that we know how the fluid is flowing, we can solve the advection-diffusion equations for temperature and concentration, in their perturbed forms given by equations (2.42) and (2.43).

As mentioned in the discussion of the base state for concentration, we omit the x-dependence of the base concentration using the limit $\lambda_1/\mathrm{Le}\,\mathrm{Pe} \to 0$. This is a reasonable treatment, because of the small value calculated for λ_1. We have also

completed all calculations using the full x-dependent model, and found that there is little difference.

In this y-dependent concentration model, the perturbed fields are

$$T^{(1)} = \hat{T}(y)e^{\sigma t+ikx}\,, \text{ and} \tag{2.53}$$
$$c^{(1)} = \hat{c}(y)e^{\sigma t+ikx}\,, \tag{2.54}$$

and the corresponding differential equations are

$$\hat{T}'' - \left[ik\mathrm{Pe}\,u^{(0)} + k^2 + \mathcal{S}^{-1}\sigma\right]\hat{T} = ik\mathrm{Pe}\,\hat{\psi}\,, \tag{2.55}$$
$$\hat{c}'' - \left[ik\mathrm{Le}\,\mathrm{Pe}\,u^{(0)} + k^2 + \frac{\mathrm{Le}}{\mathcal{S}}\sigma\right]\hat{c} = -ik\mathrm{Le}\,\mathrm{Pe}\,c_0\mathcal{C}'(y)\hat{\psi}\,, \tag{2.56}$$

using prime notation to indicate the derivatives. The terms involving σ can be ignored, because $\mathcal{S}$ is quite large. Doing so also permits a solution of the boundary conditions as a linear problem.

Following the same procedure as for the stream function, the boundary conditions were linearised through a Taylor expansion. The linearised boundary conditions for $\hat{T}(y)$ and $\hat{c}(y)$ in the y-dependent model are,

$$\hat{T}'(0) + \sigma\hat{\eta} = \Gamma k^2\hat{\eta} \tag{2.57}$$
$$\hat{T}(0) + \hat{c}(0) = (1 - c_0\mathcal{C}'(0) - \Gamma k^2)\hat{\eta} \tag{2.58}$$
$$\hat{T}'(1) + \hat{j}(\hat{T}(1) - \xi) = 0 \tag{2.59}$$
$$\hat{c}'(1) + \hat{\xi}c_0\mathcal{C}''(1) = 0 \tag{2.60}$$
$$\hat{c}'(0) + \frac{\mathrm{Le}}{\mathcal{S}}\left(\hat{c}(0) + c_0\mathcal{C}(0)\sigma\hat{\eta}\right) = -c_0\hat{\eta}\left(\frac{\mathrm{Le}}{\mathcal{S}}\mathcal{C}'(0) + \mathcal{C}''(0)\right) \tag{2.61}$$

The presence of the concentration base state, $\mathcal{C}(y)$, in these boundary conditions justifies the use of the y-dependent model rather than the degenerate case $c^{(0)}(x, y) = c_0$. Equation (2.58) is derived from the undercooling boundary condition, and couples the perturbations $\hat{c}$ and $\hat{T}$. Equation (2.59) is derived from the heat transport to air, equation (2.12c). The number $\hat{j}$ summarizes all forms of heat flux, and can be calculated from experimental observations [20].

All the forcing terms contain the amplitude of the surface deflection $\hat{\eta}$; in fact, all the hatted quantities are proportional to $\hat{\eta}$, which has time dependence $e^{\sigma t}$. We may now safely set $\hat{\eta} = 1$ to rescale $\hat{\eta}$ out of the problem.

General solution for temperature and concentration

The next task is to solve (2.55) and (2.56), using the known power series expansion of $\hat{\psi}$ in the right hand side. This is done by by first solving the homogeneous equations, then finding a particular solution to find the general solutions for the perturbation amplitude,

$$\hat{T} = a_1\hat{T}_1 + a_2\hat{T}_2 + \hat{T}_p\,, \tag{2.62}$$

$$\hat{c} = b_1\hat{c}_1 + b_2\hat{c}_2 + \hat{c}_p\,. \tag{2.63}$$

These general solutions are then substituted into the linear boundary equations (2.57-2.61) to solve for the coefficients a_1, a_2, b_1, b_2 and ultimately σ.

The left hand side of equations (2.55) and (2.56) both have the same form – the parabolic cylinder equation. To solve the ODE, it is convenient to make a change of variable, $z = 1 - y$. Doing so, both have the form,

$$w''(z) + \big(ik\mathrm{Pe}^* z^2 - (ik\mathrm{Pe}^* + k^2)\big)w(z) = 0\,, \tag{2.64}$$

where Pe^* is Pe for the temperature, and $\mathrm{Le}\,\mathrm{Pe}$ for the concentration. The solution to the parabolic cylinder equation can be stated in terms of confluent hypergeometric functions, but for a numerical solution, it is more useful to use a power series expansion.

The power series expansion will be necessary to find the particular solution, by way of the variation of parameters. Using variation of parameters for the temperature, we find,

$$\hat{T}_\mathrm{p} = \hat{T}_2\Theta_1 - \hat{T}_1\Theta_2 \tag{2.65}$$

$$= ik\mathrm{Pe}\left[\hat{T}_2\int\frac{\hat{T}_1\hat{\psi}}{W}dz - \hat{T}_1\int\frac{\hat{T}_2\hat{\psi}}{W}dz\right] \tag{2.66}$$

where $W(z) = \hat{T}_1(z)\hat{T}_2'(z) - \hat{T}_1'(z)\hat{T}_2(z)$ is the Wronskian. Similarly, for the concentration the particular solution is,

$$\hat{c}_\mathrm{p} = -ik\mathrm{Le}\,\mathrm{Pe}\,c_0\left[\hat{c}_2\int\frac{\hat{c}_1\hat{\psi}\mathcal{C}'}{W}dz - \hat{c}_1\int\frac{\hat{c}_2\hat{\psi}\mathcal{C}'}{W}dz\right]. \tag{2.67}$$

We can confirm by symbolic series expansion that the solutions of the homogeneous equation have the nice property that $W(z) \equiv 1$. The integrals in equations (2.66)

and (2.67) can be solved to high accuracy by expanding the integrands about $z = 0$ and integrating term by term. This is done numerically.

2.3.5 The thermal perturbation boundary value problem

Finally, all that remains is to solve for the dispersion relation $\sigma(k)$ along with the coefficients a_1, a_2, b_1 and b_2 in equations (2.62) and (2.63), using the boundary conditions. Because the boundary conditions are linear, they can be represented as a matrix equation.

$$\mathbf{B}\begin{pmatrix}\sigma\\ a_1\\ a_2\\ b_1\\ b_2\end{pmatrix} = \vec{\mathbf{b}}\,, \tag{2.68}$$

where the matrix is formed from the coefficients of $\{\sigma, a_1, a_2, b_1, b_2\}$ in the boundary conditions after substituting equations (2.62) and (2.63) and the vector $\vec{\mathbf{b}}$ contains all the remaining terms.

Using the change of coordinates $z = 1 - y$, the matrix is

$$\mathbf{B} = \left[\begin{array}{ccc|cc} -f & \hat{T}_1'(1) & \hat{T}_2'(1) & 0 & 0 \\ 0 & -\hat{j}\hat{T}_1(0) & \hat{T}_2'(0) & 0 & 0 \\ 0 & \hat{T}_1(1) & \hat{T}_2(1) & \hat{c}_1(1) & \hat{c}_2(1) \\ \hline 0 & 0 & 0 & 0 & \hat{c}_2'(0) \\ -c_0\mathcal{C}(1)\frac{\mathrm{Le}}{\mathcal{S}}f & 0 & 0 & \hat{c}_1'(1) - \frac{\mathrm{Le}}{\mathcal{S}}\hat{c}_1(1) & \hat{c}_2'(1) - \frac{\mathrm{Le}}{\mathcal{S}}\hat{c}_2(1) \end{array}\right], \tag{2.69}$$

and the vector on the right hand side is

$$\vec{\mathbf{b}} = \begin{bmatrix} -\hat{T}_\mathrm{p}'(1) \\ \big(1 + c_0\mathcal{C}'(1)\big)f - \hat{T}_\mathrm{p}(1) \\ -\hat{j} \\ c_0\mathcal{C}''(0) - \hat{c}_\mathrm{p}'(0) \\ c_0 f\big[\mathcal{C}''(1) - \frac{\mathrm{Le}}{\mathcal{S}}\mathcal{C}'(1)\big] - \hat{c}_\mathrm{p}'(1) + \frac{\mathrm{Le}}{\mathcal{S}}\hat{c}_\mathrm{p}(1) \end{bmatrix}. \tag{2.70}$$

The solutions for σ and all the coefficients are functions of the wavenumber k. The size of the problem and the complicated form of all the special functions involved prevents us from finding a reasonable symbolic approximation of $\sigma(k)$, so we solved it numerically.

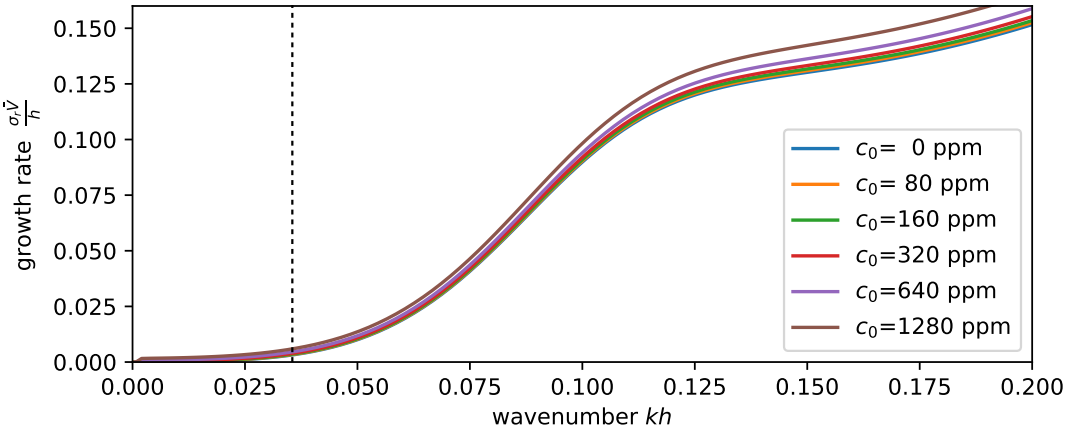

Figure 2.2: The predicted growth rate as a function of wavenumber found through linear perturbation, with varying concentrations of source water. The concentration has very little effect on the stability, only showing a slight increase for higher concentrations. The dashed vertical line indicates a 10 mm wavelength. The slight bump in the relation occurs around 2.5 mm, far from the wavelength seen in icicles.

2.4 Linear stability results

The linear stability of the generalized thin-film model was calculated numerically using a power-series expansion to 100 terms. Unfortunately, the calculations show that the model is unstable for all wavenumbers. The dispersion relation diverges to infinity for high wavenumbers regardless of dimensionless parameters.

The effect of impurity concentration on the growth rate is shown in Figure 2.2. The concentration has an insignificant effect on the stability. The insensitivity to concentration in the model can be seen in the boundary value problem for the perturbed temperature and concentration fields. The matrix describing the boundary conditions (2.69) has a primarily block-diagonal structure (indicated by the lines), which separates the concentration and temperature boundary value problems. The two problems are only weakly coupled through the $\hat{c}_1(1)$ and $\hat{c}_2(1)$ terms in the third row, and $-c_0\mathcal{C}(1)\frac{\mathrm{Le}}{\mathcal{S}}f$ in the fifth row. Due to $\mathrm{Le}/\mathcal{S} \approx 0.01$, the amplitude of the concentration perturbation, $\hat{c}$, is two orders of magnitude less than the amplitude of the temperature perturbation, $\hat{T}$. Therefore, the coupling between the temperature and concentration fields is weak, and a change in concentration will have a negligible effect on the temperature gradient through freezing point depression, and thus a negligible effect on the freezing rate.

As seen in the contour plots of the concentration and temperature field perturba-

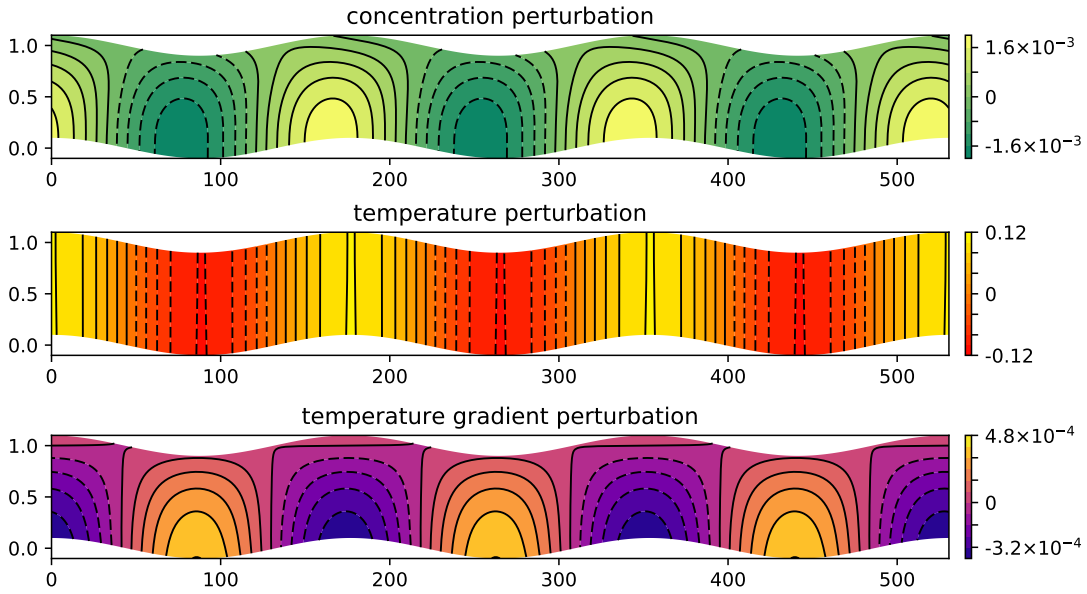

Figure 2.3: Perturbations of the concentration, temperature, and temperature gradient in the y-direction, using a wavelength of 10 mm. There is an increase in both temperature and concentration in advance of the ripple peaks due to a higher release of impurities and latent heat in those locations. The freezing rate is proportional to the thermal gradient. From the temperature gradient, we see that rate of freezing will be higher at ripple peaks. This behaviour is seen at all wavelengths.

tions, shown in Figure 2.3, the magnitude of the concentration perturbations is two orders of magnitude smaller than the temperature perturbation. As a result, variations in concentration are relatively small so the constitutional undercooling plays an insignificant role.

In the Ueno model, surface tension is seen to affect the rippling instability, but the experiments performed by Chen and Morris [12, 20] showed that the surface tension has negligible effect on the wavelength, and lower surface tensions may decrease the rippling instability. In consideration of this, we also examined the role of surface tension on the dispersion relation by varying the Weber number. In Figure 2.4, it is clear that the generalized model is affected much more strongly by surface tension than impurity concentration. The local peak in growth rate is only close to 10 mm for surface tensions greater than 10 times greater than for pure water. The strong dependence on surface tension is another result that invalidates the thin-film model for the rippling instability.

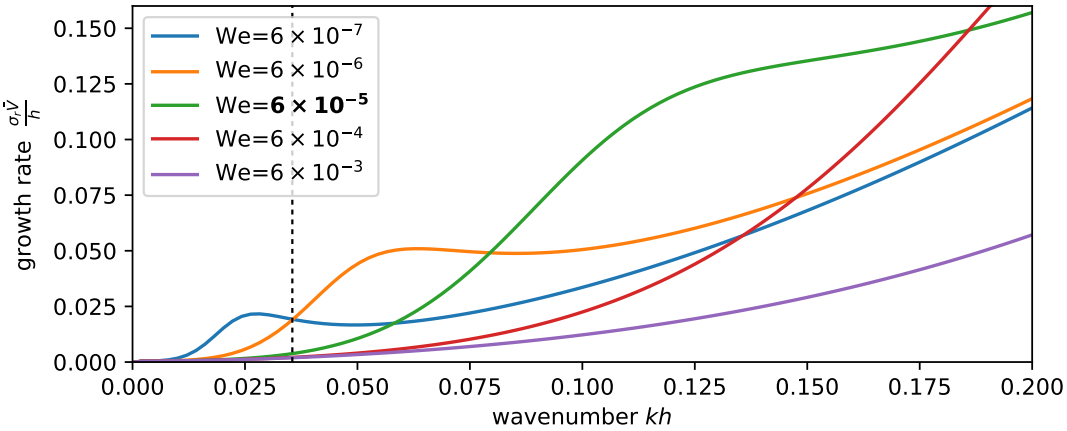

Figure 2.4: The predicted growth rate as a function of wavenumber found through linear perturbation, with varying surface tension. The dashed vertical line indicates a 10 mm wavelength. The thin-film depends much more strongly on surface tension than concentration of impurities. The relation diverges in all cases, but a local peak is found close to the expected wavelength for small values of the Weber number (higher surface tension, which is not physically reasonable).

2.5 Discussion

The fact that the linear stability analysis of the thin-film model is insensitive to concentration shows that a new approach should be taken. This could involve a weakly non-linear analysis, extension of the model with new physics, or re-assessing the assumptions made in the formulation.

A different approach to analysing the stability of the thin-film model is to use a weakly non-linear approach through gradient expansion. Performing the analysis this way would extend the work of Benney [51] to the case of an actively growing ice substrate. Bertagni has performed this weakly non-linear analysis for icicles grown with pure water, and found that the problem is stable for all wavelengths [47]. However, this approach depends on the model having no x-dependence, and cannot be applied in the case of impurities. As Bertagni states,

> "In particular, the issue is that as the aqueous solution flows down, part of the water is lost due to the freezing, but the content of impurity is preserved as the freezing ice extrudes the dissolved chemicals. This process causes a slow build-up of concentration in the vertical x direction, which cannot be addressed by the gradient expansion technique. The correct approach would be to first solve the problem of c in the x-direction,

> which we strongly believe to be responsible for the ripple instability, and then perform a stability analysis with an x-dependent base state. Such a mathematical approach is the so-called global stability analysis (Huerre and Monkewitz, 1990 [58]; Schmid and Henningson, 2012 [59]).”

A possible extension to the thin film model is to incorporate mushy layer theory, so that impurities can be trapped inside the ice. This approach has been fruitful for sea ice [60, 61, 62, 16], but has not been applied to icicles, because the amount of impurities in icicles is significantly less than the amount needed in those theories. Still, the inclusions of trapped impurities seen in icicles (see Chapter 7) suggests that a thin mushy layer is present in impure icicles. Including a mushy layer in the generalized model may increase the role of impurities, and reduce the problem of impurity accumulation down the length of the liquid film.

Despite those possible approaches, it is our opinion that an axisymmetric thin-film model of icicle growth will never explain the growth mechanisms of ripples. As seen in Chapter 6, the flow on the surface of icicles is far from uniform, instead descending in thin rivulets. The presence of impurities increases the amount of water deposited on the icicle surface, forming stagnant pools of liquid that sit on the upper side of ripples. With large regions of the ice exposed to air, a significant proportion of latent heat would be released through the ice, which has a conductivity approximately 4 times higher than liquid water. This direction of heat flux will require additional terms in the Stéfan boundary condition (2.3a), and may stabilize the growth at higher wavenumbers. It is also possible that the water is not supercooled when latent heat can be released into the ice, and the temperature of the ice can achieve temperatures below the melting point. Based on those observations, we believe a cyclic or stochastic model of icicle growth, in which the surface properties affect liquid distribution, would be a better approach to understanding the formation of ripples.

Chapter 3

The icicle machine

The failure of the thin-film model of ripple formation in Chapter 2 strongly suggests that other mechanisms are involved in icicle growth. In order to shed new light on potential mechanisms, we conducted a series of experiments by growing icicles under controlled conditions in the laboratory. For a systematic experimental study of icicle growth, it is necessary to control and monitor the both the icicle's environment and source water. This includes the source water flow rate, temperature and concentration, as well as the air temperature, humidity, and radiative heating sources. The shape of the icicle must also be measured throughout its growth. The icicle machine was created to meet all of these criteria.

A schematic of the icicle machine can be seen in Figure 3.1. The heart of the icicle machine is an insulated chamber, cooled by running antifreeze through interior insulated walls. Pre-mixed water is pumped at a controlled flow rate through a temperature-controlled nozzle onto a rotating support, and gradually freezes as it descends, forming an icicle. Unfrozen water lands in a heated drain and flows to the exterior of the chamber. The rotating support serves two purposes. First, by placing the nozzle slightly off-center and rotating the support, axial symmetry is encouraged. Second, a camera placed on one side of the chamber can capture pictures from all angles around the icicle as it rotates. The 8 minute period of rotation is slow compared to the liquid flow rate so that inertial effects from rotation do not affect the flow, but is fast compared to the growth rate of the icicle so that a full 360° view of the icicle can be taken. Pictures were taken from one side 16 times per rotation. The temperatures of the air, wall, and feed-water were measured using thermocouples. An access door on the right-hand-side of the icicle chamber permits access to the icicles during growth, and for removal so that fully grown icicles can be measured and sectioned. Results from examining the cross-sections of icicles are presented in

Chapter 7.

The details of the icicle machine design are presented in Section 3.1. The measurement components are described in Section 3.2, and the software used to control the icicle machine is described in Section 3.2.4. The method used to prepare feed-water is explained in Section 3.3.

The icicle machine, seen in Figure 3.2 was based on the machine used in previous studies by Chen and Morris [12, 45]. However, it was completely rebuilt and improved. With these improvements, the machine could be run at a wider range of temperatures, and higher flow rates. It was also possible to conduct new experiments. We were able to grow 7 icicles in one 5-day work-week – one day for cooling, and 2 icicles a day for 3 days, followed by 1 icicle and a shut-down on the final day.

3.1 Icicle machine design

The icicle machine has five main subsystems: the insulated box, cooling system, rotating support, feed-water supply, and camera and lights. The cooling system, described in Section 3.1.2, was built as an internal frame that also held the rotating support (Section 3.1.3) and all internal measurement equipment. The insulated box, was assembled around the internal frame to isolate icicle's environment from the room. The insulated box was designed to provide quick access to the internals as described in Section 3.1.1. The feed-water supply, described in Section 3.1.4, was placed behind the insulated box, and pumped water at a controlled flow-rate through the nozzle mounted to the frame above the rotating support. The camera and lights are described in Section 3.2, along with the other measurement tools.

3.1.1 Insulated box

The insulated box serves to isolate the icicle chamber from the surrounding environment, while providing quick access to the internals. It was designed as a modular system using interlocking panels for the sides and the top. Three layers of 2" isocyanate foam insulation were stacked with a PET vapour-barrier sheet bonded on the inside of each panel. 3/4" plywood panels provide support on the exterior. Spring latches hold the sides together, so that each side can be removed independently of the others. The outside dimensions of the box are 810 x 870 x 1400 mm, with an inside dimension of 465 x 520 x 1050 mm.

A removable, insulated "camera tunnel" was attached to the front of the insulated

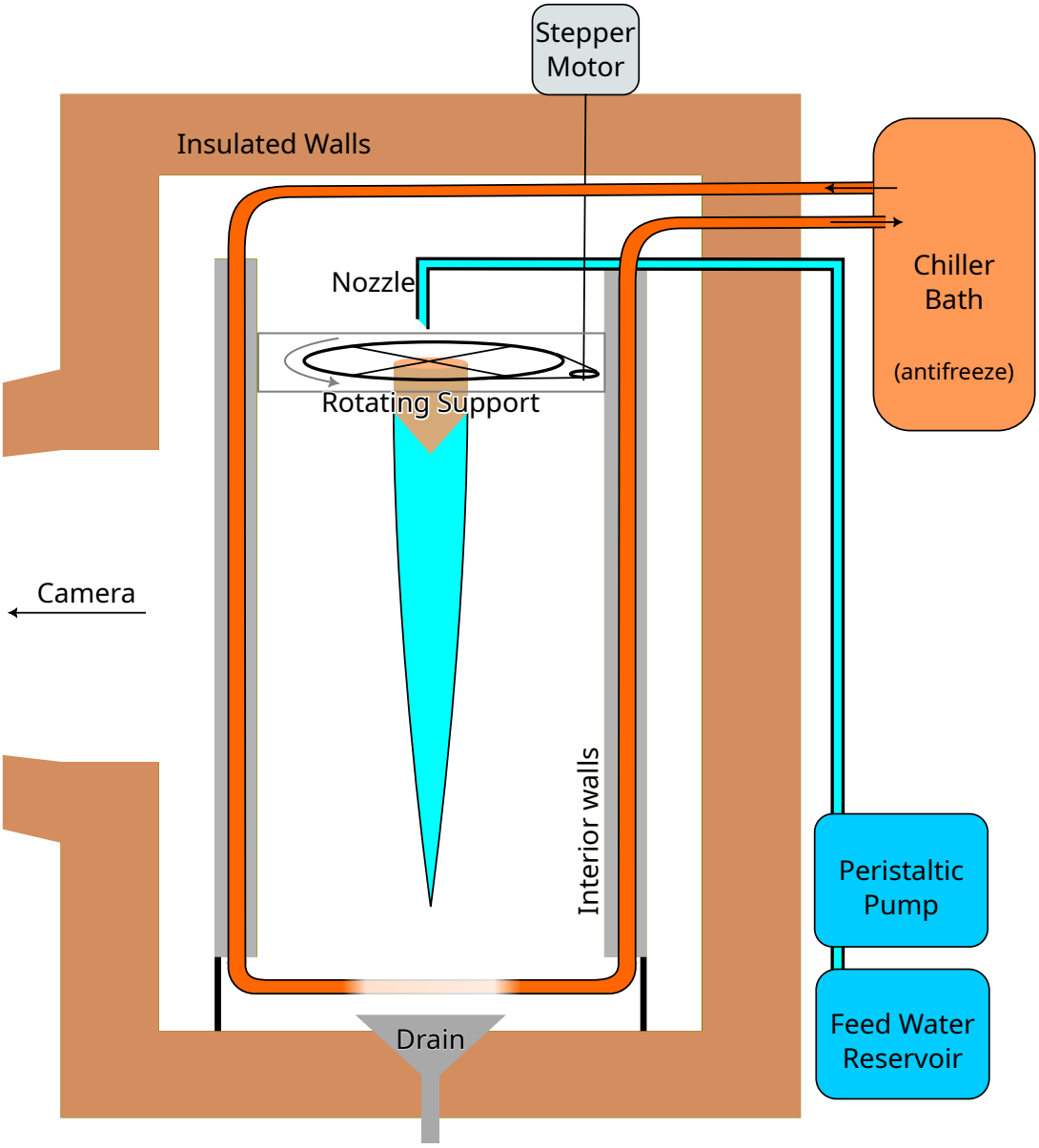

Figure 3.1: A schematic of the icicle machine. The insulated chamber is cooled by circulating chilled antifreeze through the interior. Feed water was placed on a mass scale to monitor flow rate, and pumped at a controlled rate through the cold nozzle onto a support structure. The support structure rotates, driven by a stepper motor, and an optical indexer triggers the lights and camera at fixed orientations of the icicle. Unfrozen water drips off the icicle into the heated drain, and flows to the outside of the chamber.

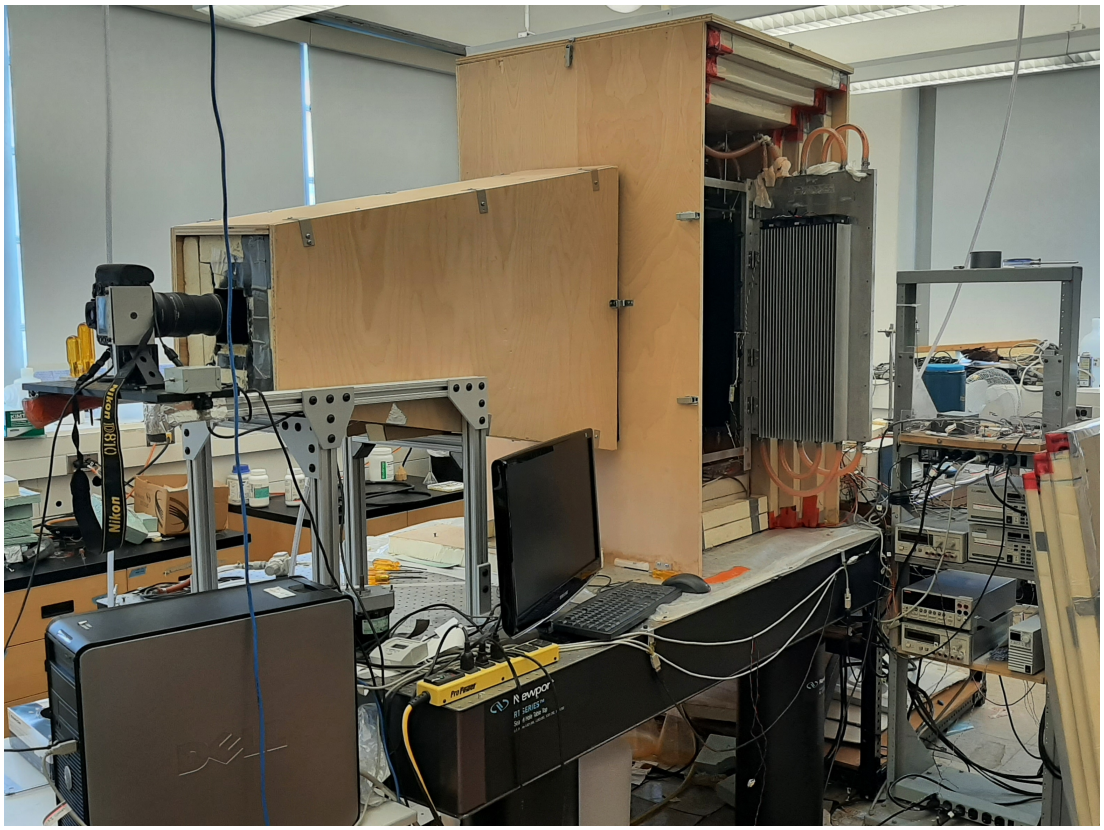

Figure 3.2: A view of the icicle machine from the right side. The right-side wall is open, with access to the icicle chamber. The camera tunnel, camera, and lab computer are shown at the left of the picture. Power supplies and electronic interfaces are in the rack on the right. The chiller bath, feed-water reservoir, and feed-water pump are behind the insulated chamber.

box, measuring 1060 mm in length. An anti-reflective glass pane was recessed in the front of the tunnel and angled downwards, minimizing glare. The camera tunnel can be seen in Figure 3.2. A steady supply of dry air was blown across the exterior of the window to prevent fogging.

All plumbing and wiring connections were made through the fixed back-panel. A heated drain was placed at the centre of the bottom under the rotating support to collect water that drips off the tip of the icicle.

The humidity in the interior of the chamber could be reduced by opening a separate dry compressed air supply while the chamber was cooled to operating temperature. In practice, supplying dry air raised the temperature in the icicle chamber by several degrees Celsius, and could not keep up with the humidity introduced by the feed-water supply, so it was only used during the initial cool-down to reduce frost buildup.

3.1.2 Cooling system

The cooling system is comprised of an internal structure that is cooled with antifreeze supplied from an external chiller bath. The antifreeze was chilled with a Thermo Scientific® HAAKE A 40 water chiller and HAAKE AC 200 circulating pump and controller. The interior structure which forms the icicle chamber is shown in Figure 3.3.

The antifreeze circuit passes through the rear of the icicle chamber to a series of pipes inside the interior aluminum walls. These aluminum walls were made of four separate panels assembled onto a frame, thermally isolated from the bottom of the chamber. Each panel was constructed from two 3/8 inch sheets of aluminum, sandwiched around 3/8 inch copper pipes that run through cylindrical grooves. Vertically-finned aluminum heatsinks measuring 80 x 250 x 610 mm were bolted to the left and right walls of the chamber for additional cooling and thermal mass. All mating surfaces were assembled with thermal paste between them to maximize cooling efficiency.

Circulating fans were attached to the top of the finned aluminum heatsinks to blow air downwards, maintaining an even temperature distribution top to bottom. With the fans blowing, the air temperature could be maintained within a range of 0.5°C from the top to the bottom of the icicle chamber. A sample plot of the temperatures inside the icicle chamber is shown in Figure 3.4. Having turbulent air inside the chamber also suppresses the tendency for icicles to grow multiple tips [45].

The large thermal mass of the interior walls provides a stable temperature – constant to within ±0.1°C at the cost of fine control. Before each icicle, the chiller

Figure 3.3: A close-up of the icicle chamber interior. The interior aluminum walls form a frame to hold the lighting, thermocouples, and rotating icicle support. The interior walls are cooled with antifreeze that circulates through them. The open door has one set of circulating fans and a heatsink, with the other fans and heatsink attached to the opposing wall. Black velvet is suspended by four corners at the back of the chamber to provide a contrasting background.

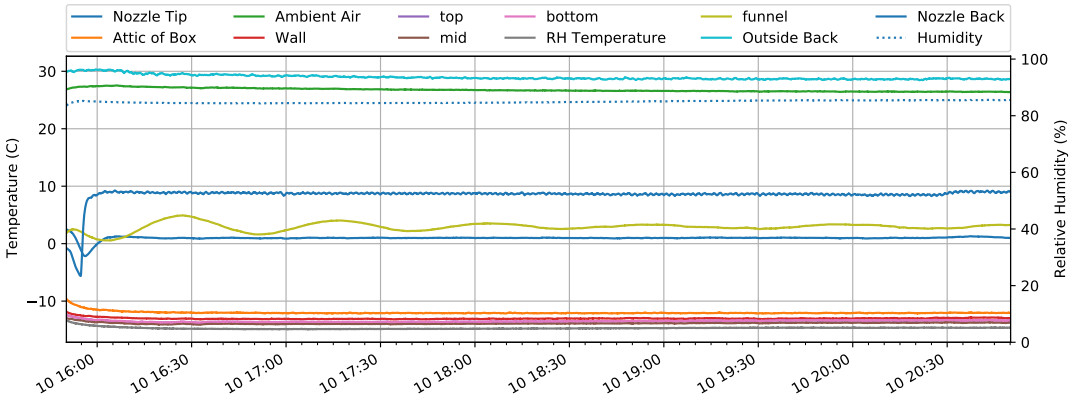

Figure 3.4: An example of the typical temperature and humidity measurements taken while an icicle is grown.

bath is set to a fixed temperature. For example, setting the bath to -18°C establishes a typical air temperature of -14°C. After the icicle is grown, the control software automatically reduced the bath to -21°C, in order to keep the chamber cold while the box is opened to remove the previous icicle, and install the new icicle support.

The aluminum walls create a frame that supports the rotating icicle support, nozzle and instrumentation. The whole assembly is attached and thermally isolated from the table using an acrylic frame.

3.1.3 Rotating icicle support

The rotating icicle support and nozzle are what make this an icicle machine, rather than simply a cold box. The support rotates so that pictures can be taken from all angles. Using wingnuts, the icicle substrate can be swapped-out quickly, so that fully grown icicles can be removed, and the next icicle can be started with little down-time.

The substrate for the majority of icicles was a short wooden dowel, suspended from a turntable by a Delrin® cross. Alternatively, a preformed cylinder of ice could be used as the substrate as seen in Section 6.4. The turntable is belt-driven from a stepper motor mounted to the top of the icicle machine, and rotates with a period of 8 minutes. The rotating support assembly is shown in Figure 3.5.

The 8 minute support rotation period was fast compared to the time it takes to form an icicle (at least 4 hours), but slow compared to the fluid mechanical time scale of the water flow. The centrifugal acceleration produced by rotation was negligible compared to the acceleration due to gravity. Rotating the support encourages axial symmetry in the icicle, and allows the icicle to be pictured from all sides during

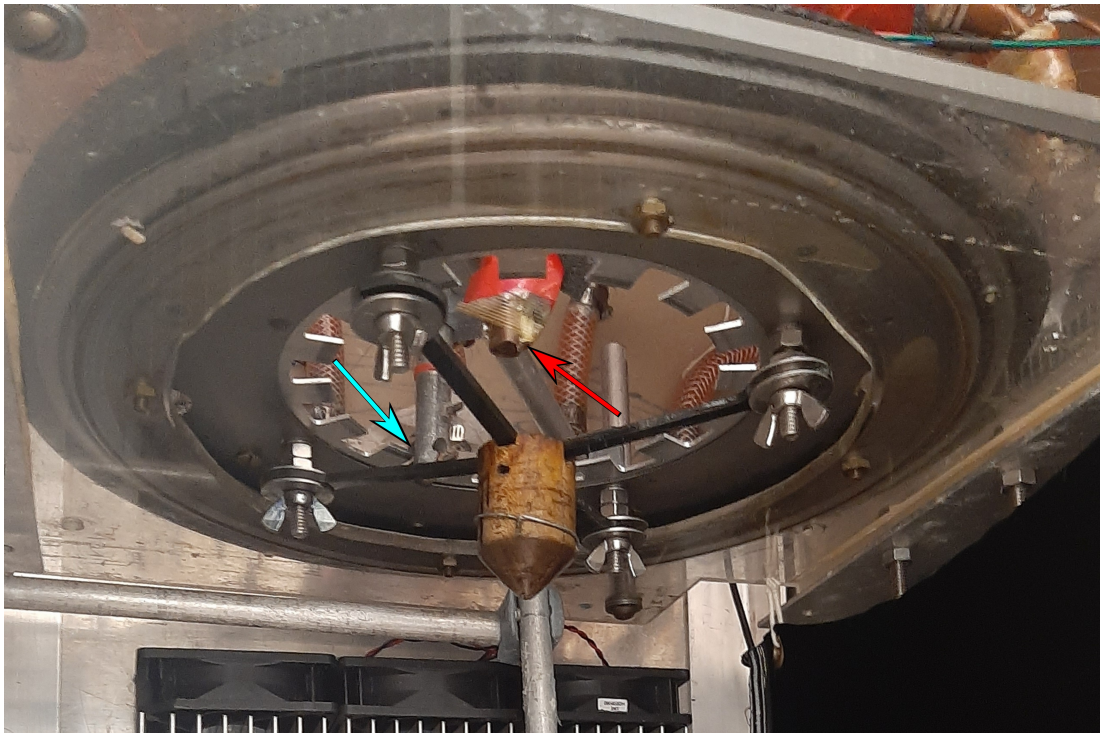

Figure 3.5: The rotating support for the icicle support. Water drips from the nozzle (indicated with the red arrow) onto the wooden cone. The icicle can be removed using the wing-nuts. The index wheel has 16 teethed spaced at regular intervals and passes through an optical interrupter indicated with the blue arrow

growth.

A toothed disc rotates along with the support, and passes through an optical interrupter. This indexing wheel accurately registers up 16 equally-spaced orientations of the icicle used for the camera control (Section 3.2.1). An additional indexer that triggers once per rotation was added, to establish a consistent zero-index so that the icicles can be oriented in the sectioning process.

3.1.4 Feed-water supply

The feed-water system provides a controlled flow of cold water to the icicle substrate through a nozzle placed above the icicle support. The source water is premixed as described in Section 3.3. After the solution is prepared in a flask, it is placed on a USB-connected mass scale to monitor the flow rate. The water is then pumped from the source-water reservoir to the nozzle using the peristaltic pump shown in Figure 3.6. The speed of the pump was controlled with a feedback loop using the LabView module described in Section 3.2.4.

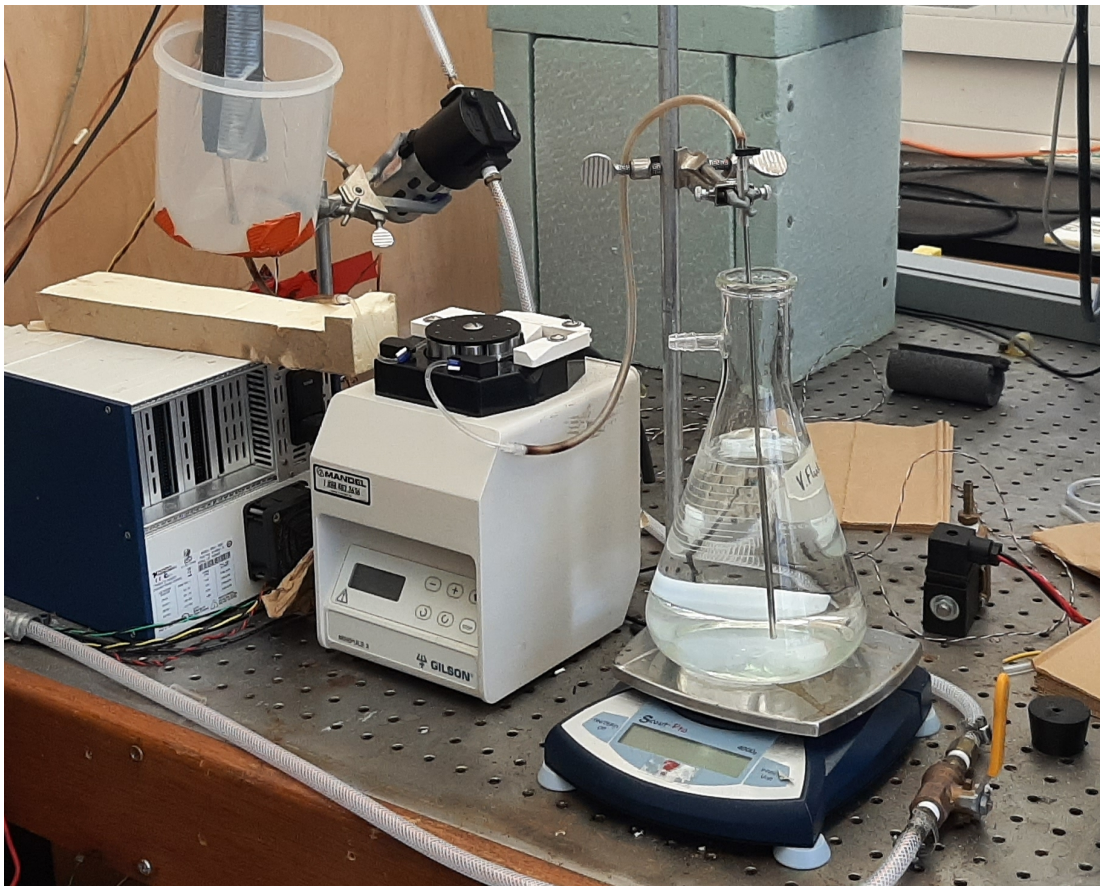

Figure 3.6: Feed-water system for the icicle machine. Water is placed on the mass scale, and pumped into the machine with the peristaltic pump. The feed-water tube passes through the plastic tub, where ice can be added if the feed-water needs pre-cooling. Pre-cooling is only necessary for warmer temperatures in the icicle chamber.

The nozzle is a 1/8" OD copper tube that is clamped to a copper heat-sink, which is, in turn, thermally coupled to the cold aluminum wall. Heating pads were strapped around the nozzle and heat-sink and controlled by the computer with a feedback loop, to maintain a constant nozzle temperature. The temperatures for the nozzle tip and back were both monitored with thermocouples, but only the tip was used for the feedback control. If extra cooling was needed, ice was be placed in a bucket around the hose before entering the icicle chamber.

For almost all icicles that we grew, the nozzle tip was held to just above the freezing point at +1°C. Maintaining a lower temperature was unreliable, because ice would form inside the nozzle, while higher temperatures would prevent the icicle from forming.

3.2 Measurement equipment

While growing, icicles were observed with a 36 MP DSLR camera (Nikon D810), managed through LabView on the computer. The icicle chamber was illuminated using white LED strips that were turned on only while a picture was being taken. The camera and lighting system is detailed in Section 3.2.1. A reference length-scale is held in-frame beside the icicle so that topography and area measurements could be calculated for each image. The design and calibration of the scale is explained in Section 3.2.3.

While the icicles grew, we monitored the temperature of the wall, air, and feed-water using Type-J thermocouples. Relative humidity was monitored with a USB-connected solidstate humidity sensor. The details of sensor placement are described in Section 3.2.2.

3.2.1 Camera and lighting

A 36 MP SLR camera (Nikon D810) was placed at the front of the icicle machine, pointed down the length of the camera tunnel. The camera was levelled and placed so that the lens was 1650 mm from the centre of the icicle chamber. The camera was set in manual mode with a fixed aperture, ISO, shutter speed and focus so that exposure was consistent for all pictures. All pictures were stored in raw format (`.NEF`), then converted to 16-bit-depth `PNG` for analysis.

The lab computer was used to control the camera and capture pictures. Using the index wheel on the rotating support (Section 3.1.3), images were captured at at 16 evenly spaced, indexed, angular support positions. The angular orientation and time of capture were stored in a table for each image. The white LED strip lighting was turned on only for image capture. A black velvet background was suspended behind the icicle for contrast.

3.2.2 Temperature and humidity

All temperature measurements were taken with Type-J thermocouples connected to a National Instruments NI SCXI-1303 isothermal terminal block. The terminal block has a high-accuracy thermistor cold-junction temperature sensor to correct for temperature drift.

A total of nine thermocouples were connected. Five were used for temperatures relevant to icicle-growth models, and an additional four were used for control and

performance monitoring. The temperatures measured were:

Air temperature Bottom, middle, and top probes placed 36 cm, 55 cm and 70 cm from the bottom of the icicle chamber;

Wall temperature Fastened to the middle of the left-side interior wall;

Nozzle temperature Attached to the nozzle tip; and

Additional monitoring included chamber attic (above the support), room air, chamber drain, and back of the nozzle.

Humidity within the chamber was continuously monitored by a probe (Dracal USB-TRH300) placed in the upper-rear-left of the icicle chamber. Measurements of humidity are difficult below the frost point [63]; we pumped desiccated air into the chamber during initial cool-down, but the relative humidity rose quickly to approximately 85% once the water drip started to form an icicle. A small amount of evaporative cooling contributes to the heat transfer away from the growing ice [46].

3.2.3 Length scale

The length scale inside the icicle chamber is a custom print on polyester fabric that is adhered to a poly-ethylene ruler. The scale is suspended on an adjustable mount, parallel to the central axis of the machine, in the same image plane as the grown icicles. For human readability, major ticks are marked and labelled every centimeter, and minor ticks are marked at 2 mm increments. Red circles are printed at the top and bottom of the scale, 409.5 mm apart as measured (the 0.5 mm discrepancy was due to poor adhesion to the substrate). The red circles were used for robust and accurate feature detection in the image-processing software for calculating the image resolution.

To rule out any issue from the custom scale in the icicle machine, we assessed sources of error due to position of the scale, and thermal expansion. Those two sources of error were analysed independently, by (a) taking a set of pictures with the scale randomly moved at room temperature; and (b) cooling down the icicle machine, taking pictures every 30 minutes. The resolution was calculated for each image (29 images for position, and 14 during cool-down). The calibration measurements are shown in Figure 3.7.

The position of the scale introduces a random error for each icicle grown, because the scale often needed to be adjusted after replacing the icicle support. To assess

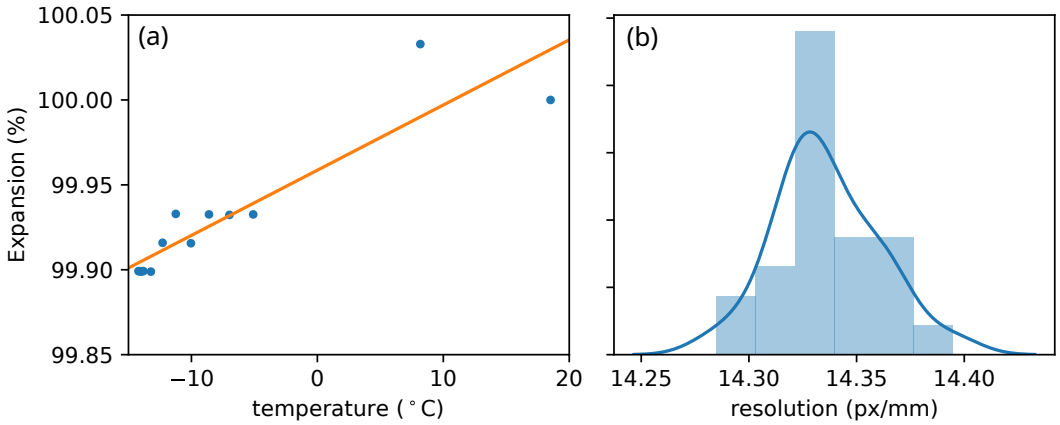

Figure 3.7: Calibration results for the scale. The thermal expansion is shown in (a), and the effects of scale position on calculated resolution are shown in (b).

this error, 29 images were taken with the scale randomly perturbed in position and orientation. Calculating the resolution for each of the images, we found a relative error of 0.17%.

Cooling the scale introduces a consistent shrinking of the scale due to thermal expansion. Fitting a line to the measured length of the scale as it cooled, we calculated the coefficient of thermal expansion to be 34×10^{-6} K^{-1}, which is less than the 120-200$\times 10^{-6}$ K^{-1} quoted by manufacturers for high-density polyethylene. At -14°C, our calculated thermal expansion would amount in a 0.13% reduction in length.

Combining all error sources, a measurement of 10 mm in the image would be 9.998 ± 0.017 mm. These errors are insignificant compared to the uncertainties from the wavelength measurement calculations. The standard deviation in peak-to-peak width is typically between 2 and 3 mm, with a standard error of about 0.5 mm for each wavelength measurement.

3.2.4 LabView software

All components of the icicle machine were controlled and monitored using LabView®. LabView is a software package in which the user can program modules called *visual instruments*, which provide a graphical interface to control and read from connected hardware. Visual instruments are programmed graphically with block diagrams.

The control software for the icicle machine is split into four primary modules. The "temperature monitoring" instrument monitors all temperatures, and controls the nozzle and drain temperatures. The "pump controller" monitors the mass of water in

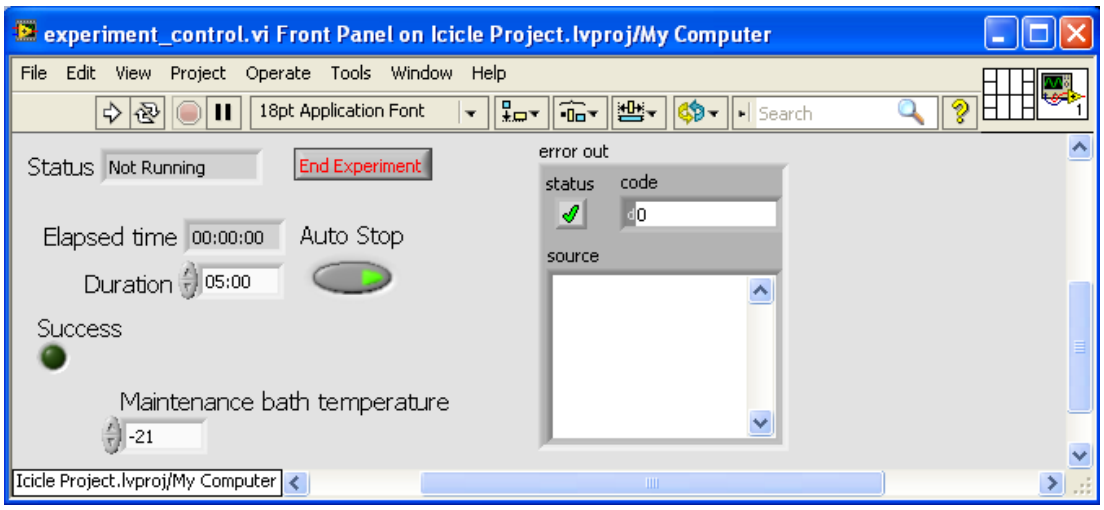

Figure 3.8: The icicle machine supervisor interface. The duration of icicle growth chiller temperature between icicles can be set, and the experiment can be manually stopped. When started, the data directories are created, and all virtual instruments are started. After the experiment is stopped, the nozzle is purged, all virtual instruments are stopped, and the chiller bath temperature is set to the maintenance bath temperature.

the reservoir and controls the flow rate. The "camera control" instrument monitors the index wheel, and takes pictures at prescribed icicle orientations. The "motor control" starts and stops the rotating support and chooses its direction. Usually the motor control is simply set to "on" and rotates the icicle clockwise.

The process for starting and stopping a single icicle run was automated using the run-supervisor instrument. When this VI is run, it creates a new directory to store pictures and data, then restarts all VIs that must be running. After the icicle has been growing for the designated time, data logging is stopped, the feed lines are run in reverse to prevent the nozzle from freezing, and the chiller bath temperature is lowered. Setting the temperature lower between runs is necessary, because the icicle chamber warms significantly when it is opened to remove the icicle and replace the support.

Temperature controller

The temperature controller VI handled saving and controlling all of the temperatures in the icicle chamber. Every 2 seconds, the controller read the temperatures from the thermocouples and saved them into `<icicle-name>/Temperatures.lvm`. The nozzle and drain heaters voltages were set using proportional control – the voltage

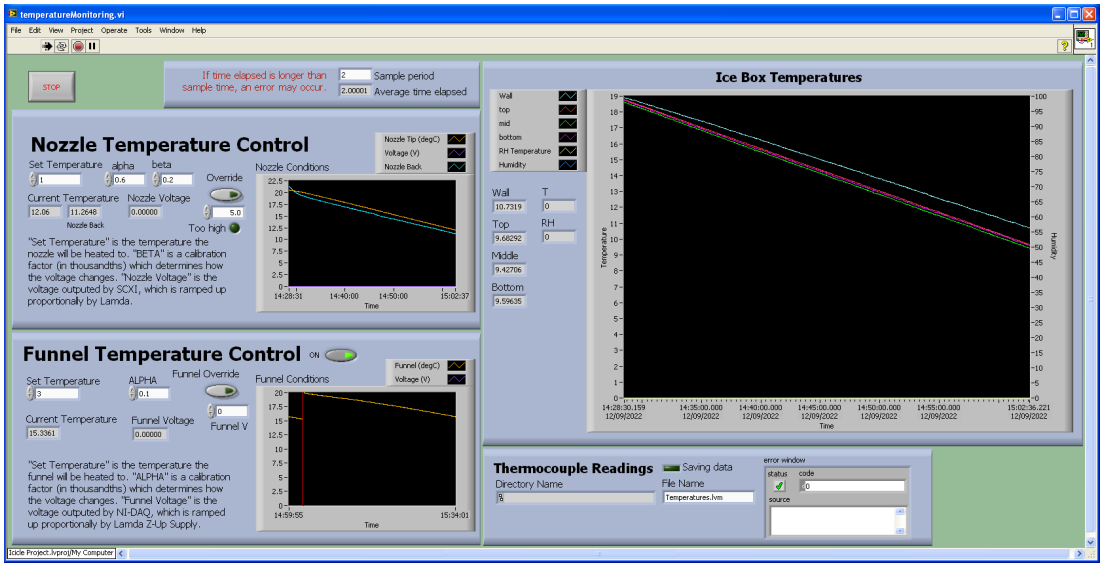

Figure 3.9: The temperature monitoring visual instrument. The nozzle and funnel temperature control parameters can be set on the left. All icicle chamber temperatures and relative humidity are shown in the right panel.

was increased proportional to the square of the difference between the measured and target temperatures. An extra derivative term was included in the nozzle controller to prevent overheating as the desired temperature is targeted.

Flow rate Controller

The flow rate controller was in charge of saving the weight of water in the feed-water reservoir, and setting the speed of the peristaltic pump. Every 2 seconds, the controller read the water weight from the USB-connected scale, and saved the value into `<icicle-name>/WaterWeights.lvm`. The nominal flow rate was set using the interface, and converted to a voltage value to control the peristaltic pump speed. Because the relation between pump speed and flow rate is dependent on the properties of the plumbing, the output voltage is controlled using an integration controller. With active control set, the flow rate is accurate to 0.05 g/min.

An additional "ramp" function was included in the flow controller to gradually increase the flow rate. Based on the thin-film model, increasing the flow rate would keep the Reynolds number constant throughout icicle growth. However, based on the observations of surface liquid distribution in Chapter 6, the Reynolds number from the thin film model is inaccurate, so we chose to use a constant flow rate in all icicles to simplify the analysis.

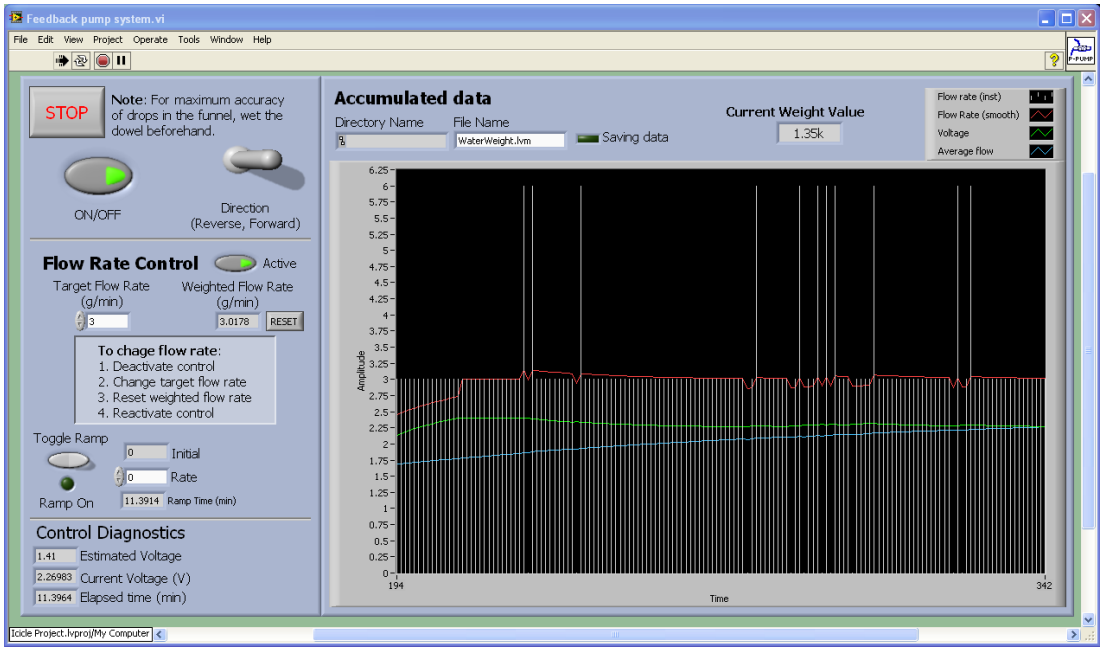

Figure 3.10: The pump controller interface. The plot on the right pane displays the change in mass between samples, the integrated flow rate, the output voltage for the peristaltic pump, and the average flow rate from the beginning. The direction and flow rate can be set using the controls on the left-hand side.

Camera and Lights controller

The camera and lights controller handled all picture-taking of the icicles. When a signal arrived from the optical indexer, the VI turned on the lights, took a picture with the camera, saved the picture to `<icicle-name>/raw_pictures/`, then turned off the lights again. Each picture was saved as `<frame-number>-tab<tab-number>.nef`, where `<frame-number>` tracks the order of pictures taken and `<tab-number>` tracks the orientation of the icicle based on the index-wheel on the rotational stage. The "absolute index" of the tab could be set using a second optical indexer that only triggered once per rotation. Times for each picture were saved to `<icicle-name>/picture_times.tsv`. In addition to triggering based on the index wheel, pictures could also be taken at fixed time intervals, or manually using the "Take Picture" button.

Motor controller

The motor for the rotational stage was controlled using a stepper motor controller driven by a 555-timer. The period of rotation was tuned using a trim potentiometer. The motor controller VI was only used to enable/disable the motor and set the

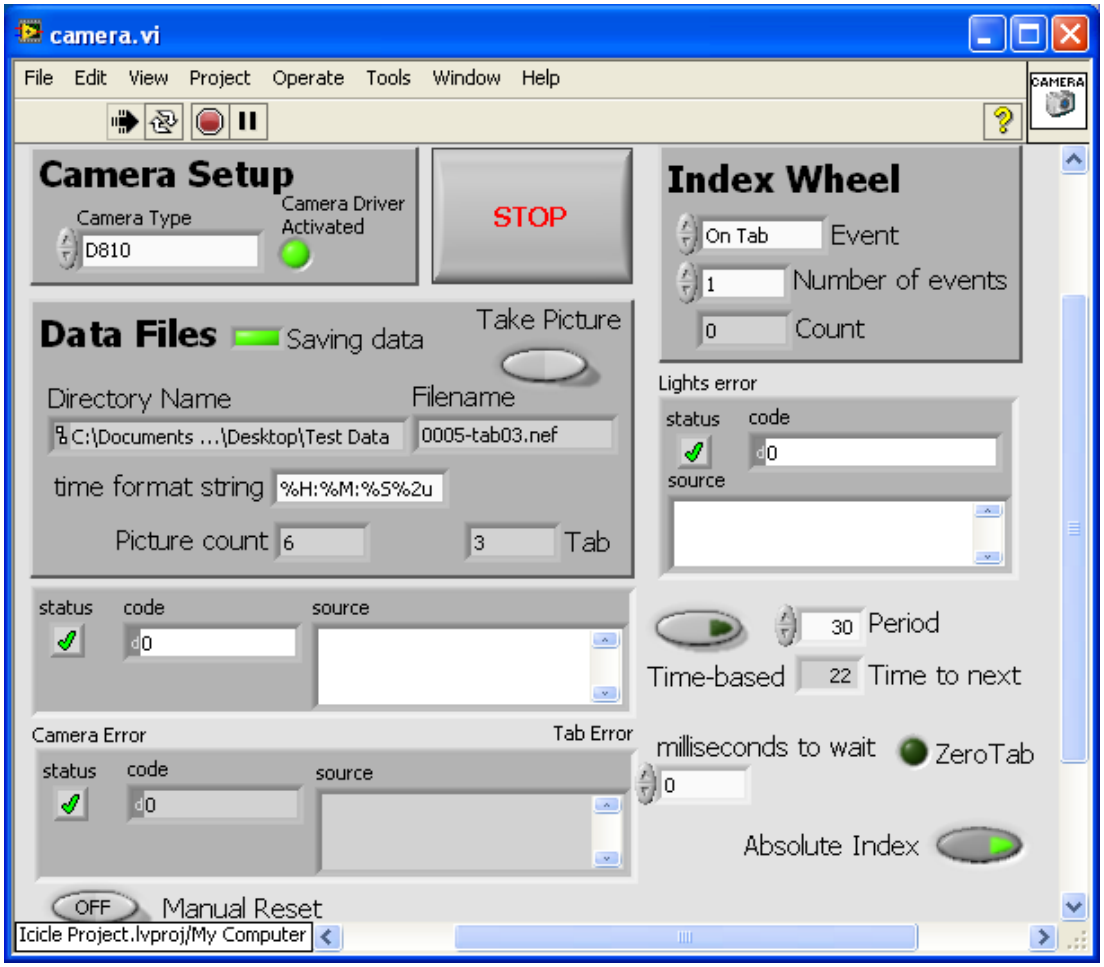

Figure 3.11: The camera control visual instrument. The current picture count and filename are shown in the "Data Files" panel. The timing and number of pictures per rotation can be set in the "Index Wheel" panel. Pictures can also be taken manually using the "Take Picture" button, or set on a timer using the controls on the bottom-left. Errors from the camera interface is shown, because it is sensitive to the settings on the attached camera.

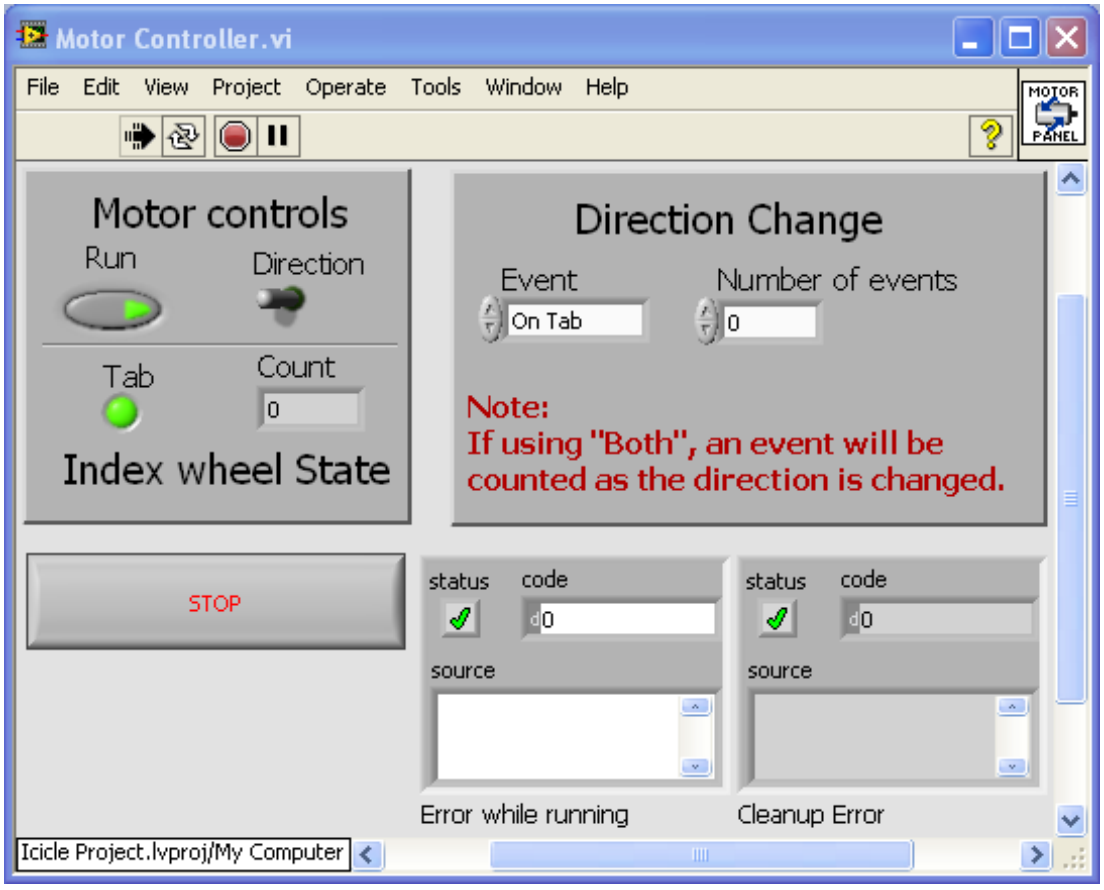

Figure 3.12: The motor control visual instrument. The direction and status are controlled using the "Motor controls panel". The "Direction Change" panel can be used to switch the direction of rotation after a number of rotations, but this wasn't used for any experiments in this thesis.

direction of rotation.

3.3 Feed-water preparation

The feed-water used to grow icicles was prepared by mixing anhydrous impurities into distilled water. Lower concentrations were achieved through subsequent dilutions.

Each icicle grown consumed roughly 900 mL of feed-water. When a new series of icicles was started, a single impurity was added to approximately 1.8 L of distilled water. Half of the mixed water was poured into the feed-water reservoir. The remaining mixture was then diluted with equal parts of distilled water for subsequent icicles in the series.

All icicles grown after March 2019 were grown with degassed water. The feed-

Table 3.1: Dissolved cation concentrations (in ppb) in the distilled water as measured by ICP-OES, sorted by concentration. Note that these concentrations are all lower than the most dilute calibrated standard (0.1 ppm) except Ca^+ and Na^+.

Na^+	495.7	Ca^+	121.5	K^+	56.0	Si^+	30.8	Zn^+	16.6
B^+	10.0	Mg^+	8.5	Se^+	7.4	As^+	5.7	Sb^+	4.7
Cu^+	4.5	Ni^+	3.5	Al^+	3.4	Tl^+	3.3	Mo^+	2.5
Cr^+	2.0	Pb^+	1.7	Ag^+	1.4	Cd^+	1.0	Ti^+	0.96
Be^+	0.86	Ba^+	0.72	Co^+	0.32	Mn^+	0.53	V^+	0.56
Fe^+	0.062								

water was degassed under vacuum for 10 minutes using an aspirator while being stirred with a magnetic stirrer. After degassing, the vacuum flask was placed directly on the feed-water scale to avoid re-introducing dissolved gasses.

Distilled water for early icicles was purchased from Puretap (Puretap.ca). Later icicles were grown using distilled water from the University of Toronto Undergraduate Physics Laboratories (UPL). The UPL distilled water undergoes a 2-stage process: first tap water is filtered through charcoal and membrane filters, then it is distilled and stored in a large (100L) Nalgene bottle.

We analysed a sample of the UPL distilled water using ion-chromatography by optical emission spectroscopy (ICP-OES) [1]. The ICP-OES equipment used can only identify positive ions. The summary of cation concentrations in the UPL distilled water is presented in Table 3.1.

To account for the non-zero concentration of distilled water, we add a molal concentration of 0.056 mMol/kg to all icicles in our analysis. This value is significant for 18 icicles in the full data set (11 grown with distilled water, and 7 grown with sodium fluorescein).

3.4 Sectioning Box

In order to observe the inclusions inside of the interior of the icicle (Chapter 7), we built a simple refrigerated box. The box is a simple construction out of the same insulation foam used for the icicle chamber. It was cooled on one side using circulating fans and a radiator chilled with antifreeze. The internal temperature was never below 0°C, but was cold enough to reduce melting.

[1] Thermo Scientific iCAP Pro ICP OES at the Analytical Laboratory for Environmental Science Research and Training (ANALEST), Department of Chemistry, University of Toronto.

Icicles were illuminated with a directional light source placed to the right of the box, or with a strip of UV-LEDs at the top of the box. The camera was mounted above the box on a frame. A black rubber mat was placed under the icicle sections for a dark background. The entire frame was covered by a black drop-cloth to block out light from the room. The refrigerated box and camera frame are shown in Figure 3.13.

The same box and camera were used for cross-polarized photography, which was used to view the grain structure of icicles. In that case, a white LED panel was placed at the bottom, and the icicle section was sandwiched between two polarized filters.

Figure 3.13: The refrigerated box and camera frame used to take pictures of sectioned icicles. The aluminum plate used to create the sections is shown to the left of the box.

Chapter 4

Morphology analysis methods

The foundation of all morphology analysis is accurately extracting the edges of the icicle from each image. The edge extraction process is sensitive to lighting conditions and dirt or frost on the background, which will cause either missing or false values. The 3-step process we used to extract icicle edges is explained in detail in Section 4.1. Using the extracted edges, it is possible to construct a full picture of the icicle's topography as it changes throughout growth.

With approximately 700 images per icicle, each with a left and right side, efficiently and reliably extracting topographic data is a challenge. The methods used need to be robust, automated, widely applicable to many icicles, easy to repair and check, and measure the same quantities as past work.

We reduce the topography of an icicle into set of five values so that individual icicles can be compared. These are split into measures of global morphology and rippled morphology. The measures of global morphology include the radial growth rate and elongation rate of icicles, as explained in Section 4.2. The rippled topography is quantified through ripple wavelength and ripple amplitude. In previous experiments, Chen *et al.* [12] considered the growth rate of ripple amplitude, but here we focus on the maximum ripple amplitude. The details of how ripples are measured and the reasons we chose those particular measurements is described in Section 4.3.

Ripples are also seen to migrate on the icicle surface during growth. The direction of migration is consistently upwards in concentrations below 320 ppm NaCl, but becomes unpredictable above that concentration. The process to track ripple peaks during growth is explained in Section 4.3.3, and the migration of ripples was compared to the pattern of inclusions in Chapter 7.

For a subset of icicles, we also measured the liquid distribution on the surface of icicles, and patterns of inclusions seen in cross-sections of icicles. The methods of

those measurements are explained in the chapters explaining those results (Chapter 6, and Chapter 7).

4.1 Edge Extraction

The first step in analysing the icicle morphology is accurately extracting the edges of the icicle. Image edge extraction is well-established, but in our case, it is sensitive to lighting conditions and dirt or frost on the background. Poor contrast can lead to missing values in the icicle edge, while frost will produce false values. Low contrast makes detecting edges for transparent icicles particularly challenging, but increasing the contrast also increases the sensitivity to non-icicles features in the image.

With perfect images, edge extraction is simple: (1) use an existing edge-detection method like the *Canny filter*; then (2) find the first edge-pixel from the left (or right) along the length of the image. However, no picture is perfect, so additional steps were used to pre-condition the image, and clean up the extracted edge post-extraction. The 3-stage process is:

1. pre-condition the image to adjust contrast, and use an optional mask;
2. extract the edges using a Canny edge detector;
3. clean up the edges with a basic "in-painting" algorithm.

Enhancing the contrast ensures that all pixels that may be the icicle edge are identified, while the clean-up step removes all falsely identified pixels. The extraction steps are detailed in the following sections.

4.1.1 Pre-conditioning

The primary pre-conditioning process is to increase the contrast in dark regions of the image using a "gamma" value. With pixel values $I[x, y] \in [0, 1]$, they can be adjusted to enhance contrast using the transformation,

$$I'[x, y] = (I[x, y])^{\gamma},$$

where γ controls contrast in the dark or light regions of the image. Using $\gamma < 1$, contrast is increased for darker pixels, while $\gamma > 1$ increases contrast for brighter pixels. We use a nominal value of $\gamma = 0.4$, which was found to be effective for most icicles. This value can be adjusted on any one icicle as needed. This step

greatly improves the edge extraction of transparent icicles. In some cases, the higher contrast needed to find the icicle edge also increases the significance of other features like frost or reflections on the backdrop. An optional masking step can be used to remove those features from the image.

Masking (optional)

If too many non-icicle features are identified by the Canny edge filter, a "mask" could be used to remove the background. The mask used was a subtractive mask: with $I[x, y]$ as the image, and $M[x, y]$ as the masking image, the conditioned image is,

$$I'[x, y] = I[x, y] - aM[x, y]$$

where a is a factor to "strengthen" the mask.

The mask can be selected as either the first image taken before the icicle starts growing, or a previous image of the icicle at the same orientation. Using the first image works best for objects that don't change during growth, while. The tab-indexed mask is more effective for objects that change during icicle growth. To account for jitter, a Gaussian blur is applied to the mask, and the additional factor $a > 1$ is used to ensure the features are fully removed.

This masking step was only necessary for a few icicles, because the clean-up step in Section 4.1.3 was sufficient to remove false features in all but the worst cases. After the image contrast was improved, the edge extraction was performed.

4.1.2 Canny edge extraction

The actual edge extraction was performed with a Canny edge detector from the *Scikit Image* package [64]. The most significant parameter to adjust was `sigma`, the standard deviation of the Gaussian filter. We found that a value of `sigma = 2.5` worked well for most icicles.

After the Canny filter was applied, we scanned the image from the left (or right) side of the image to find the first edge pixel. This procedure finds the *raw edge*, $E[y] = x$, for the left and right sides of the icicle.

The *raw edge* is highly sensitive to any noise or objects in the background, and thus requires an additional step to "clean up" the data. For this, we used an "in-painting" method that selects pixels that are in-line with nearby icicle edge pixels, as described in the next section.

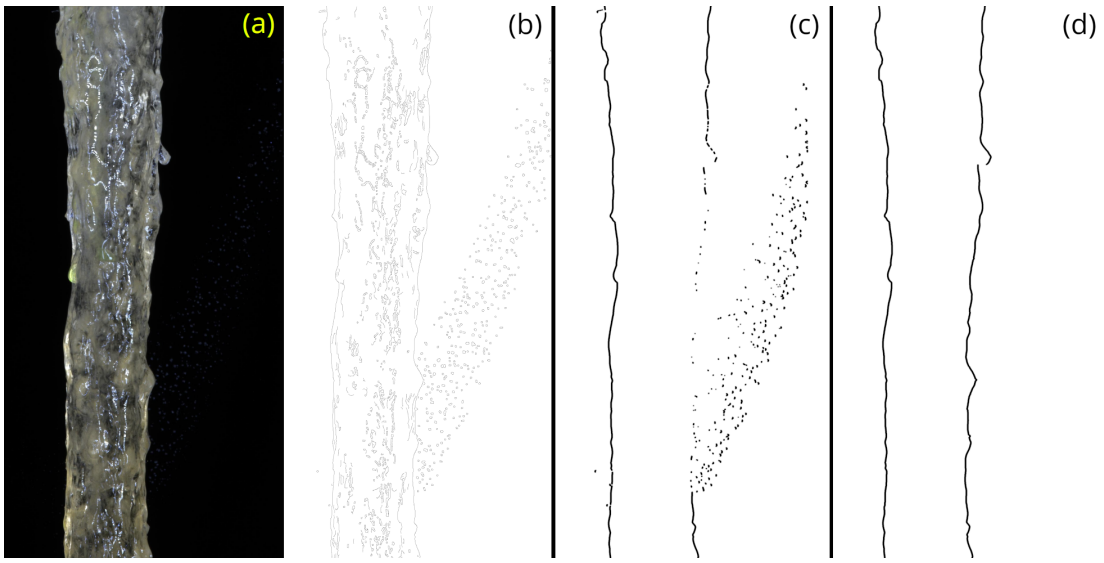

Figure 4.1: An example of cleaning up the icicle edge with frost on the backdrop. The frost is barely visible in the original image (a), but is significant after the Canny filter is applied (b). The raw edge extraction (b) prefers the frost on the right edge, but the actual icicle edge can be found using the "in-painting" method (d).

4.1.3 In-painting

The task to remove the gaps or false-positives in the edge data was the most challenging. A naive approach to denoise the edge was particularly unreliable, so we chose to use a more sophisticated approach based on in-painting methods. The in-painting method extrapolates out from a confirmed icicle edge by selecting the best candidate from the set of canny-detected edge pixels.

The effectiveness of this method can be seen in Figure 4.1. In that case, almost all information in the region with frost on the background was lost in the raw edge, so denoising would not be possible. Tracing the icicle edge in the Canny filtered image accurately identified the icicle edge.

The foundational assumption of the in-painting method is that the icicle edge is uniformly continuous. Because we are using discrete functions, we use a Hölder condition,

$$|E[y_1] - E[y_2]| \leq C|y_1 - y_2|^{\alpha} .$$

The Hölder condition sets a maximum difference between adjacent pixels, C, and also a limit for quickly the function can change at a distance, α. The parameter α is particularly useful when there is a gap in the edge. We used $\alpha = 1/2$ for all edges.

In-painting algorithm

The first step in the in-painting algorithm is to identify continuous regions, and remove the poor regions. Boundaries of continuous regions are locations where there is a significant jump in value: $|E[y] - E[y+1]| > C$, where $C = 4$ px ($\sim$0.3 mm) is typically used. The quality of a region is based on two factors: (a) the length of the region, and (b) the mean value of the region.

Shorter regions (less than 100 pixels) are more likely to be non-icicle features, like frost or an ice-spike. Regions with a mean value that is too low (left side of the image) are likely the in-chamber scale. A high mean value indicates that the region could be the edge of the camera tunnel.

After the "bad" regions are identified and removed, we "paint" in the edge from the top or bottom of each bad region using the Hölder condition. The basic algorithm is rather simple:

0. Store the edge value, $v = E[y_0]$, from the adjacent region.
1. Calculate the permissible range of values, $r = ck^{1/2}$, where k is the distance from the current stored value.
2. Look for the best candidate from the Canny edge filter results, $v_{\text{next}} = \arg\min_x \{|x - v| : I_{\text{canny}}[x, y_0 + k] > 0\}$
3. Check if there is a candidate within the range:
   (a) if $|v - v_{\text{next}}| < r$, set $E[y_0 + k] = v_{\text{next}}$, $y_0 = y_0 + k$, and $k = 1$, continue from (1)
   (b) otherwise, increase k, and continue from (1).

Any locations where an appropriate edge value cannot be found are set to `NaN`, so that they can be easily identified or ignored. A detailed implementation is shown in listing 4.1.

```
def shrink(edge, region, edge_image, c=3):
    """ Interpolate within a region based on the canny-extraction."""
    st, end = region
    # Start with an edge value in the above good region
    value = edge[st-1]
    k = 0   # ‘k‘ counts how many missing pixels there are (y_2 - y_1)
    for i in range(st, end):
        # ‘r‘ is the valid distance for the next value
```

```
        k += 1
        r = int(np.floor(k**.5 * c))
        # Find the next candidate value
        candidates = edge_img[i, :]
        nextv = sorted(np.flatnonzero(candidates) - v,
                       key=lambda x: np.abs(x))
        if not nextv:
            # There is no candidate
            edge[i] = np.nan
        elif np.abs(nextv[0]) < r:
            # The best candidate satisfies the condition
            v += nextv[0]
            edge[i] = v
            k = 0
            r = c
        else:
            # The best candidate is outside the range
            edge[i] = np.nan
```

Listing 4.1: In-painting function

4.2 Global morphology

In order to characterize the global morphology of icicles, two quantities were considered: the radial growth rate, and the elongation. The observations of the global morphology are reported in Chapter 5.2. We focus on the rates of elongation and radial growth, to simplify comparisons between icicles grown for different lengths of time under different conditions. For most icicles, the growth rates are constant and closely relate to the length and radius at a fixed time into growth, but the growth rates incorporate all of the data from start to finish. Calculating the growth rate through regression also reveals when the icicle growth rates are not constant.

The elongation rate is found through a straight-forward linear regression, but the radial growth rate measurement is much more involved. For the radius measurement, we are not concerned about the rippled topography, so the ripples on each edge are filtered out using a discrete cosine transform. All wavelengths shorter than 25 mm are removed, leaving the smooth edge.

The radius is calculated as $R[y,t] = (E_r[y,t] - E_l[y,t])/2$, where E_r and E_l are the right and left edges respectively. Thus the radius is a function of y measured from the top of the icicle.

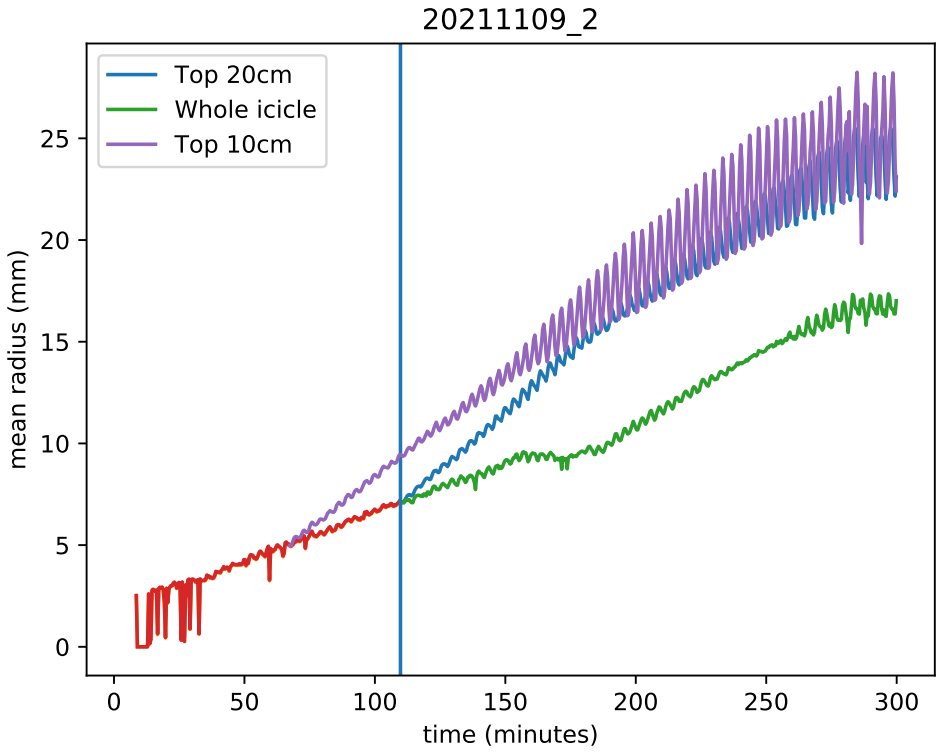

Figure 4.2: The mean icicle radius vs time for an icicle. When radius is averaged over the entire length of the icicle, the mean radius grows substantially slower than at any one point. A more accurate radial growth rate can be found by restricting the region of interest to the top 10 cm or 20 cm. The vertical lines indicate when the icicle edge fills the region of interest, and the mean radial growth rate more closely matches the local radial growth at any point in the region. Axial asymmetries cause fluctuations in the icicle radius as it rotates.

Because the icicle is growing in length, the tip always has the same small radius. If the mean radius of the whole icicle, $\frac{1}{N(t)} \sum_y R[y,t]$, is used to calculate radial growth rate, then the measured radial growth rate would be lower than the actual radial growth at any point along its length. This behaviour can be seen in Figure 4.2. The radial growth rate measurements presented in Chapter 5.2.2 are calculated from the mean radius of the top 200 mm of the icicle. The rate is calculated for the time after the icicle reaches that length.

4.3 Ripple topography

In order to examine the rippled topography of icicles, we consider four values: ripple wavelength, ripple amplitude growth, maximum ripple amplitude, and ripple migration rate.

4.3.1 Ripple wavelength

Accurately and reliably measuring the wavelength of icicle ripples is difficult in such a large data set. Two previous methods were used. Maeno *et al.* [18] measured the wavelength by measuring the distance between adjacent ripple peaks on an icicle, then defined the wavelength as the average distance between adjacent peaks. Chen *et al.* [20, 12] used a Fourier transform method. The power spectrum was calculated of the top 10 cm of an icicle, then fit with a Lorentz function. The position and width of the fitted Lorentz function provides the wavelength and its uncertainty. These two methods should provide the same results on an ideal rippled edge, but real icicle edges are far from ideal.

Chen's method using the power-spectrum introduces a significant challenge, which obstructs automation of wavelength measurement. The power-spectrum of an edge will often have multiple peaks, as seen in Figure 4.3. Fitting a single peak to such a spectrum is extremely inaccurate, and the largest peak may not be the correct wavelength. Even within a single icicle, one frame may have multiple peaks in the spectrum, while the next frame has a single clear peak. For this reason, we decided to revert to Maeno‘s original method, which is simpler and more reliable. Measuring peak-to-peak distances also opens up further statistics, like the variance of wavelength within a single icicle.

Wavelength algorithm

The ripple wavelengths throughout this thesis were determined using a statistical approach, based on real-space position measurements of the peaks and valleys on edge detected topography. The average of the distance measurements gives a ripple wavelength consistent with previous measurements that were made using a Fourier technique [12]. This method allowed us to use data from a larger fraction of the icicle, as well as giving a better statistical understanding of the variability of the wavelength.

To obtain the ripple wavelength during growth, each icicle was imaged over 700 times, and both edges were extracted, as described in Section 7.1.1. The wavelength

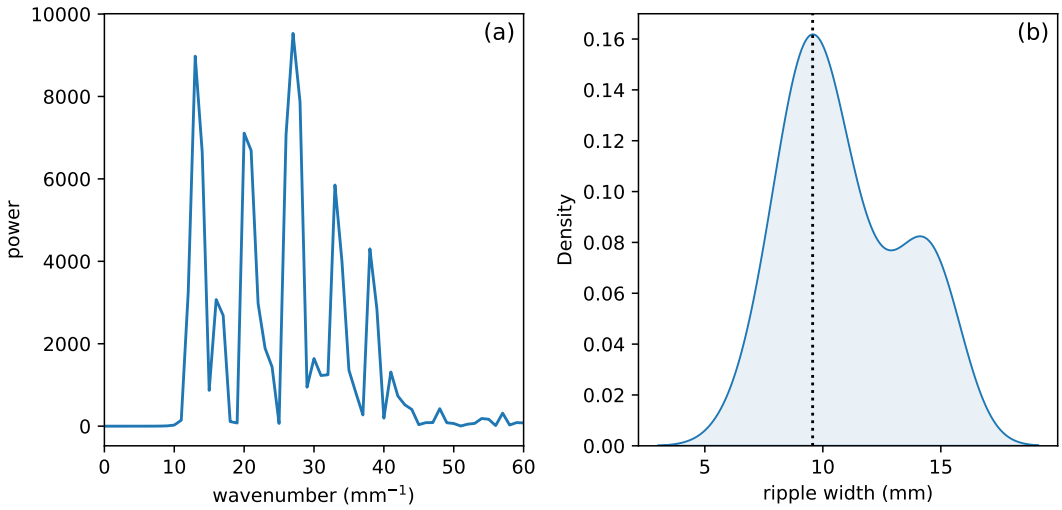

Figure 4.3: Frame 393 of icicle number 20211110_2 has multiple peaks in the power spectrum (a). There are 5 clear peaks at wavelengths 7.9, 9.1, 11.2, 14.8, and 23.4 mm. Examining the distribution of ripple-widths (b), there appears to be an additional small mode near 14 mm. It is possible that this additional mode interacts with the primary wavelength of 9.25 mm to create multiple peaks in the power-spectrum.

of each edge was measured independently using the following procedure. First, each edge was then detrended using a discrete cosine transform, removing all wavelengths longer than 5 cm. The positions of the peaks and valleys were then found using `scipy.signal.find_peaks()` [65] with minimum prominence of 3 px (approximately 0.2 mm). The "ripple widths" were calculated as the distance between adjacent peaks and valleys, and the *wavelength* of the edge was taken to be the *mode* of the ripple width distribution.

This procedure provides a wavelength at each point in time during growth. We found that the wavelength was constant throughout growth, so that the median value of all these wavelengths could be taken to be the ripple wavelength for each icicle during its growth. A typical progression of the ripple wavelength of an icicle is shown in Figure 4.4.

We limited the edge sampling to a time and region where ripples are well-formed; between 90 and 240 minutes into growth, and the top 20 cm of the icicle. Results of this analysis are presented in Section 5.3.1

The first step of detrending the icicle edge has a negligible effect on the peak (or valley) position, but makes the method more reliable, and ensures the *prominence* value used to measure the ripple amplitude in Section 4.3.2 is consistent with the

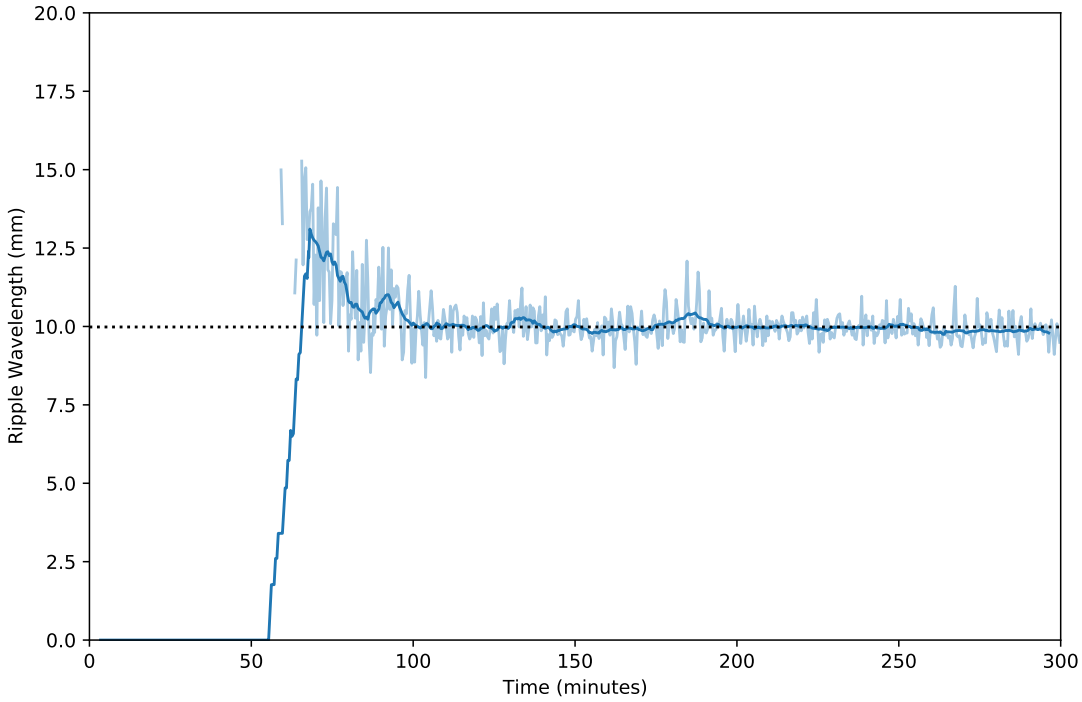

Figure 4.4: The measured wavelength during icicle growth. The dark line shows the rolling average of the wavelength. After ripples form, the wavelength is stable, so the median wavelength (horizontal dashed line) is used for the icicle's wavelength.

amplitude that would be measured with a Fourier transform.

We choose to calculate the wavelength independently for each edge, because the concept of "wavelength" does not make sense for multiple combined signals. This choice also reduces the effects of sampling bias: when all of the *widths* are combined into one distribution, there is a skew towards longer widths, because it is more likely to miss a ripple peak than find a peak where there is none. Missing a ripple peak will cause a long ripple width. This sampling bias is also the reason that we use the *mode* to calculate the wavelength. The *mode* is less affected by a skewed distribution than either the *median* or *mean*. Outliers were removed from the width distributions using an inter-quartile range (IQR) method. Any value outside of $median \pm 1.5 * IQR$ were identified as outliers, and ignored.

4.3.2 Ripple Amplitude

The function to extract the peaks from an icicle edge also returns the "prominence" of each peak. The returned prominence is the height of the peak above the background. In the case of a rippled edge, the background of a peak is the depth of its adjacent valleys, so the amplitude of a peak is one-half of the prominence. The ripple amplitude is calculated independently for each edge as the median of the peak and valley amplitudes.

We then use the calculated ripple amplitude as a function of time to find both the maximum ripple amplitude, and the ripple amplitude growth rate.

Amplitude growth rate

A naive approach to measuring the ripple amplitude growth rate would be to use the amplitude of an entire edge. However, that would suffer from the same problem as the radial growth rate (Section 4.2). The new ripples will always have lower amplitude than the older ripples, reducing the average ripple amplitude. We solve that problem in the same way as for the radial growth rate; the ripple amplitude is measured on a region between 5 cm and 15 cm from the top of an icicle. Measuring the amplitude of a longer segment can fail for lower concentrations, because the maximum amplitude can be reached before the icicle edge fills the region.

There is an additional complication for ripple amplitude, because there is a maximum amplitude that is reached. This maximum amplitude is dependent on feed-water concentration. In Figure 4.5, we see that the ripple amplitude grows linearly until it plateaus at a maximum value. If allowed to grow longer, the ripple amplitude will

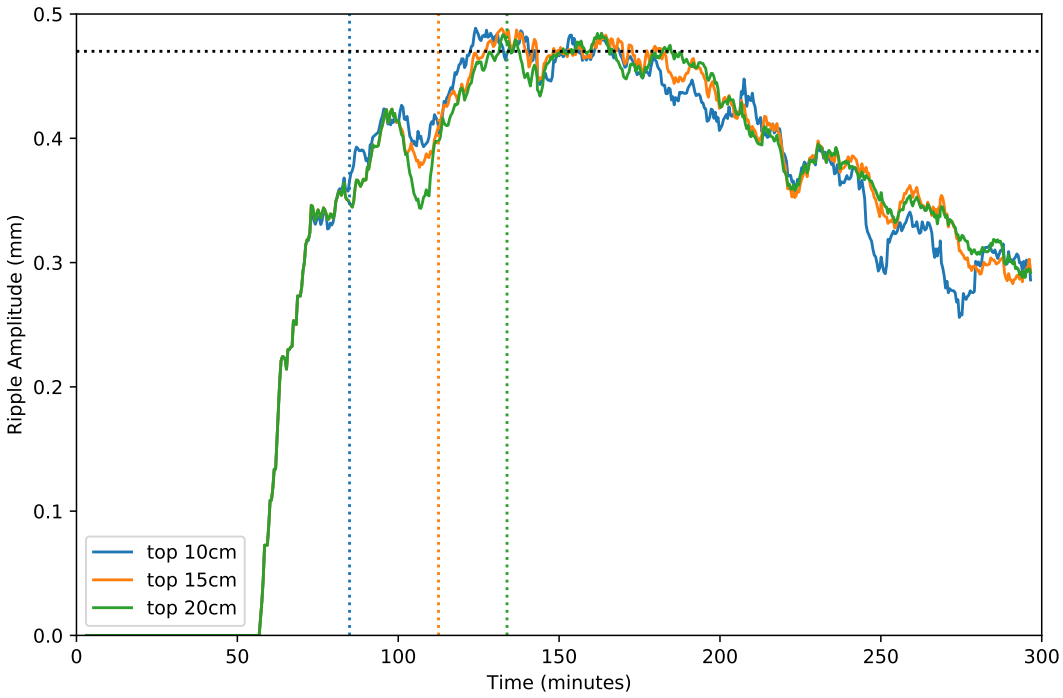

Figure 4.5: Ripple amplitude vs time of an icicle grown from 20 ppm NaCl feed-water. The vertical lines indicate when the icicle has grown to fill the measured region with corresponding colour.

gradually decrease. We examined similar plots for many icicles, and determined that the ripple amplitude consistently increases for at least 30 minutes after the ripple forms.

With that in mind, we calculate the ripple amplitude growth rate by fitting a line to the ripple amplitude of a 10 cm long region for 30 minutes after that region is formed.

Maximum ripple amplitude

The maximum ripple amplitude is simpler to find than the growth rate. However, we can see in Figure 4.5 that the ripple amplitude fluctuates wildly depending on orientation, and can also start decreasing as the icicle grows larger.

To calculate the maximum ripple amplitude, we first take a rolling average to reduce the fluctuations, then select the 95th percentile as the maximum, which ignores outliers. For the rolling average, a window width of $N = 16$ (1 rotation) was used. We tested percentiles from 90 to 99 on a subset of icicles, and found that they were consistent within the resolution of the images, because the ripple amplitude changes

slowly around its maximum.

4.3.3 Ripple migration

The ripples on icicles tend to migrate. Some treatments of the thin-film theory predict a downwards migration, but Chen and Morris [12] found that ripples consistently migrate upwards when the feed-water concentration was below 320 ppm NaCl. Above this concentration, the direction of migration is inconsistent, sometimes moving upwards, at other times downwards.

Because the ripple wavelength measurement is derived from distances between peaks and valleys, the locations of all peaks for each edge is extracted as a bi-product. Tracking the ripples throughout time was performed simply by selecting one peak from the list, and finding the closest peak at each subsequent rotation. However, this is still a manual process, because the selection must be done carefully. In particular, for low concentrations, ripples will quickly disappear, while for high concentrations, many ripples will split or merge.

A program was written in Python to assist in tracking the ripples. A space-time plot of all peaks was displayed, then the user clicked the peak to track, and the program tracked it through time. The trajectory of the peak was then plotted for verification, and the results were saved to a spreadsheet. Tracking the peak produces the position and radius at each point in time. The slope of the ripple peak ($\Delta R/\Delta x$) was used to find the angle of the peak's trajectory, for comparison with the chevron pattern seen in cross-sections.

Because tracking ripples is necessarily a manual process, it was only performed on a subset of icicles. The migration of rippled topography was compared to the angle of inclusions as reported in Chapter 7.

4.4 Fitting trends with concentration

The focus of our morphology experiments in Chapter 5 was the effect of concentration on the shape of icicles. As seen in the work by Chen and Morris [45, 20], most of the morphological properties vary with the logarithm of concentration. Normally, this would suggest a power-law relation, $X = Bc^A$, where A is the slope of the line on a semi-log plot. However, icicles grown from pure water still have a radius and length, which is not possible with a power-law relation. For that reason, we add a constant to the power-law $X = Bc^A + C$, that represents the nominal value if no impurities

are present. While there is no theoretical model to justify this relation, it provides a reasonable quantification of the trend.

4.5 Summary

A Python package was written to implement the above methods on our experimental data. The majority of the results are presented in Chapter 5, after being applied to the full set of icicles we grew in the icicle machine. This includes the radial growth and elongation rates, and the ripple wavelength and amplitude. The migration of ripples was compared to the pattern of inclusions in Chapter 7.

Additional methods were implemented to track the liquid on the surface of icicles. Those methods and their results are presented in Chapter 6.

Chapter 5

Morphology

In this chapter, we present our experimental findings of the effects of small amounts of impurities on the morphology of icicles. Previous experiments with icicles tend to either use distilled water [19, 40] or marine water [14, 17]. The largest experiment on the morphology of freshwater icicles with impurities was performed by Chen and Morris [12, 20, 45]. The experiment presented below extends the work of Chen and Morris using a larger set of icicles, and by considering different chemical species of impurities. We begin with a summary of previous experiments.

The earliest quantitative and systematic review of icicles was conducted by Maeno and Takahashi in 1984, in which they observed the growth mechanics of icicles [40] grown in a lab, and measured the ripples on a set of natural icicles collected in Sapporo. In 1988, Makkonen proposed a mathematical model to predict the elongation rate and radial growth rate of icicles by balancing water flux on the surface and heat transport to the atmosphere [11]. A joint paper by Maeno, Makkonen, *et al.* followed in 1994, comparing a set of 30 lab-grown icicles grown from distilled water to Makkonen's model [19].

An similar model for marine icicles, including the effect of salt on elongation and radial growth, was developed by Chung and Lozowski for marine icicles [14]. This model predicts a decrease in elongation rate for higher concentrations of impurities, but a larger radius at towards the root. Chung and Lozowski grew a set of 7 icicles using 33 ppt NaCl water to confirm the predictions of the model. Maeno, Makkonen, *et al.* found a consistent result for one of their icicles grown with a 32 ppt NaCl solution [19]. In his thesis, Chen observed the same behaviour for icicles with concentrations above 10 ppt NaCl, but counter-intuitively, the elongation rate increased with concentration up to 10 ppt NaCl [20].

Some time later, Short *et al.* [44] considered how a thermal boundary layer pro-

duced by natural air convection would affect heat transport, and thus the overall shape of an icicle. Short's model predicts a self-similar shape following a 4/3 power-law. Chen and Morris [45] grew a set of 76 icicles that were compared to Short's predicted icicle shape, and found good agreement for icicles grown with distilled water.

Meanwhile, Ogawa *et al.* [25], and Ueno *et al.* [26, 27, 28, 29, 30, 31, 32] produced a series of papers focused on a thin-film model of the rippling instability as discussed in Chapter 2. The ripple wavelength had been measured by Hatakeyama and Nemoto [36], Maeno *et al.* [18], both finding an average wavelength of 9.0 mm. Later, Chen and Morris established the dependence of icicle ripples on concentration [12] in a set of 67 laboratory icicles, varying wall temperature, flow rate, and concentration of NaCl. Remarkably, the ~ 9 mm wavelength was unaffected by any of those parameters.

In the following sections, we present a larger set of icicles than has been previously considered. The focus of this work is the effect of the concentration and chemical species of impurity on the morphology of icicles. Four aspects of the morphology of icicles were measured. The overall shape (global morphology) was characterized by the radial growth rate, and elongation rate. The rippled morphology was characterized by wavelength and maximum ripple amplitude. The observed effects of concentration on the morphology of icicles is consistent with Chen and Morris's observations [12]. We further find that the chemical species of impurity does not change the morphology, and so the rippled morphology of icicles is a colligative phenomenon.

The global morphology of icicles is measured in Section 5.2. It is established that higher feed-water concentrations increase both the elongation and radial growth rates. The radial growth was more strongly affected by impurities, so icicles grown with impurities tend to be broader than pure water icicles.

The rippled morphology of icicles is measured in Section 5.3. The presence of ripples is purely dependent on impurities in the source water. The quality that is most affected by concentration is the ripple amplitude, which follows a clear upward trend with concentration. However the wavelength of ripples remains completely unaffected by temperature, flow rate, concentration or chemical species. During icicle growth, the ripple amplitude rises to a maximum value, then slowly decreases in late stages of icicle growth. This behaviour is discussed in Section 5.3.2.

The chemical species of impurity showed no effect on any of the measured characteristics of icicle morphology. All dissolved solids exhibited similar morphological magnitudes and trends when the molar concentration was considered, rather than the mass concentration. The charge and molecular weight of dissolved solids had

no visible effect on the morphology. This strongly suggests that icicle ripples are a colligative phenomenon.

5.1 Water concentrations and growth conditions

A set of 128 icicles were grown using the icicle machine described in Chapter 3. With our focus being the role of impurities, approximately half ($N = 59$) of the icicles were grown with an air temperature of 14.0 ± 0.5°C and a flow rate of 3.0 ± 0.1 g/min. The rest of the icicles were grown in temperatures between -17.6°C and -7.6°C, and with flow rates between 1.2 g/min and 3.2 g/min.

The chemical species used for the instability-triggering impurity were sodium chloride (NaCl), cupric sulfate ($CuSO_4$), ferrous sulfate ($FeSO_4$), sodium sulfate (Na_2SO_4), sodium fluorescein ($Na_2(C_{20}H_{12}O_5)$), D-Glucose, and 3350 molecular weight polyethylene glycol (PEG3350). The majority of icicles were grown with either NaCl (52 icicles) or fluorescein (49 icicles). Fluorescein has a relatively high molecular weight of 332.3 g/Mol and a charge of -2. In order to distinguish effects of charge and molecular weight, we grew a set of 17 icicles using Na_2SO_4. Sulfate has a charge of -2, and molecular weight 96.0 g/Mol. D-glucose and PEG3350 are both non-ionic impurities with molecular weights 180.2 g/Mol and 3350 g/Mol. The number of icicles grown with these chemicals was insufficient to observe trends independently, but they agreed with the trends seen in NaCl and sodium fluorescein.

5.2 Global morphology

The first aspect of icicle morphology considered is the overall shape, as described by radial growth rate and elongation rate. Dependence of these quantities on air temperature and flow rate has already been explored. Icicles grow faster in both length and radius in colder temperatures. The radial growth is largely unaffected by flow rate, but the elongation of an icicle slows for a higher flow rate [19, 20], because the pendent drop experiences less cooling before it falls of the tip.

In marine icicles, the elongation rate decreases while the radial growth increases near the root, producing icicles that are shorter and wider than pure-water icicles [14]. This change in morphology is a result of accumulation of impurities in the liquid descending the icicle, which lowers the freezing point down the length of the icicle. The prediction of that model is that marine icicles grow to be shorter and wider than freshwater icicles. This difference was more pronounced at colder temperatures. This

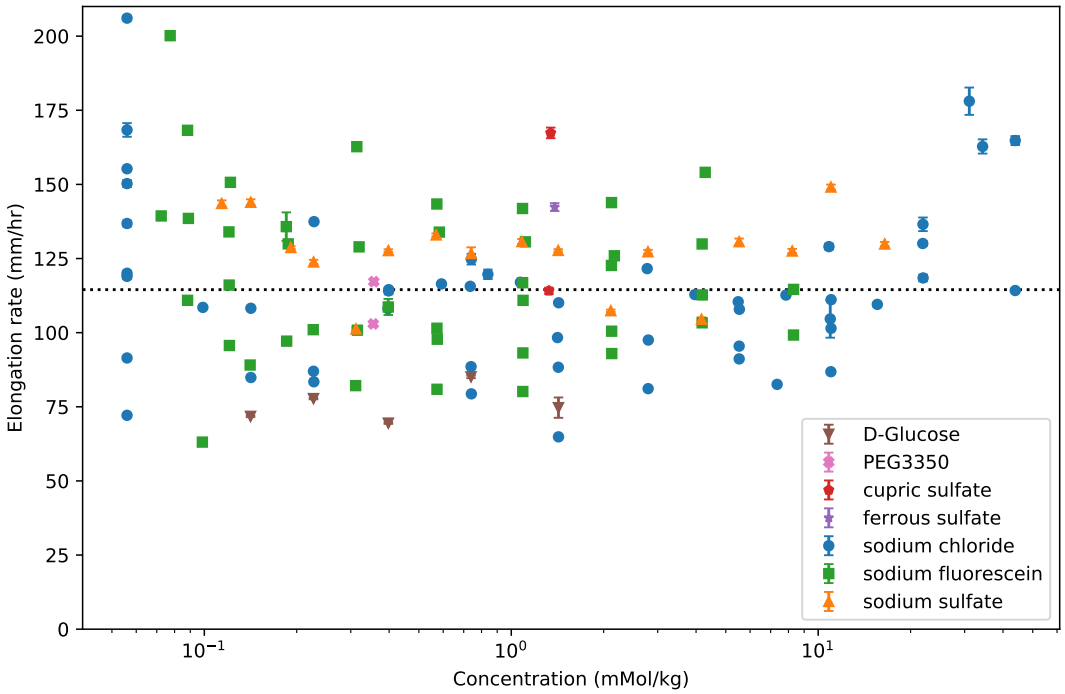

Figure 5.1: The elongation rate of all icicles. There appears to be no effect caused by concentration.

decrease in elongation rate was also observed in Chen's experiment for concentrations above 10 ppt NaCl, but below that, the opposite trend was observed [20].

Like Chen, we find that both the elongation rate and radial growth rate increase with concentration in this range of concentrations. The radial growth rate is more strongly affected by concentration than the elongation, so low-salinity icicles should be both wider and longer than pure water icicles under the same growing conditions.

These effects are seen regardless of the chemical species used as the impurity. Provided the molar concentration is equal, icicles grown under the same conditions will have similar lengths and diameters.

5.2.1 Elongation rate

We measure the length as the vertical distance between the root and tip. In early stages of growth, icicles tend to lengthen at a constant rate, but in later stages of growth, the elongation may accelerate before cessation occurs. Figure 5.2 shows this behaviour in a series of icicles with varying concentration. In our set of icicles, this accelerating elongation is more common in icicles grown with higher concentrations

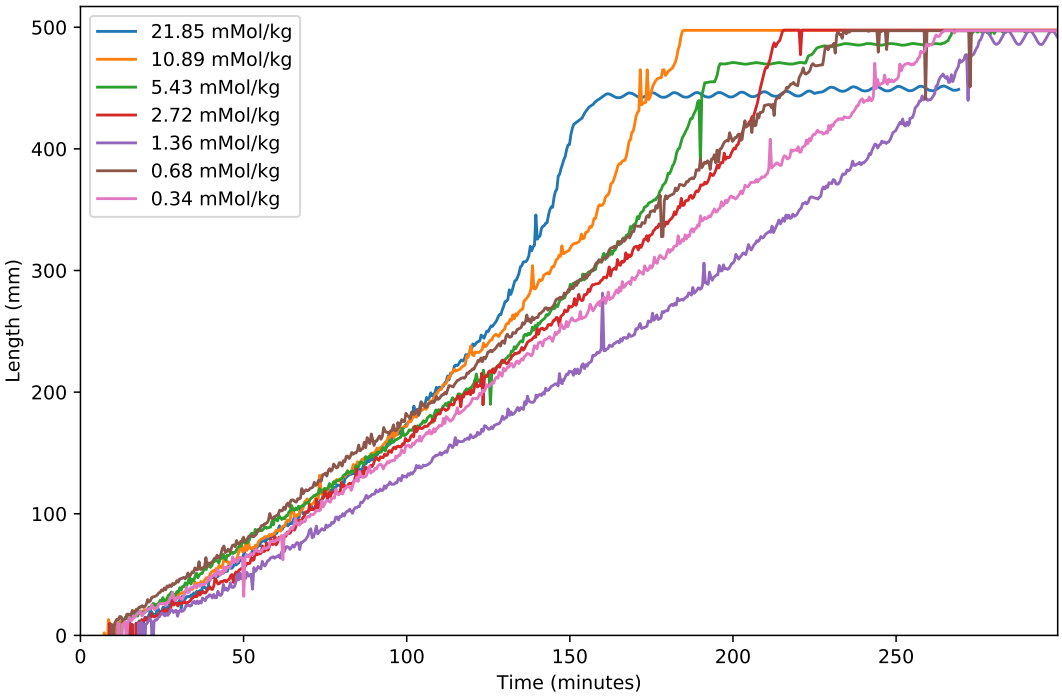

Figure 5.2: Length vs time for a series of icicles. Icicles with higher concentration tend to accelerate in length in later stages of growth.

of impurities. Chung observed the opposite elongation behaviour in marine icicles: the elongation decelerates as it approaches cessation.

The rate of elongation for icicles was calculated from the length using a linear regression against time. For consistency between icicles, we measure the elongation rate in the earlier more linear regime, from the time it reaches 2 cm in length until reaching 22 cm.

If temperature and flow rate are not controlled, the icicles' elongation rate does not have a clear dependence on feed-water concentration, as seen in Figure 5.1. However, it is known from past experiments and theory [19, 20] that both the flow rate and temperature have a significant effect on the elongation rate, so these are confounding variables that may hide any trends in concentration. After controlling for both the flow rate and temperature, a trend in concentration will emerge.

First, we consider the dependence on temperature by limiting the dataset to a flow rate of 3 ± 0.1 g/min (N=100). The elongation rate is seen to decrease at higher temperatures in Figure 5.3. This matches what was seen in past work [19, 20], but there is significant variation in the plot. This variation in elongation rate is most apparent around $T = -14°\text{C}$, where the greatest variation in concentrations is

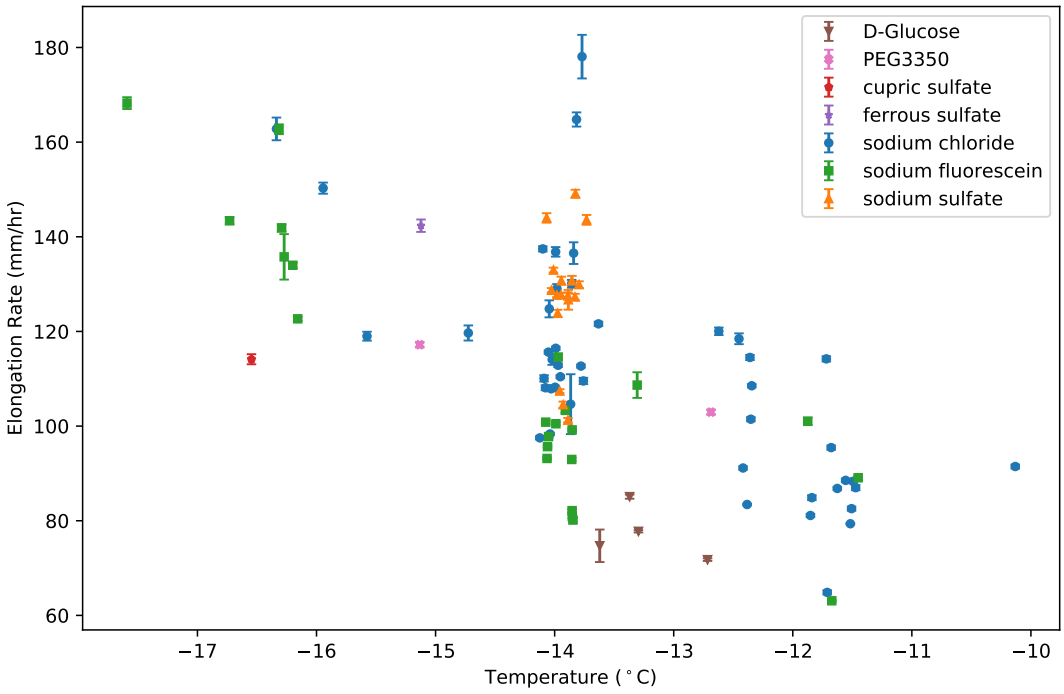

Figure 5.3: The elongation rate as a function of temperature, with a fixed flow rate of 3 ± 0.1 g/min. The elongation rate is dependent on temperature with a Pearson correlation coefficient $R = -0.60$.

present.

Next, if the dataset is fixed with $T_{\text{air}} = -14 \pm 0.5°\text{C}$ (N=77), there is also a downward trend in elongation rate with flow rate. This is shown in Figure 5.4. The dependence on flow rate also matches previous results [19, 45]. In our dataset, we see significant variation at a flow rate of 3 g/min, where the concentration is varied more significantly.

The high variation in elongation rate seen around the point ($T = -14°\text{C}$, $Q = 3$ g/min) indicates that another variable is affecting the elongation rate. This would be the concentration. To get a better view of the effect of concentration on icicle length, we restrict the dataset to icicles with a flow rate of 3 g/min and $T_{\text{air}} = -14 \pm 0.5°\text{C}$ (N=59). The elongation rate as related to concentration is shown in Figure 5.5. When both the temperature and flow rate are controlled, the trend in concentration emerges. We see that the elongation rate increases with concentration for both NaCl and Fluorescein. The small set of sodium sulfate does not show the same trend. When the elongation rate is compared to the logarithm of concentration, the Pearson correlation coefficients are, $R = 0.31$ for the whole set, $R = 0.37$ for NaCl, $R = 0.64$

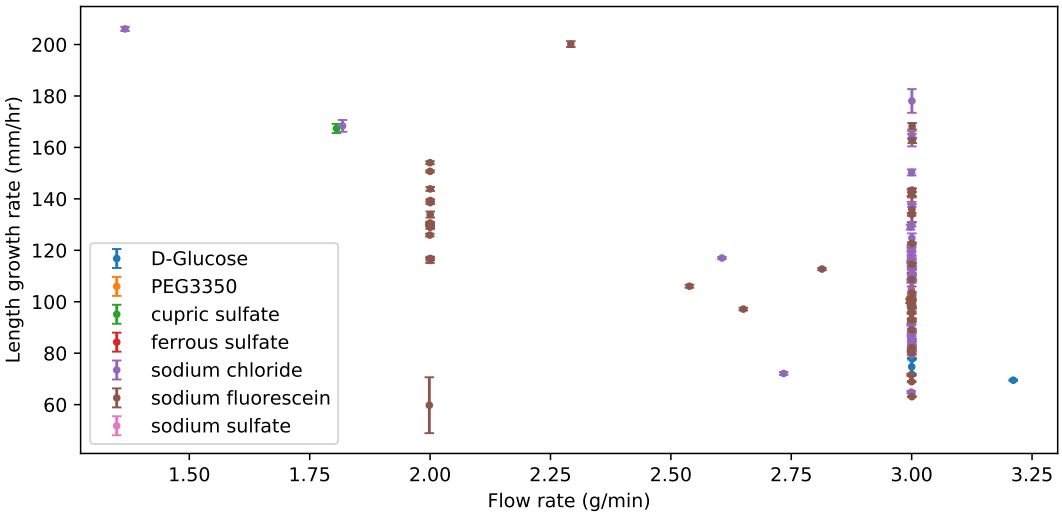

Figure 5.4: The elongation rate as a function of flow rate, with temperature fixed at -14 ± 0.5°C. The elongation rate depends on flow rate with a Pearson correlation coefficient $R = -0.34$.

for sodium fluorescein, and -0.06 for $NaSO_4$.

5.2.2 Radial growth

The radial growth rate has a clear trend with concentration as seen in Figure 5.6. It is remarkable that this trend emerges even without compensating for the effects of temperature and flow rate. Chen saw a similar trend in his experiments, with some evidence that it is strengthened at lower temperatures [20].

We begin a more detailed examination of radial growth by controlling for temperature. Past experiments showed an increase in radial growth with temperature, but no clear effect from varying water flow rate. In the experiment performed by Maeno *et al.* [19], the water flow rate had no apparent effect on radial growth rate, while the experiments by Chen and Morris [20] showed a slight effect with a maximum reached at 2 g/min. However, no previous study connected the radial growth with concentration.

Understanding that the air temperature has a significant effect on icicle growth, it makes sense to control that variable, as for the elongation rate in Section 5.2.1. Figure 5.7 shows the radial growth rate for the subset of icicles grown with $T_{\text{air}} = -14 \pm 0.5$°C. The full range of flow rates was included, because it has no significant effect on radial growth. The radial growth rates are much more consistent at a given

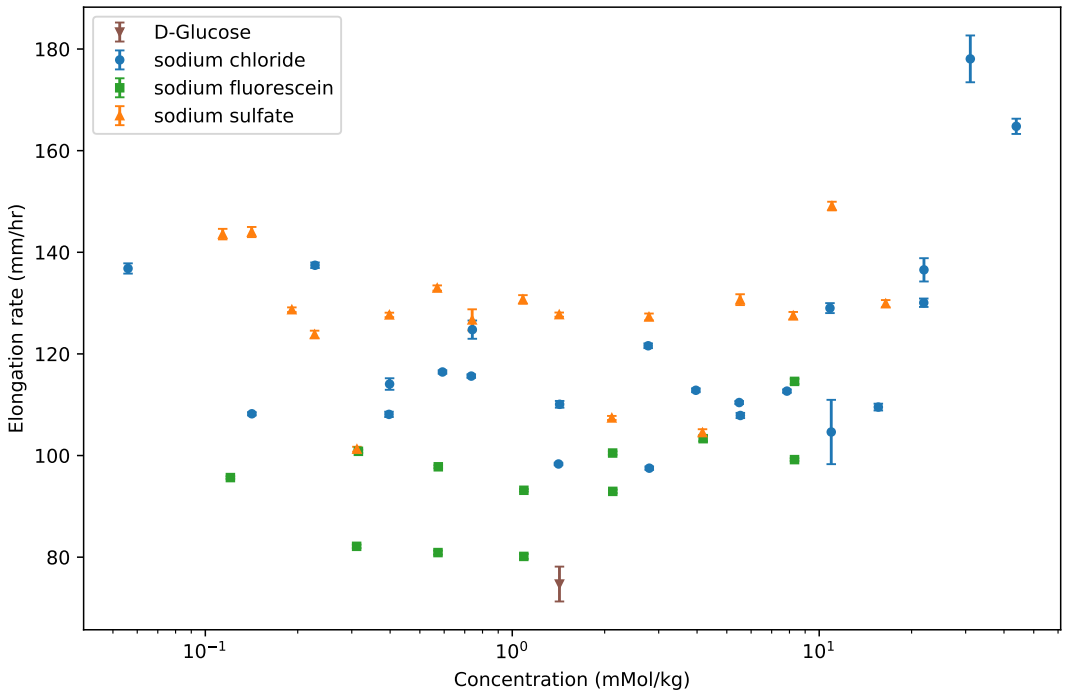

Figure 5.5: The elongation rate of icicles as a function of concentration with flow rate 3 g/min and $T_{\text{air}} = -14 \pm 0.5°\text{C}$. (Pearson correlation R=0.53 total, 0.72 NaCl, 0.59 fluoro, 0.17 $NaSO_4$)

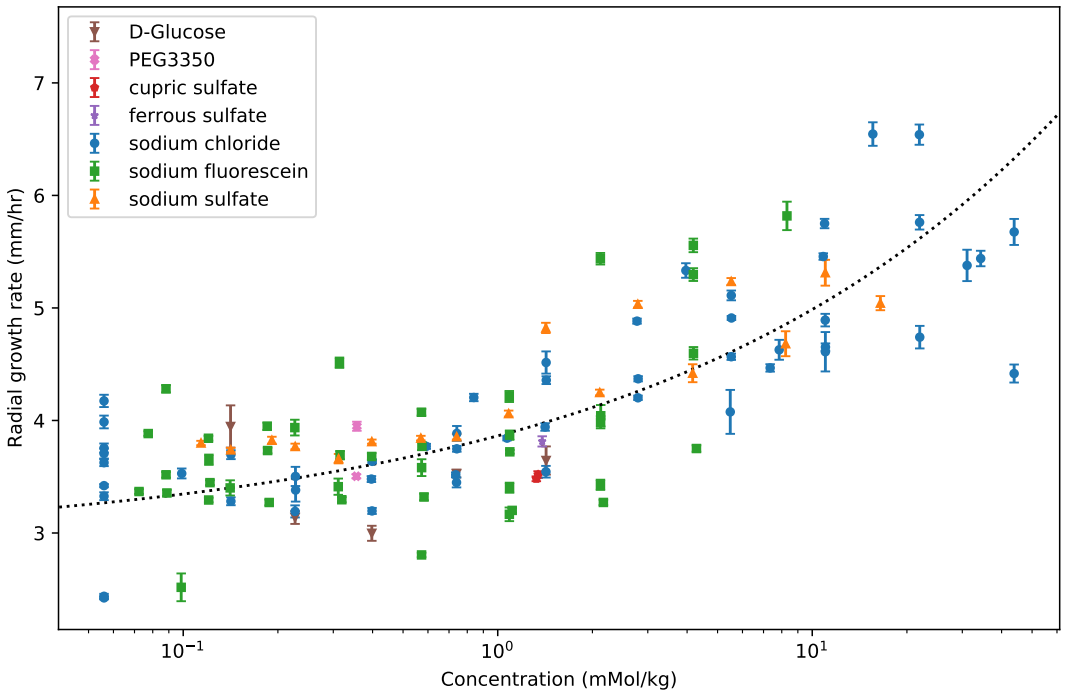

Figure 5.6: Radial growth rate of all icicles. There is a clear trend to higher radial growth for icicle grown from liquid with higher concentrations, but there is high variability due to variation in air temperature. The black dotted curve is the fitted trend, $\dot{R} = 0.91c^{0.34} + 2.94$.

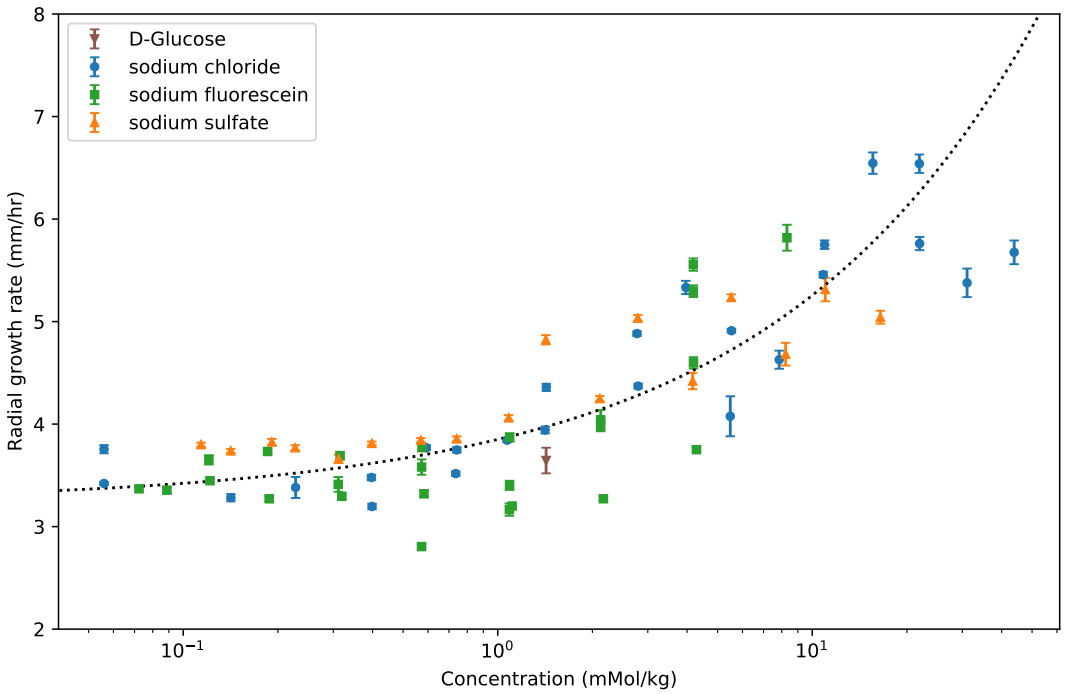

Figure 5.7: Radial growth rate of icicles with fixed air temperature $T_{\text{air}} = -14 \pm 0.5°\text{C}$. The black dotted curve is the fitted trend $\dot{R} = 0.63c^{0.51} + 3.2$. All of the icicles follow this trend, regardless of chemical species.

concentration, and follow the trend, $\dot{R} = 0.63c^{0.51} + 3.2$.

These results show that the radial growth of icicles has a high sensitivity to the concentration of impurities in the source water. Previously, this range of concentrations had only been considered by Chen [20], and our results further support his observation. The species of impurity does not significantly alter the radial growth rates.

5.2.3 Radial growth to elongation ratio

In the above sections, we have seen that small amounts of impurities increase both the radial growth and elongation of icicles. The radial growth rate has a greater dependence on concentration than the radial growth rate. The combined effects should produce wider icicles when the concentration of impurities is higher.

The overall shape of an icicle can be characterized by its aspect ratio. Fixing the flow rate and air temperature as in Section 5.2.1, we do see a change in the ratio of elongation and radial growth rates. The increase in radial growth out-paces the

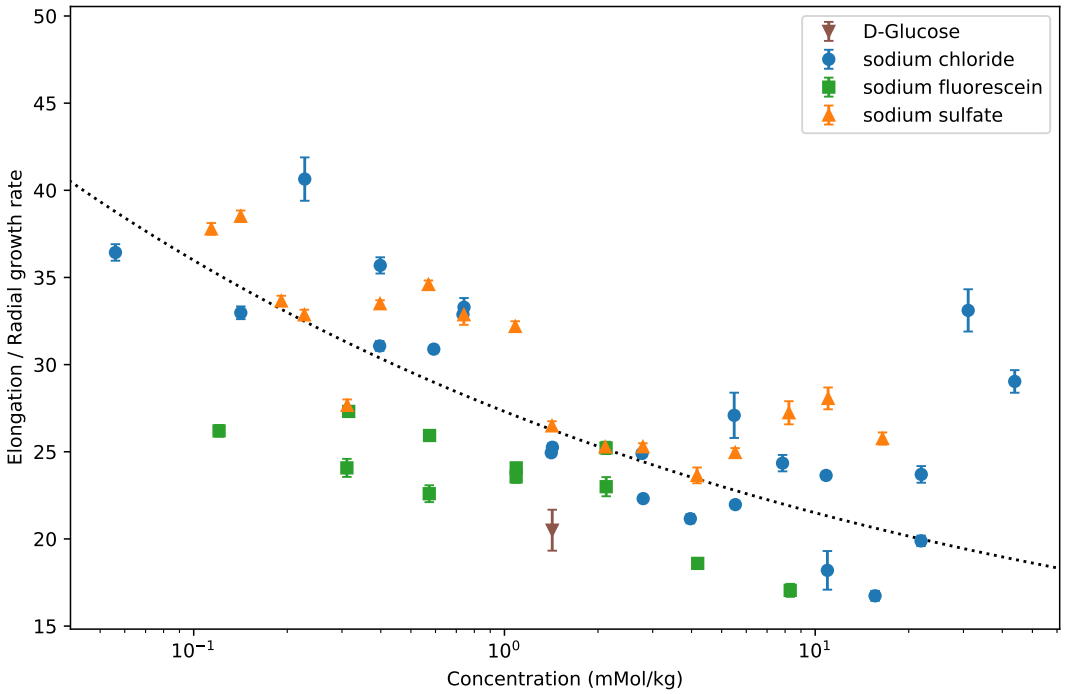

Figure 5.8: Ratio of elongation and radial growth rates for icicles with flow rate 3 ± 0.1 g/min and $T_{\text{air}} = -14 \pm 0.5$°C. At higher concentrations, the icicles tend to grow wider relative to their length.

increased elongation rate at higher concentrations, as seen in Figure 5.8. Thus rippled icicles grown with higher concentrations are relatively wider than those grown with distilled water.

5.3 Rippled Morphology

The first measurement of the rippled pattern on icicles was the wavelength [36, 18]. These measurements were made on natural icicles, and found that there was very little variation, with an average wavelength of 9.0 mm. The first systematic experiment on ripple formation on icicles under controlled conditions was performed by Chen and Morris [12]. This remains the most comprehensive study to date.

Chen and Morris established that the rippled morphology is only affected by the amount of dissolved solids in the source water [12]. The wavelength remained constant, regardless of growth conditions or concentration. The amplitude growth rate saw the largest change, increasing logarithmically with concentration. During icicle growth, the peaks of ripples were also observed to migrate. Below 320 ppm NaCl,

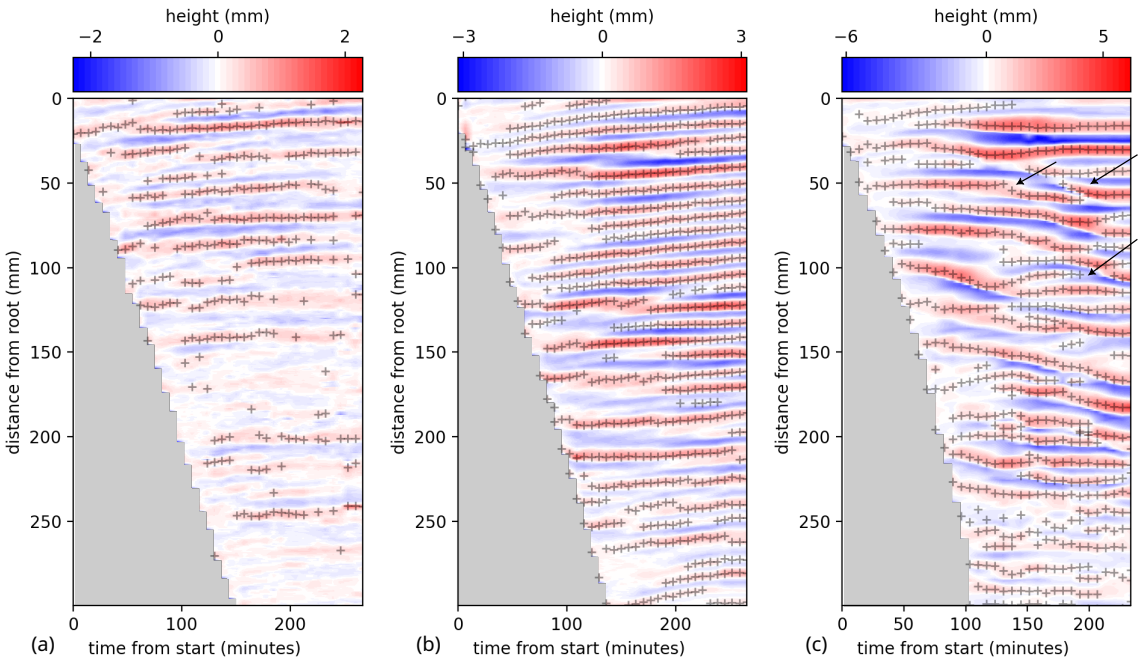

Figure 5.9: The extracted topography of icicles with concentrations (a) 0.34 mMol/kg (10 ppm NaCl), (b) 2.7 mMol/kg (80 ppm NaCl), (c) 22 mMol/kg (640 ppm NaCl). The peaks of ripples are marked by + symbols. Note the different color scales. The arrows in part (c) indicate ripple splitting or stopping events.

they consistently move upwards at a rate of 1.5-3.5 mm/hr. Above 320 ppm NaCl, the direction of migration becomes unpredictable [12].

We built upon the experiments of Chen and Morris by growing more icicles, and by using more chemical species to trigger the rippling instability. The rippled morphology was analysed using the techniques described in Chapter 4. The icicles were detrended using a high-pass discrete cosine so that only the rippled topography remained. The peaks and valleys of ripples were then found, and used in our measurements. Several examples of the mapped topography and the extracted peaks are shown in Figure 5.9

The chemical species of impurity did not affect the wavelength or amplitude of ripples, and our measurements are consistent with previous observations. The ripple wavelength measurements are presented in Section 5.3.1, and the amplitude in Section 5.3.2. Our observations of the ripple migration matched the behaviour observed by Chen and Morris [12], but we did observe a deep connection to the patterns of inclusions inside of icicles. For that reason, our discussion on the migration of ripples is deferred to Chapter 7.2.5, in the context of inclusions of impurities.

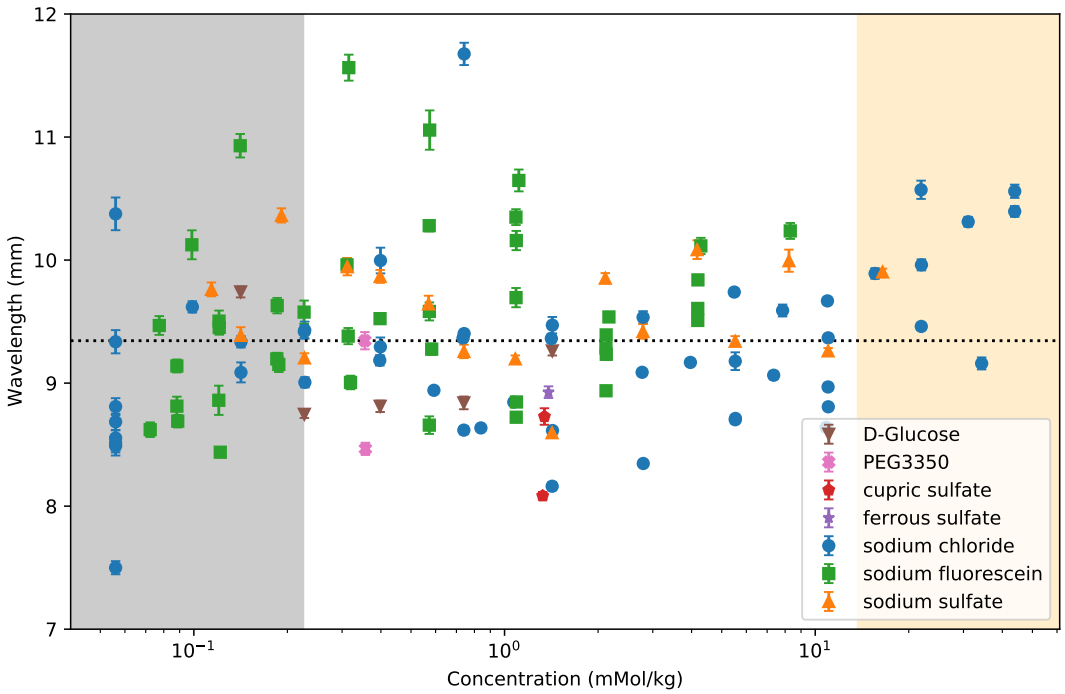

Figure 5.10: Wavelength vs concentration for all icicles. The wavelength is quite consistent below 10cm for most icicles with a median wavelength of 9.3 mm across all icicles. The grey region on the left indicates poorly formed ripples, and the orange region on the right indicates the concentration where ripple migration is unpredictable.

5.3.1 Ripple wavelength

It has been previously observed that the ripple wavelength does not depend on concentration [12, 19, 20]. The reason for this remarkable consistency is not known. In addition to varying concentration, we also investigated other species of dissolved solids as impurities. The set of icicles presented here includes more species of impurities than was previously studied. This includes a range of charges from D-Glucose and PEG3350 with zero charge to $FeSO_4$ and $CuSO_4$ with doubly charged ions. There is also a range of molecular weights, which affects the diffusivity. Even with the use of different chemical species, the ripple wavelength is consistent at 9.3 mm. The measured wavelengths are plotted against concentration in Figure 5.10 . The wavelengths of our full set of icicles is entirely consistent with the values measured by Maeno *et al.* [19], and Chen *et al.* [12]. The results are summarized in Table 5.1

For more clarity on the role of species on wavelength, the distributions of measured wavelengths for each species is shown in Figure 5.11. From this, it is clear that the type of impurity has little to no effect on ripple wavelength, because all distributions

Table 5.1: Summary of wavelength measurements for all icicles analyzed, including both data from edge detection and from annotated cross sections in Chapter 7. Measurements from cross sections are more reliable at intermediate concentrations, where the bands are well behaved.

	Dataset of icicles	Number	Average (mm)	Standard dev. (mm)	70% range (mm)
Edges	(all)	128	9.33	0.72	8.69 - 10.0
Sections:	(all)	30	8.30	0.68	7.78 - 9.06
	(well behaved)	25	8.54	0.66	7.8 - 9.3
	Maeno *et al.* [19]	19	9.0		7.0 - 10.0
	Chen *et al.* [12]	67	10.4	0.8	

of wavelengths fall within the same range.

For every impurity tested, the median wavelength fell between 8.4 mm and 9.6 mm, with standard deviations between 0.5 and 0.7 mm. The longest median wavelength observed was 9.6 mm seen in sodium sulfate, Na_2SO_4, followed by 9.4 mm for sodium fluorescein. These are both salts with two +1 cations, and one -2 anion. However, both distributions fall entirely within the values seen for NaCl which has a median wavelength of 9.2 mm with standard deviation 0.6 mm. As noted in Section 4.3.1, errors in the wavelength measurement are biased towards longer wavelengths. The longer tails of the sodium chloride and sodium fluorescein are explained by that systematic error.

5.3.2 Ripple amplitude

The clearest effect of impurities on icicles is the maximum ripple amplitude shown in Figure 5.12. The increase in ripple amplitude is obvious, and appears to have a similar power-law trend as seen in the radial growth rate, discussed in Section 5.2.2. Fitting a power law to our NaCl dataset of icicles, we find that $A_{\max} \approx 0.42c^{0.28}+0.15$. And the full set of icicles has the trend, $A_{\max} \approx 0.30c^{0.35} + 0.23$.

At first glance, it is counter-intuitive that there is a "ripple amplitude" even for icicles grown from distilled water, which would be described as "smooth". This is a systematic error due to the measurement method of ripple amplitude. Most significantly, there is a minimum amplitude that can be measured using the extracted edge from images due to the resolution – approximately 0.3 mm. This means that we are essentially fitting the noise in the grey region on the left of Figure 5.12

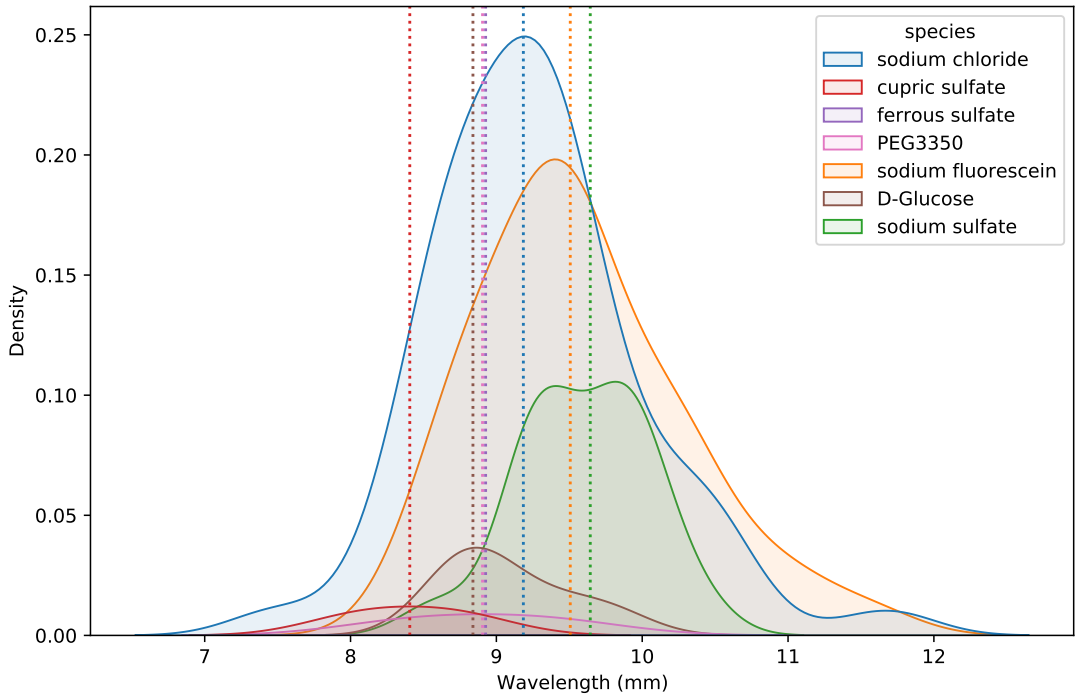

Figure 5.11: Distributions of the wavelengths organized by impurity species.

Another source of this error is that bumps on the surface that are not ripples are identified. These are either isolated bumps (e.g. from sessile drops) or small surface variations on the edge that do not form bands that surround the icicle. The latter effect belies a difficulty in terminology. Maeno *et al.* [18, 19] described "ribs" on icicles, while Chen and Morris [12] focus on "ripples", as do Ueno [27, 28, 29, 30, 31, 26, 32], Ogawa [25], and others in their thin-film models for ripple growth. Ripples on an isolated edge of an icicle may be present, but if the isolated edge is not correlated to its neighbours, this does not appear to be "ribs". Such isolated rippling does not visually correspond to "ripples" observed on an icicle surface.

There is no measurable difference in ripple amplitude when we limit the set to icicles grown with a flow rate of 3 ± 0.1 g/min, and air temperature $T_{\text{air}} = -14\pm0.5°\text{C}$. The maximum ripple amplitude for those icicles is shown in Figure 5.13. This agrees with the observation by Chen and Morris that the growing conditions do not affect the rippled morphology [12].

There is also no clear difference in the ripple amplitude for icicles grown with different chemical species. Sodium sulfate icicles follow the same trend as the sodium chloride icicles. There may be relative increase in amplitude for fluorescein at or above 4.2 mMol/kg (518 ppm Sodium Fluorescein, equivalent to 120 ppm NaCl), but there

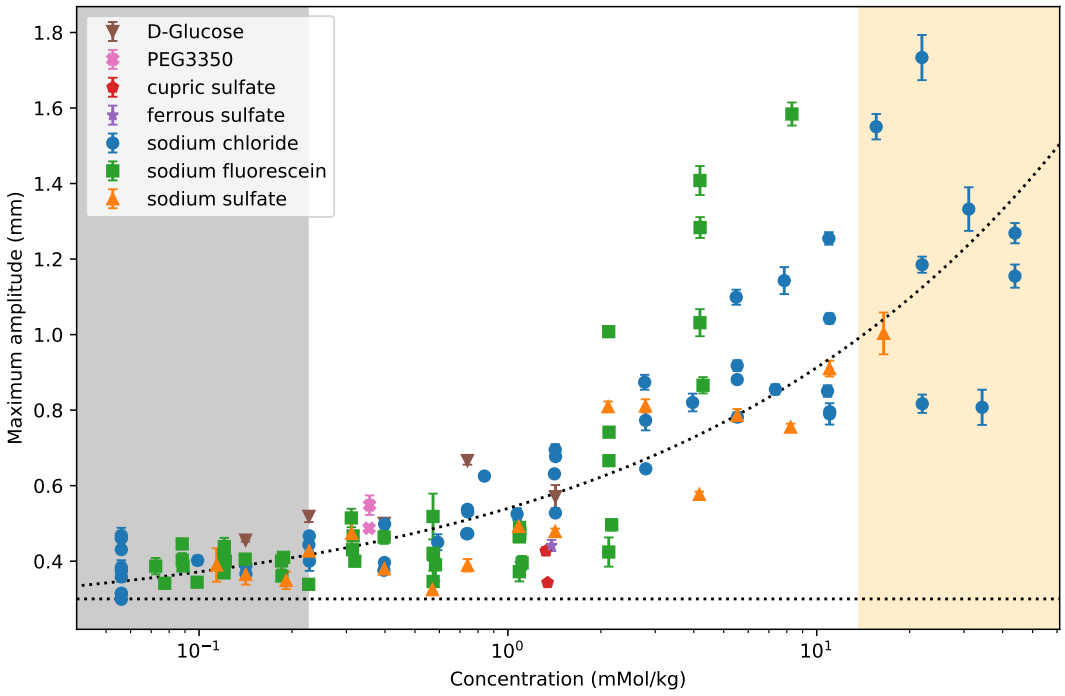

Figure 5.12: The maximum ripple amplitude reached for all icicles. The horizontal line indicates the minimum amplitude that can be resolved using the edge data. The grey region on the left indicates poorly formed ripples, where the algorithm essentially fits the noise on the surface. The curve shows a power-law fit to the NaCl icicles, $A_{\max} \approx 0.30c^{0.35} + 0.23$.

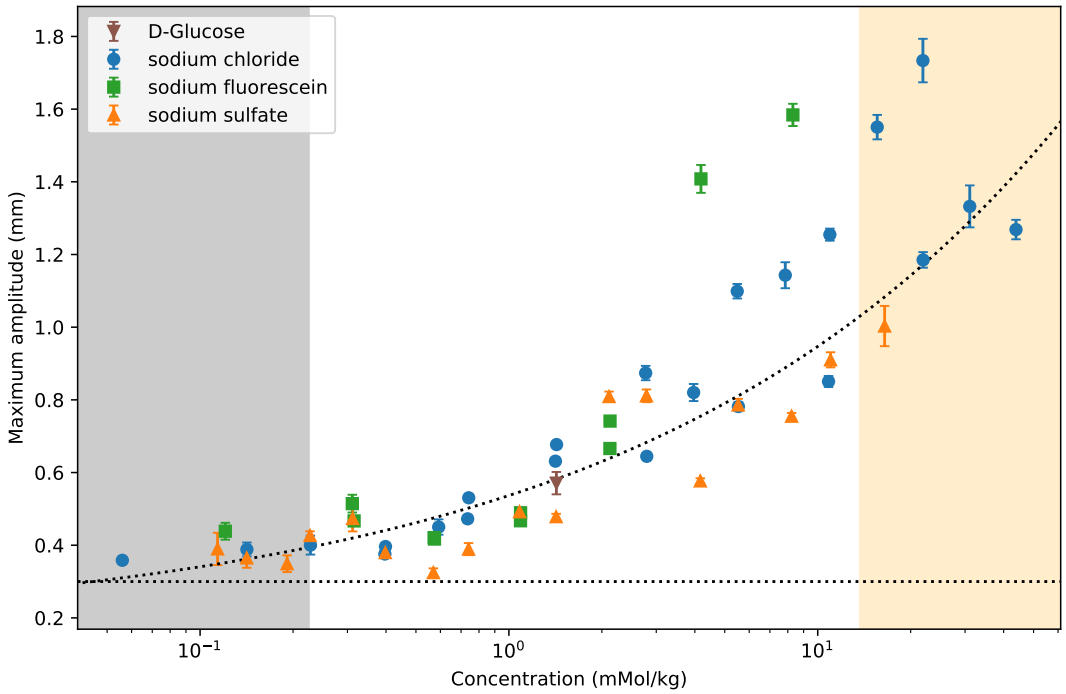

Figure 5.13: The maximum ripple amplitude reached for icicles grown with flow rate 3 ± 0.1 g/min and $T_{\text{air}} = -14 \pm 0.5$°C. The horizontal line indicates the minimum amplitude that can be resolved using the edge data. The grey region on the left indicates poorly formed ripples, where the algorithm essentially fits the noise on the surface. The curve shows a power-law fit to the NaCl icicles, $A_{\max} \approx 0.33c^{0.35} + 0.20$.

are not enough samples above that concentration to make a definitive statement.

5.4 Summary

Wet ice accretion from water with concentrations below 34 mMol/kg (10 ppt NaCl) has different behaviour than either marine ice or pure ice. In particular, the elongation and radial growth rates both increase with concentration in this range. The radial growth rate has a stronger dependence on concentration, so icicles in this range still have larger diameters for a given length compared to pure water, but they are longer than marine icicles. This is shown through the ratio of radial growth to elongation rate in Section 5.2.3.

The increase in radial growth rate with concentration could be a result of the increased retention of surface liquid seen in Chapter 6. With more liquid resting on the surface for a longer time, there is a greater opportunity for release of latent heat,

which in turn increases the freezing rate. This is would have the same effect as a reduced mass flux in the Makkonen model [11]. The reduction of mass flux at the tip of the icicle causes a similar increase in elongation rate, however the higher concentration counteracts this effect by lowering the freezing point. The competition between reduced mass flux and increased concentration may explain the relative insensitivity of elongation rate to concentration in this set of icicles.

We also observed an acceleration of elongation in latter stages of growth, with a more pronounced acceleration at higher concentrations. Because the elongation rate increases with concentration in this range, the accumulation of impurities down the length of the icicle might be the cause of this acceleration.

The Chung/Lozowski model for saline icicles always predicts a decrease in elongation rate with increasing concentration, because it depends on the accumulation of salt down the length of an icicle. This also has the effect of slowing the elongation in later stages of growth. Thus Chen's observations of elongation rate [20], and those presented here behave opposite of Chung's model for low-salinity icicles. Another mechanism is likely involved for low-salinity icicles. The difference may be a result of the surface water retention that we observe in Chapter 6.

Our observations of the rippled morphology are consistent with Chen and Morris's previous experiment [12]. The average wavelength is 9.3 mm with a standard deviation of 0.5 mm. The relatively low variance indicates that none of the temperature, flow-rate, or concentration affect the ripple wavelength. The ripple amplitude is also seen to increase with concentration, and shows negligible dependence on either temperature or flow rate.

Through the use of different chemical species for the impurity, we showed that the change to icicle morphology is a colligative property. Icicles grown with the same molar concentration exhibited similar morphologies. The chemical species of impurity has no substantial effect on either the global or rippled morphologies, regardless of charge or molecular mass.

Chapter 6

Surface liquid

This chapter presents work that has been published in New Journal of Physics [1] https://doi.org/10.1088/1367-2630/ac3cf4 . The experiments and data analysis were conducted entirely by John Ladan. Stephen W. Morris contributed to the discussion of our results as related to previous theories. An additional section about the liquid coverage near the tips of icicles was added as Section 6.3.3.

Models of icicle shape evolution, and of the origin of the ripple pattern, require a detailed understanding of how liquid water flows over a growing icicle. Here, we explore the flow dynamics using laboratory-grown icicles with a fluorescent dye as the instability-driving impurity.

Contrary to previous models, we find that the ice is incompletely wetted by the liquid phase, and that the whole process is much more stochastic than has been previously assumed. In addition, the presence of impurities modifies the wetting properties of the ice surface, while the emerging topography interacts with the liquid distribution. There is evidence for mixed-phase ice, which is observed in more detail in Chapter 7. These observations must inform any successful model of an impurity-driven rippling instability. Our results have general implications for the morphological evolution of many natural, gravity-driven, wet ice growth processes.

6.1 Introduction

The motivation of the present work is to explore the long time dynamics of the liquid water on the surface of growing icicles, with an eye to better understanding the mechanisms that lead to ripple formation.

We experimentally probed the dynamics of liquid water on the surface of icicles with the use of a strongly fluorescent dye added to the feed water. The dye acts as the impurity which triggers the ripple pattern, and an indicator for the liquid water. The composition of the feed water is described in Section 6.2 below. All icicles were grown in the icicle machine described in Chapter 3.

In Section 6.3, we observe that the liquid does not cover the entire ice surface, but rather descends in rivulets, leaving behind patches of liquid. What's more, in Section 6.3.1, we show that the amount of liquid retained on the surface is strongly correlated with the amount of impurities. In Section 6.3.2, we show that the distribution of liquid is also correlated with the upper surfaces of the ripples and matches their observed upward migration. We see that the tip of most icicles is always ensheathed in liquid in Section 6.3.3.

Our results shed important light on the unresolved question of why impurities are required for ripple formation. We show that icicles grown with impurities retain surface water quite differently than those without. To investigate processes that may affect the liquid distribution, we use cylinders of ice as a substrate and modify the surfaces to isolate single properties. Those results are presented in Section 6.4. In Section 6.5, we discuss the implications of these observations for theories of ripple formation.

6.2 The experiment

We grew a set of icicles using the icicle-machine described in Chapter 3. In addition to monitoring the growing icicle with the SLR, we also recorded 30 fps HD video during some runs, which allowed the fastest fluid mechanical time scales to be qualitatively observed.

Many different dissolved impurities can trigger the rippling instability. In this chapter, *sodium fluorescein* ($Na_2C_{20}H_{12}O_5$) was used as both a dye and the instability-triggering impurity. When icicles are grown with fluorescein dye and illuminated with white light, they fluoresce green in patches where liquid water is present while the ice appears orange. The effects can be seen in Figure 6.1. This fluorescent quenching is due to a saturation of fluorescein; as the liquid water freezes, the concentration of sodium fluorescein increases, and the fraction of fully dissociated fluorescein molecules decreases, quenching fluorescence and turning the dye orange.

The emissivity of fluorescein is dependent on its charge: the doubly charged di-anion emits strongly in the green band near 520 nm, while the singly charged anion

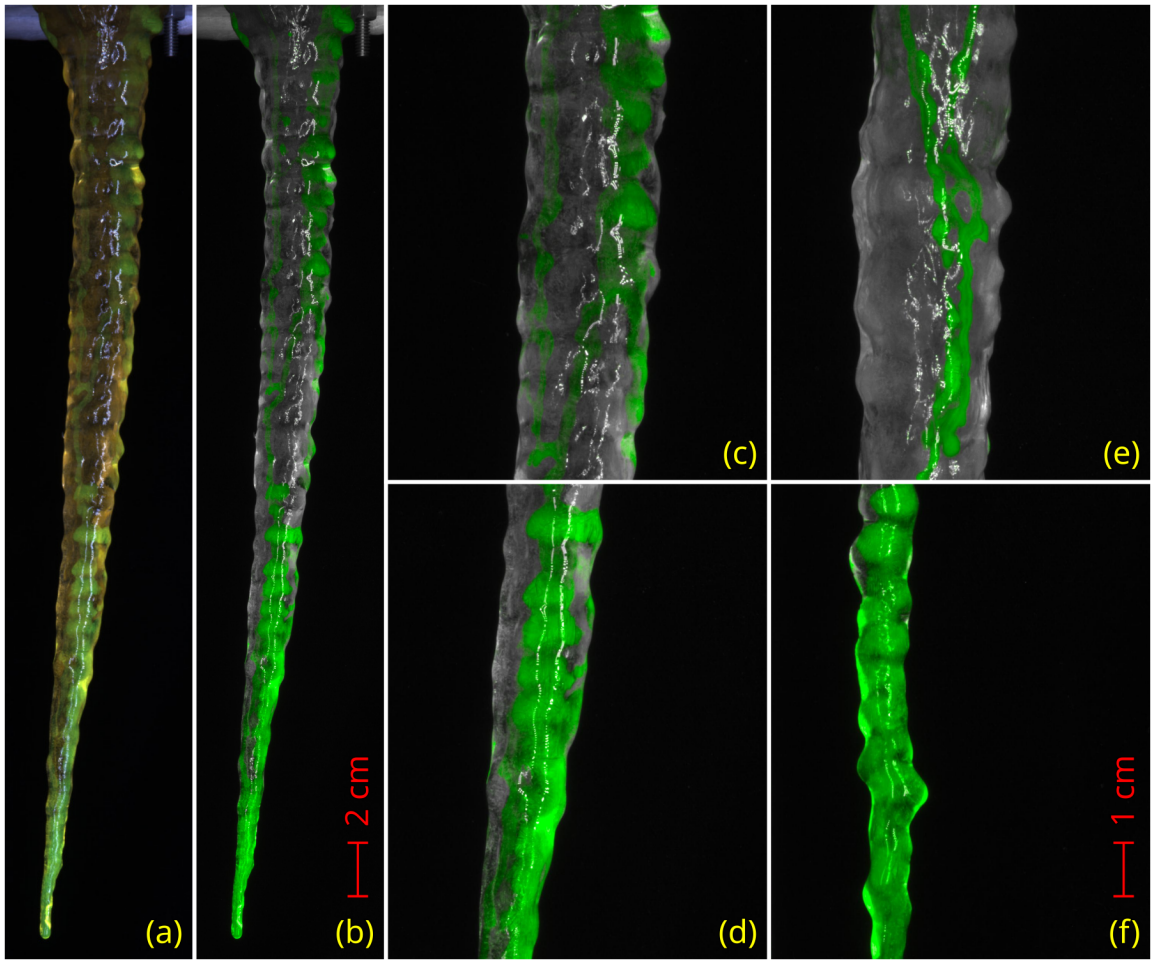

Figure 6.1: An example of an icicle dyed with 129 ppm sodium fluorescein. The quenched orange colour can be seen in the unaltered image (a), and the fluorescent green can be isolated (b) to locate liquid on the surface. Close-ups show patches of liquid on the upper side of ripples (c), (d). At a later time, thinner rivulets with complex branching are present (e), while the tip remains covered (f).

Table 6.1: Experimental parameters for the five series of icicles studied, comprising a total of 39 icicles. *The 32 ppm icicle for Series 1 had incomplete data due to a camera malfunction and has been omitted. †The NaCl solution in Series 5 was dyed with 8 ppm Sodium Fluorescein.

Series Number	Impurity	Initial Concentration (mMol/kg)	Number of icicles	flow rate (g/min)	air temperature (°C)
1	Sodium Fluorescein	4.13	6*	3.0	-14
2	Sodium Fluorescein	2.06	7	3.0	-17
3	Sodium Fluorescein	8.26	8	3.0	-14
4	Sodium Fluorescein	8.46	10	2.0	-14
5	Sodium Chloride†	31.1	7	3.0	-14

and neutral forms do not [66]. The fluorescein dye used in the source water is at low enough concentration that it near-fully dissociates into two sodium cations, and a fluorescein dianion. This behaviour of fluorescein has also been used to visualize the freezing of capillary flows [67, 68].

We grew icicles in a series of decreasing concentrations. Each series started with a relatively high concentration of feed water impurities added to distilled water, which was then diluted by half for each subsequent icicle. We maintained the same flow rate and air temperature within each series, but varied it between series. Five of these series are presented here, as summarized in table 6.1. The source water for Series 2 through 5 was degassed under vacuum for 10 minutes using an aspirator before each icicle was grown.

The flow rates we used were near the upper end of the flow rate ranges used in previous icicle growth experiments. Meano *et al.* [19] used flow rates between 0.2 g/min and 2.1 g/min, while Chen *et al.* [45, 12, 20] used between 0.5 g/min and 3.2 g/min. Higher flow rates can result in no icicle growth at all, depending on air temperature and the temperature of the feed water [20]. Our flow rates were consistent with robust icicle growth at the air temperatures shown in table 6.1.

The ionic concentration stated in mMol/kg counts the number of dissociated ions per kg of water. Our highest value of 8.46 mMol/kg is equivalent to 247 ppm NaCl, which is roughly the highest concentration with consistently upward moving ripples seen in previous work [12]. Even this maximum impurity concentration is rather low in absolute terms; it is only four times the impurity concentration of Toronto tap water [12], and less than 1% of 35 ppt standard sea water. Ripples are observed at concentrations as low as 16 ppm sodium fluorescein.

The fifth series of icicles uses sodium chloride (NaCl) as the primary impurity and 8 ppm sodium fluorescein dye. This amount of dye can be seen clearly by the camera, but has little effect on the actual freezing dynamics. We observed that when fluorescein comprises a smaller fraction of the impurities, the fluorescence does not quench as quickly. This series of icicles are more transparent, emit green light for longer times, and appear less orange after fully freezing. While the same behaviour of the liquid is observed, the fluorescence measurements had to be analyzed separately from the other four series.

6.3 Water distribution

The water which freezes to form the icicle generally does not completely cover the ice surface except in a short region near the tip. Over most of the icicle, the water flows down in a number of thin rivulets, leaving trails of water, but on icicles grown with higher concentrations of dye in the source water, there are also patches of fluorescent liquid adhering to the surface. These patches are wider and last longer than the trails. The rivulets may branch or reconnect with trails left by past rivulets, or feed into patches of liquid, and usually have a complex morphology as seen in Figure 6.1.

One can feel a rough texture on the surface at fluorescent patches by scraping it with a fingernail, indicative of dendritic growth or spongy ice. We are unable to image the microstructure directly in the current experiments. The clearer, uncovered portions of the icicle are quite smooth. The surface coverage tends to increase with dye concentration, a trend that is visualized in Figure 6.2, and quantified in Section 6.3.1 below.

The surface liquid is transient, but evolves slowly enough to be identified over several rotations of the icicle (*i.e.* over $\sim$15 minutes). The lifetime of rivulets and patches is short compared to the full growth time, so that the icicle above the tip area is built up stochastically from the contribution of many rivulets and patches.

6.3.1 Surface coverage

The relationship between the source water dye concentration and the amount of surface covered by liquid is our first evidence of a connection between the configuration of surface liquid deposits and the formation mechanism of icicle ripples. It is apparent to the eye in Figure 6.2 that higher concentration icicles retain more fluorescent liquid on their surfaces. We can quantify this observation using image processing.

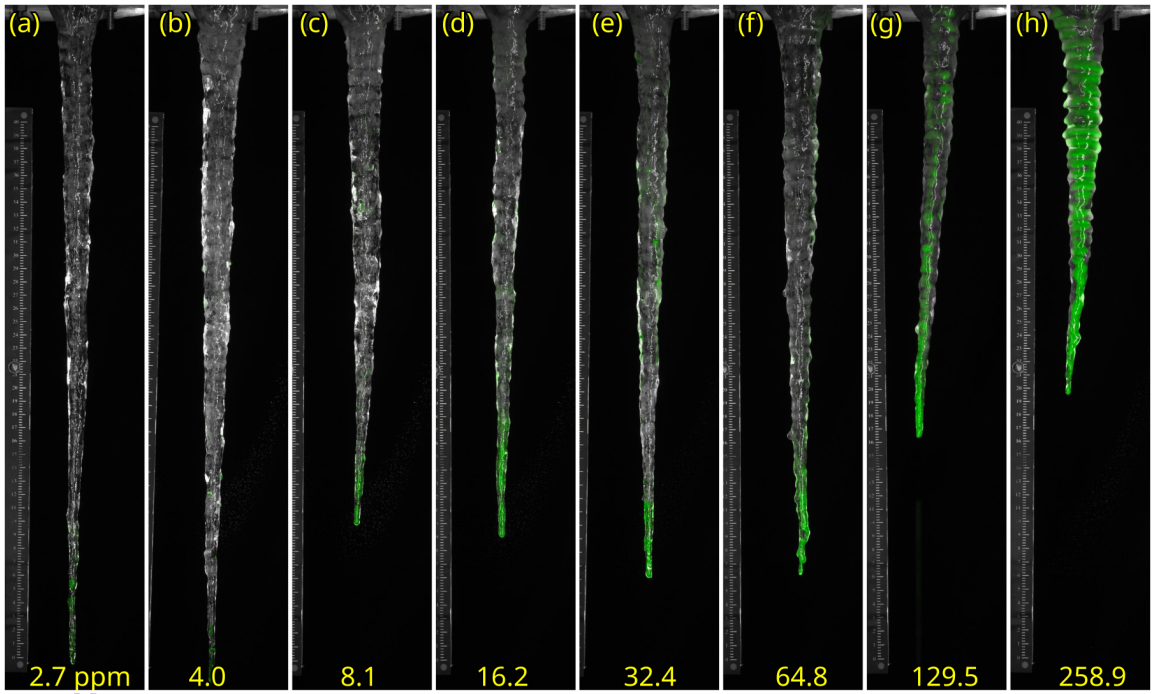

Figure 6.2: Each icicle of Series 2 pictured 2.5 hours into its growth. There is a clear correlation between the concentration and the amount of surface covered by liquid. In this series, the icicles grown with higher concentration are also shorter, thicker and exhibit more prominent ripples.

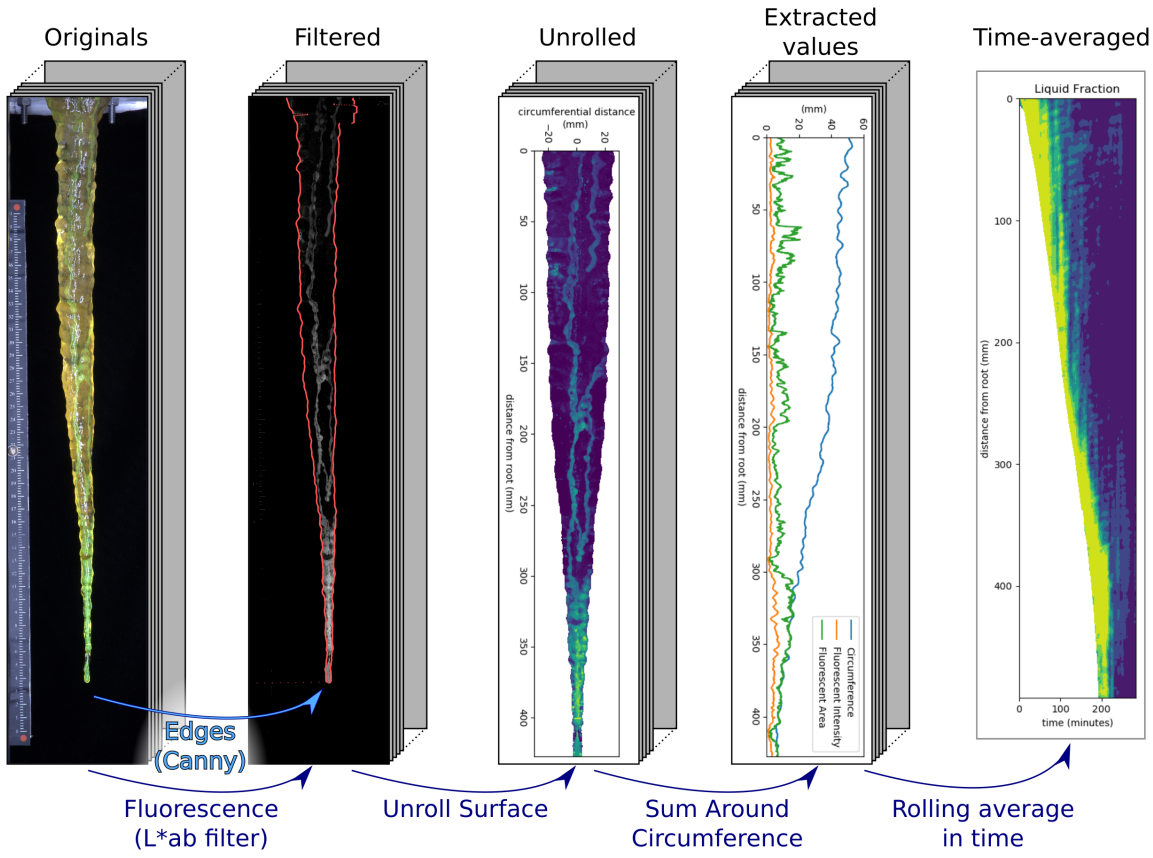

Figure 6.3: The image processing pipeline. The original image is filtered to extract edges and fluorescence. The icicle is "unrolled" and the fluorescence signal is summed around the circumference. All quantities are then time-averaged over a full rotation.

The green colour of fluorescence matches the negative a channel in the CIE-LAB colourspace. We used a Canny edge detector [64] to find the icicle shape, and isolated the a channel as the fluorescent *intensity* of each pixel. The CIE-LAB colourspace is a reference standard, in which the a and b channels are colour axes with 0 as colourless and values further from zero having more saturated colour. Our images typically ranged from 0 (grey) to -60 (green) in the a channel. For some measurements, the image was segmented by thresholding the intensity so that anything below $a = -6$ was counted as liquid. Choosing a threshold of -6 included all pixels with fluorescence, while reducing background noise.

Assuming a circular cross section, we "unrolled" each image and mapped each pixel to an area on the icicle surface. The intensity and liquid area measurements were summed around the circumference, and recorded as a function of the distance from the root. A rolling time average was then applied over one full rotation (16 frames). This image processing pipeline is illustrated in Figure 6.3.

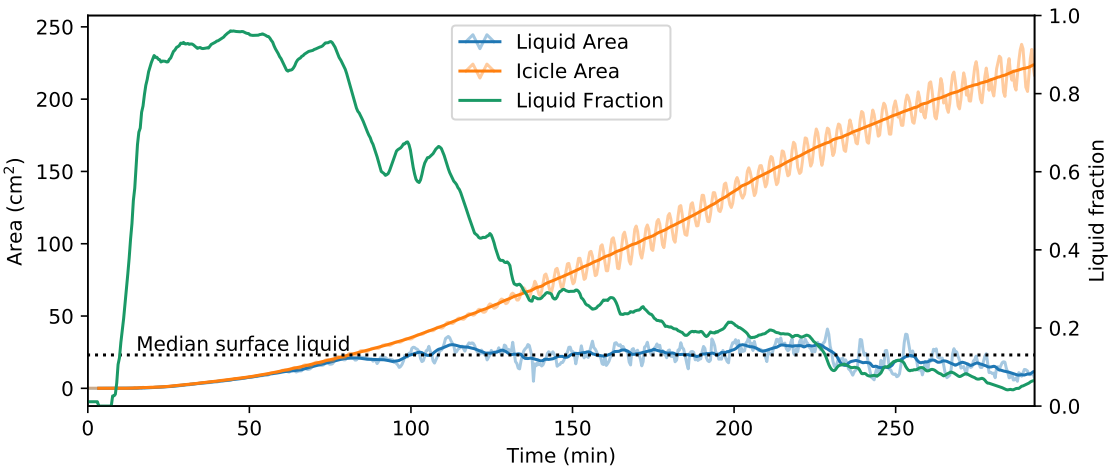

Figure 6.4: Total surface areas on an icicle ($Q = 3.0$ g/min, $T = -14.0$°C, $c = 1027$ μmol/kg) during its growth. All icicles show a common pattern; liquid covers the entire surface until a certain size is reached, after which the liquid area remains constant through the rest of the icicle growth.

Figure 6.4 shows the surface area, covered area, and liquid fraction, plotted against time for a sample icicle. The trends shown are typical for all icicles with a constant water feed rate. At first, liquid covers the whole icicle while the area grows nearly linearly and the covered area matches the surface area. This continues up to a certain time, after which the covered area plateaus and remains roughly constant for the rest of the growth time. The liquid fraction, conversely, stays close to 100% in the early stages, then falls off as $1/t$.

In order to compare icicles across different concentrations, the median covered area between 2 hours and 4 hours was selected to characterize the maximum supported liquid area. This statistical quantity varies significantly with concentration, as seen in Figure 6.5, with higher concentrations consistently supporting more liquid. This quantifies the trend observable by eye in Figure 6.2. A phenomenological fit of this trend to a simple power-law gives $A \propto c^{0.62}$, where A is the liquid-covered area and c is the concentration. This important and somewhat counterintuitive result has strong implications for any theory of the rippling instability, as discussed in Section 6.5 below.

Previous experimental work has established that the presence of ripples depends only on the concentration of impurities [12]; we also observe this in our dyed icicles. Clear ripples are present for concentrations above 64 ppm sodium fluorescein, while there are brief hints of ripples at some lower concentrations. The icicles with lower concentration that exhibited ripples were all part of Series 2, which had colder ambient

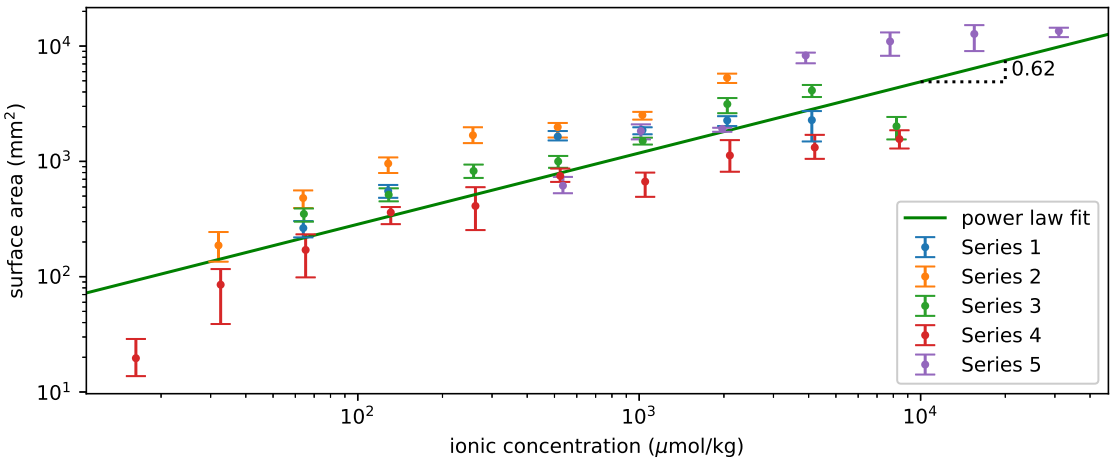

Figure 6.5: The median liquid covered area for icicles grown with varying feed water concentrations. Flow rates and temperatures for each series are outlined in table 6.1. Higher concentrations support more liquid at the surface, following a power-law trend for most of the range of concentrations, with an exponent of 0.62 ± 0.04. Series 4, which had a lower flow rate, shows the same trend but has a consistently lower covered area than the others.

air. Series 2 also consistently had higher surface coverage. The significant dependence of liquid coverage on concentration strongly suggests that the arrangement of surface liquid is directly linked to the mechanism of ripple formation. This inference is strengthened by the fact that in Series 2, we find ripples at lower concentrations than under other conditions, and also more liquid retained on the icicle surface. Furthermore, in all cases, the additional retained liquid appears to be contained in wider patches, rather than thin rivulets. To further establish the relationship between ripples and surface coverage, in the next section we compare the spatial distribution of liquid surface water, measured by fluorescence, to the topography of the icicle, measured by edge detection.

6.3.2 Liquid on ripples

In this section, we employ correlation techniques to reveal connections between ripples and surface liquid coverage. Visual inspection of rippled icicles shows that the liquid water often sits on the upper surface of a ripple. An example of this is highlighted in Figure 6.1. This distribution makes intuitive sense, because low Reynolds number gravity-driven flow might be expected to cause liquid to accumulate of the upper surface, while draining it from the underside. Accumulation on the upper surface,

leading to additional ice growth there, would also intuitively explain the observed upward migration of ripples [12, 19].

We quantitatively compared the liquid distribution to the topography using cross-correlation. The topography on the sides of the icicle can be measured directly using edge detection on the images. The liquid, however, is identified with fluorescence on the front surface, facing the camera. Because the icicle was rotated right-to-left in the view of the camera, we cross-correlated the right edge to the fluorescence one quarter rotation later. The fluorescent intensity for the middle 3/8 of the "unrolled" icicle surface (as described in Section 6.3.1) was used to estimate the liquid distribution. In order to focus only on the ripple pattern, we de-trended both the topography and the fluorescence using a discrete cosine transform, and identified the cross-correlation peak closest to zero.

Figure 6.6 shows results for the cross-correlation between the right edge and the fluorescent intensity for a particular icicle. For that icicle, between 90 minutes and 210 minutes of growth, the median offset distance between the fluorescence signal and the topography was 3.41 mm, or about 1/3 the ripple wavelength, with the liquid preferentially located on the upper side of the ripple.

These measurements were repeated for all icicles that exhibited ripples. The liquid areas were consistently above the ripples, with a median displacement of 1.88 mm and mode of 3.1 mm over all rippled icicles. Icicles without ripples cannot be analyzed the same way, because both the amount of liquid and variation in topography were too small to reliably measure.

The results of this section show that higher dye concentration in the source water is correlated with much higher surface liquid coverage, with the additional liquid preferentially located on the upper surface of the emergent ripples. This coverage increase is more than a geometric flow effect, however, as the coverage pattern becomes dominated by patches rather than rivulets, with the patches associated with increased surface roughness.

The important effect of impurity concentration on surface wettability is most obvious on icicles grown at the highest concentrations, where nearly the whole surface above and below the ripples is covered. These icicles have a distinct surface roughness that can be readily observed by scratching. This rough surface probably retains more liquid water because of its increased wettability *via* the Wenzel effect [69]. Similar surface roughness can be detected on the upper side of ripples at medium concentrations, while non-rippled icicles have very smooth surfaces. It is likely that the presence of impurities also directly modifies the surface energy of the ice; ionic

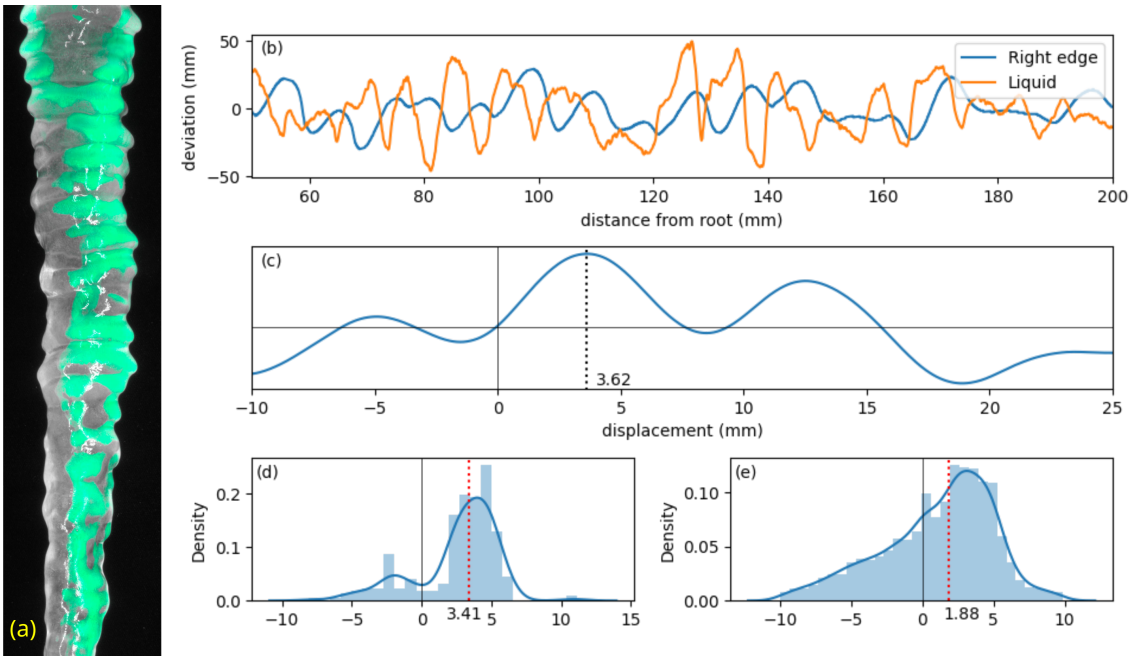

Figure 6.6: A rippled icicle with dye concentration of 259 ppm (2053 μmol/kg), grown at flow rate 3.00 g/min and air temperature -16°C. (a) It is clear by eye in a saturated false-colour image that patches of liquid tend to be located above the ripples. (b) A plot of the topography (blue) and fluorescent intensity (orange) for this frame shows that fluorescence peaks several mm in advance of the topography. (c) A cross-correlation of these two measurements gives a offset-distance of 3.62 mm at that time. (d) The distribution the peak closest to zero in the cross-correlation for each frame has a clear bias for liquid sitting above ripples, with a median offset (red dotted line) of 3.41 mm. (e) This offset in the cross-correlation is still evident when the cross-correlation peaks are averaged over of all rippled icicles.

impurities trapped at surfaces are known to effect contact angles and other equilibrium wetting properties [70].

In the following section, we investigate the influence of these effects by growing ice on preformed cylindrical substrates designed to separately test the effect of various properties of the ice surface.

6.3.3 Liquid near the tip

In most icicles, we observed that a region near the tip of the icicle was always fluorescent, even when the rest of the icicle surface is clear, which suggests that it is always ensheathed by a thin film of liquid. This is the one region where the thin-film model for ripple growth discussed in Chapter 2 may apply.

The size of this covered region was measured by considering the fraction of the

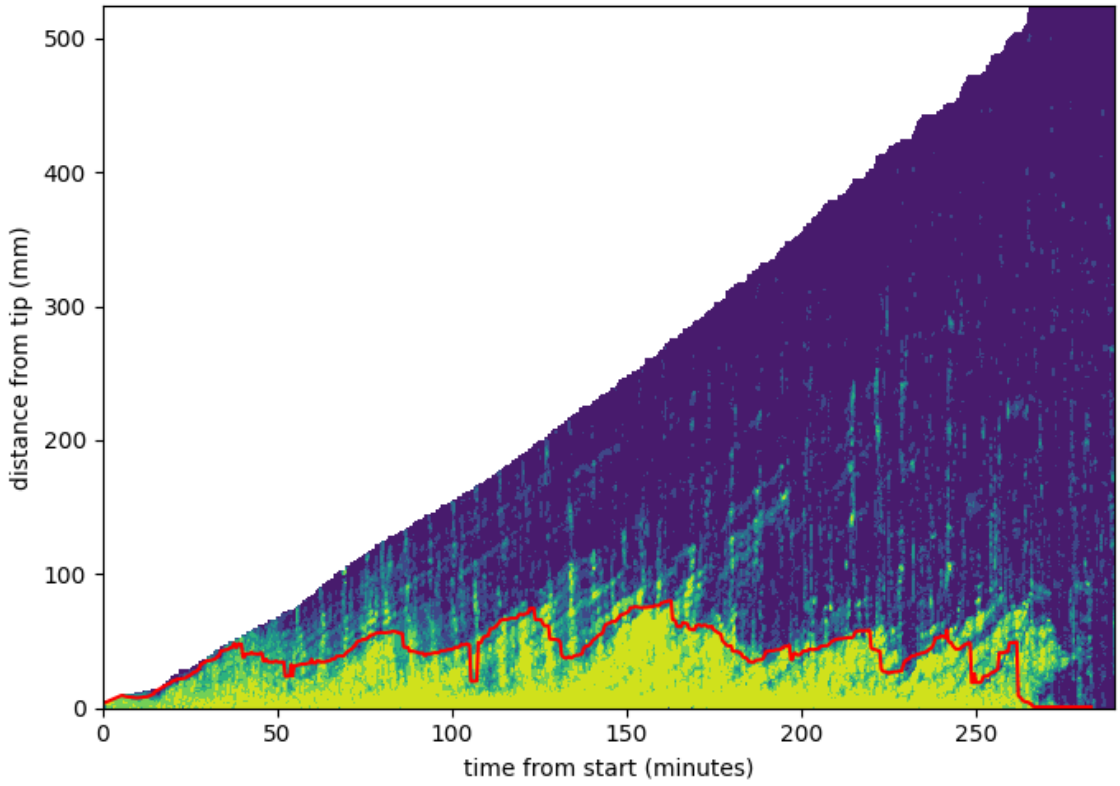

Figure 6.7: Sample of how the length of the "completely covered" tip is measured. The measured tip length is drawn over the contour surface liquid fraction. This icicle was grown in -14.1°C air using 259 μmol/kg source water fed at 3.0 g/min.

surface covered by liquid. This time, we use the distance from the tip as the coordinate before the time-averaging. Any distance where the liquid fraction is greater than 50% is considered "covered," and the closest uncovered distance to the tip is the "tip-length." A sample of this measurement is presented in Figure 6.7.

The tip-length during typical icicle growth can be compared between icicles. We consider *typical growth* to be between 90 min and 210 min, and consider the interquartile range of tip-length in that period for each icicle. The ranges are shown in Figure 6.8.

The length of the covered tip increases slightly with higher concentrations, consistent with the overall increase in surface liquid. At the highest concentrations, we see a sudden decrease in the amount of liquid at the tip At those high concentrations, almost all of the water is adhered to the upper regions. The lack of water at the tip of the icicle will cause it to stop growing in length. This cause of cessation is different from the proposed mechanism in Chung and Lozowski's model of marine icicle growth, which predicts cessation due to salt accumulation and freezing point

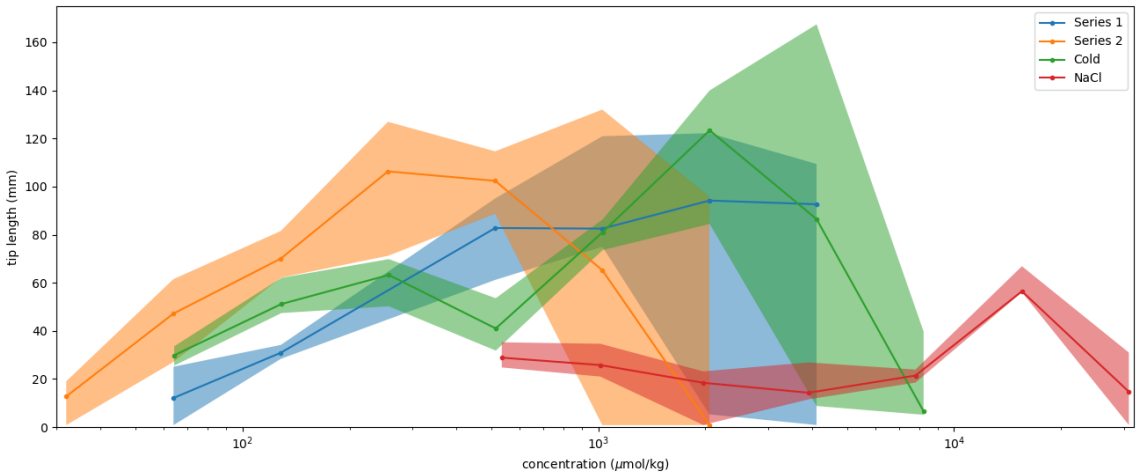

Figure 6.8: Interquartile ranges of the liquid covered tip length for our 4 series of icicles, measured between 90 min and 210 min after start. Temperatures and flow rates are as described in Table 6.1

depression [14]. Both processes may contribute to the shorter length of saline icicles.

The reason for the tip to be fully coated is not understood. One possibility is that the small radius near the tip contributes to capillary forces that pull the liquid upwards.

6.4 Cylindrical substrates

In previous sections, we saw that the amount and location of liquid on the surface of an icicle is affected by the concentration and topography. The surface of ice is still an area of active research, with many unanswered questions about the contact angle, surface energy, and quasi-liquid layer [7, 71, 72]. While quite interesting, those theories and experiments focus on pure ice in very controlled conditions near equilibrium. Wettlaufer *et al.* do consider how impurities would affect the quasi-liquid layer [73], but this is also near equilibrium conditions. Because icicles grow far from equilibrium and with a complicated flow involving a moving contact line, we chose to consider more macroscopic properties that may affect the wetting dynamics. The concentration may play a role through its modification of the surface energy, or by creating a rough surface and reservoirs (*e.g. via* dendritic growth). Larger scale topography can trap water in small depressions, or slow the gravity-driven flow.

To isolate these effects, we replaced the wood support with various long pre-formed cylinders of ice which acted as substrates for subsequent ice formation. The cylinders

Table 6.2: The characteristics of a series of runs in which dyed water was dripped onto rotating preformed cylinders of ice with various surface treatments and lengths. All cylinders were initially formed in a mold using distilled water.

cylinder	concentration (ppm)	flow rate (g/min)	temperature (°C)	treatment
control	184	3.0	-13.7	No surface treatment.
dye bands	184	3.0	-13.7	Saturated sodium fluorescein solution painted in bands to create regions of high surface concentration of dye.
roughened	184	3.0	-13.7	Sanded with 120 grit emery cloth to create a rough surface.
grooved	184	3.0	-13.7	grooves of various widths sawn into the cylinder to approximate ripples.
truncated	440	3.0	-11.5	no surface treatment, short cylinder.

were frozen in a copper pipe mold, from distilled water which had been degassed under vacuum for 30 minutes. A cotton string core reinforced the otherwise fragile cylinders. Table 6.2 lists the properties of each cylinder. For each cylinder, dyed water was delivered to the top of the rotating cylinder in the same way as before.

Strikingly, no ripples form at any time during the growth of the *control* cylinder, seen in Figure 6.9. From start to finish, very little liquid water is retained on the surface. All of the water descends quickly in thin rivulets, between 2 mm and 5 mm in width, and only a few patches dwell on the surface. This flow leads to a slow radial growth rate of 2.4 mm/h, with the impure ice eventually reaching a diameter several times that of the original pure ice substrate. It was apparent that the ice that formed on the *control* cylinder is quite different from that of normal impure icicles grown under otherwise identical conditions. The additional ice is still impure, as is evident from its orange color, but is more transparent than the other icicles and cylinders, which suggests fewer impurities were trapped.

The three long surface-modified cylinders from table 6.2 are shown in Figure 6.10. We modified the surface concentration by painting dye on some regions (*dye bands*), surface roughness by sanding (*roughened*), and the surface topography by sawing grooves (*grooved*). Placing these features in the middle of a long cylinder also isolates the effects from the start and end of a finite domain. In each case, the resulting ice accretion pattern differed from the control, each exhibiting some ripples, but in no

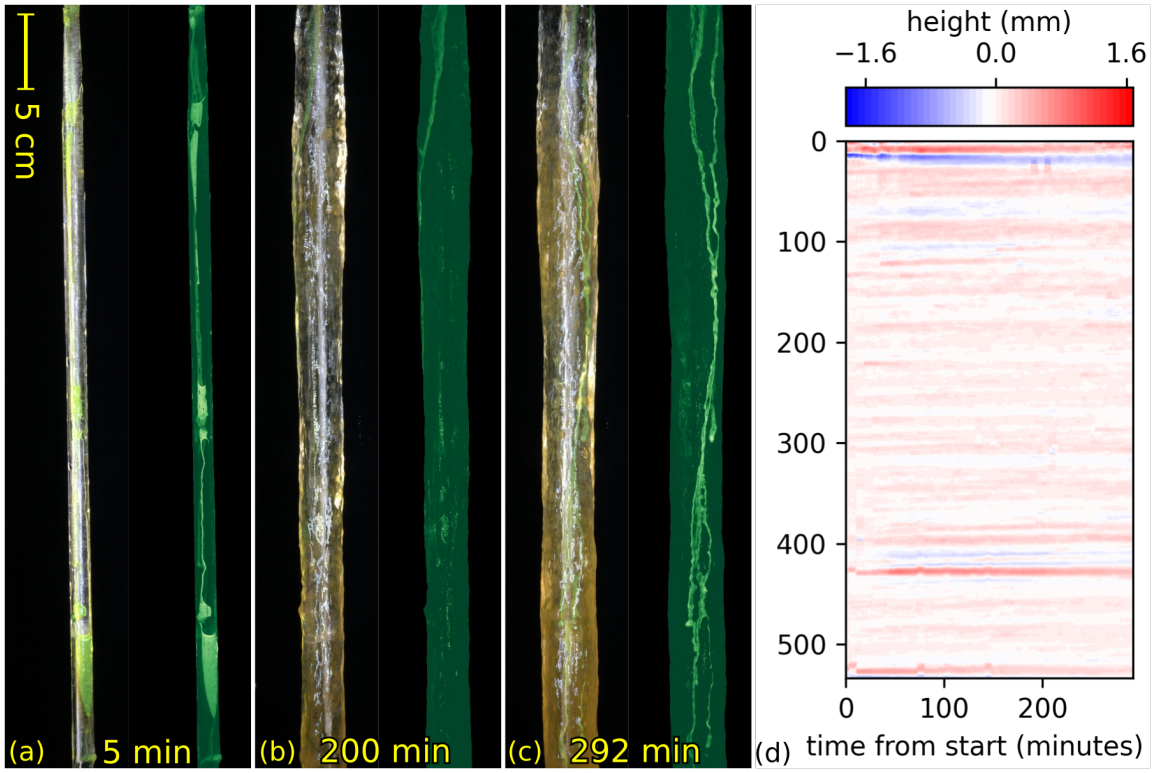

Figure 6.9: The control cylinder, imaged at various times during growth, shown next to a false colour image to highlight the liquid regions. Branching and merging of rivulets is clearly visible in panel (c). Panel (d) shows the deviation of right edge from its mean throughout growth. No clear ripple pattern forms.

case did they sustain a large amplitude ripple pattern resembling that of an icicle grown under the same conditions.

Some small ripples briefly formed below the largest band of fluorescein on the *dye bands* cylinder, as indicated in Figure 6.10. However, the ripples never spanned the circumference of the cylinder, and their growth was not sustained. The initial ripples remained small, then slowly smoothed out over the remaining hours of growth. In early times, the liquid spread out over more of the surface below that large band, so that more liquid was retained in the region where ripples began to form. At 18 minutes, we measured the liquid width as 6.3-10.4 mm (25^{th} to 75^{th} percentile) above the wide band, and 13.5-18.1 mm below the wide band. The increased width compared to the *control*, even above the wide band, may be caused by the less concentrated bands near the top of the cylinder. At late times, the liquid distribution on the *dye bands* cylinder resembled the thin rivulets of the *control* cylinder, but the ice itself was much more opaque and bumpy at the $\sim$1 cm scale. This liquid coverage was also reflected in the radial growth rate: for early growth, the rate was 3.5 mm/h, while at later times it matched the *control*'s gowth of 2.4 mm/h. In the first few minutes, the band appears to have released dye into the water, changing the concentration in the downstream region where small ripples formed.

The topographic features on the *grooved* cylinder, indicated on Figure 6.10(b), had some significant effect on ripple formation. The thinnest grooves had a very minor effect that would be easy to miss, but a 5 mm wide groove caused a large rib that spanned the circumference of the cylinder, followed by a small train of ripples that formed upstream. These ripples began immediately because the wide groove held more water at its top, leading to more liquid covering the entire surface above the wide groove. But again, at later times, less water was retained on the surface, and ripple growth was not sustained. The first ripples that formed above the wide groove lasted the longest, and remained as the highest diameter after all the ripples smoothed out. The appearance of the ice in well-coated areas was very similar to the ice of the *dye bands* cylinder.

Ripples quickly formed on the *roughened* cylinder and became disordered at later times. These ripples nevertheless remained considerably smaller in amplitude than those that would be formed on an icicle grown with the same flow rate and concentration. However, of the three long cylinders, the *roughened* cylinder showed the greatest initial difference in liquid distribution as compared to the *control*. Liquid water clearly spread more widely than in the previous cases, covering half the circumference over most of the length. The spread was widest at the onset, and narrower

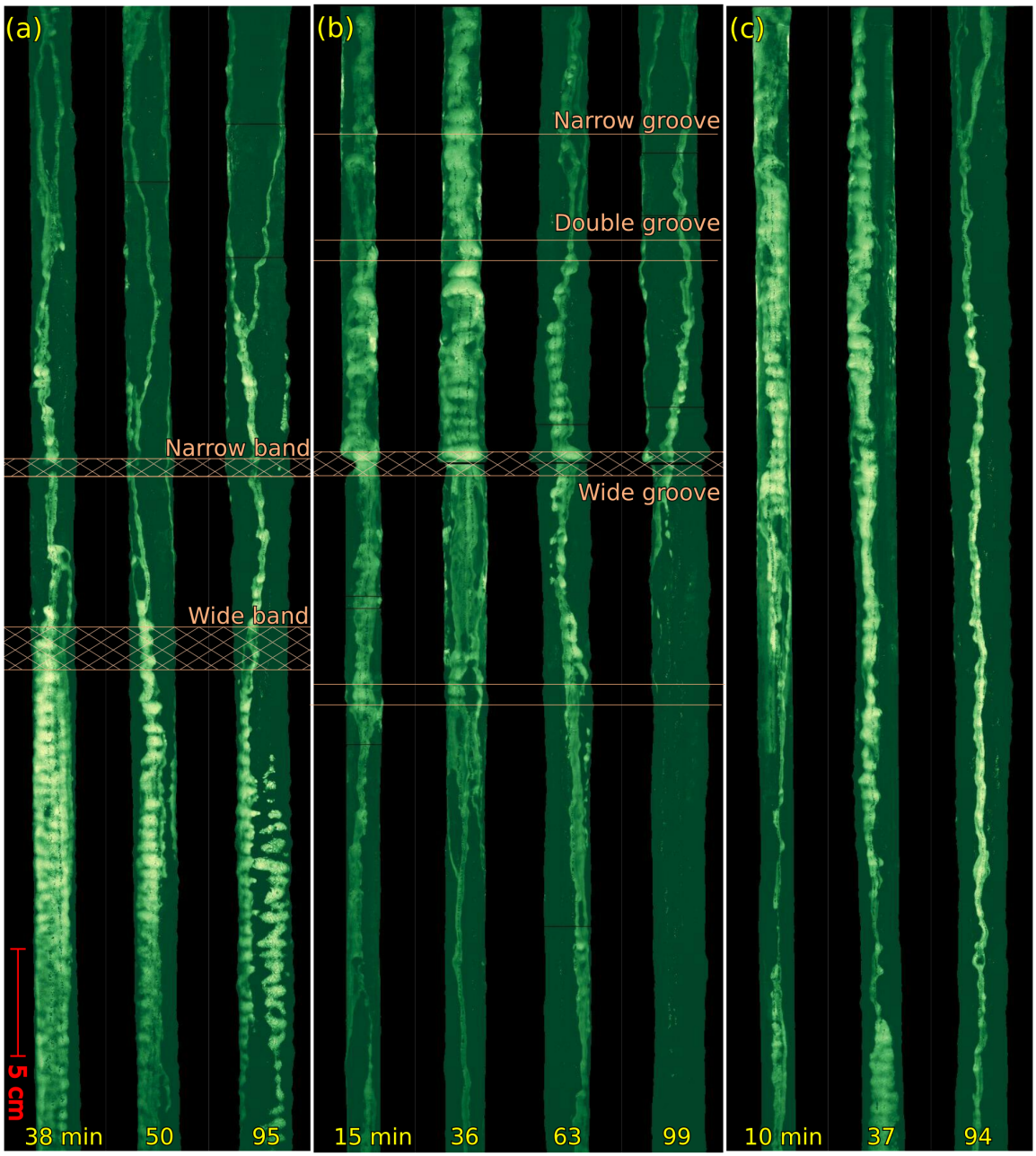

Figure 6.10: Three long cylinders with surface modifications and how they affect liquid distribution and ripple formation. The areas with more liquid coverage exhibit ripples. (a) The *dye bands* cylinder exhibits transient ripples directly below the wide band with the highest concentration, but below not the narrower bands. (b) The *grooved* cylinder developed a train of transient ripples above the largest groove (indicated by the arrow). Narrow grooves had almost no effect. (c) The *roughened* cylinder exhibits the most consistent spreading of liquid along its length and the formation of small disordered ripples.

lower down the icicle, because most of the water had been used up by then. For the first hour, larger patches remained on the surface, preferentially on the upper surface of ripples. After another 30 minutes, the water began to descend in small rivulets as seen on the *control*. We believe this is because the ice began to freeze over completely before more liquid replenished the reservoirs. When the ice is frozen completely, the surface becomes smooth and impurities are isolated from the surface, so it behaves like the pure ice of the *control* cylinder. The radial growth rates were nearly identical to the *dye bands* cylinder: 3.6 mm/h at the start, and 2.4 mm/h later in growth.

The *truncated* cylinder, which was simply a shorter version of the *control*, strikingly illustrates the difference between ice growth on cylindrical substrates and in icicles. It is analyzed in detail in Figure 6.11. The first ripple formed around the bottom edge of the *truncated* cylinder, and more were robustly generated along the length of the pendant icicle. Eventually, additional ripples started to form on the *truncated* cylinder above the first one, and became visible at 100 minutes and 160 minutes into icicle growth. This upward propagation is consistent with the tendency of icicle ripples to travel upward during growth for low impurity concentrations [12]. The source water flowed uninterrupted down the surface of the cylinder in rivulets as in the *control* cylinder, then fed a conventional icicle at its base. As growth progressed, the icicle forming below the base became thicker than the section on the preformed cylinder.

The stark contrast in water adhesion and diameter growth between the *truncated* cylinder and its pendant icicle shows that there is a fundamental difference in the surface characteristics between the impure ice in an icicle and impure ice formed on a pure substrate, as in the *control*. It seems likely that the internal structure of the ice in each case differs as well, because less dye appears trapped inside the ice covering the cylinder. The internal structure and trapped impurities inside icicles is explored in Chapter 7.

The ripples that formed on the pendant icicle, as well as the few just above the end of the *truncated* cylinder, were more persistent, and grew more robustly to a much larger amplitude than any ripples in the other cylinder experiments. These observations have important implications for any theory of ripple formation, as discussed in Section 6.5 below.

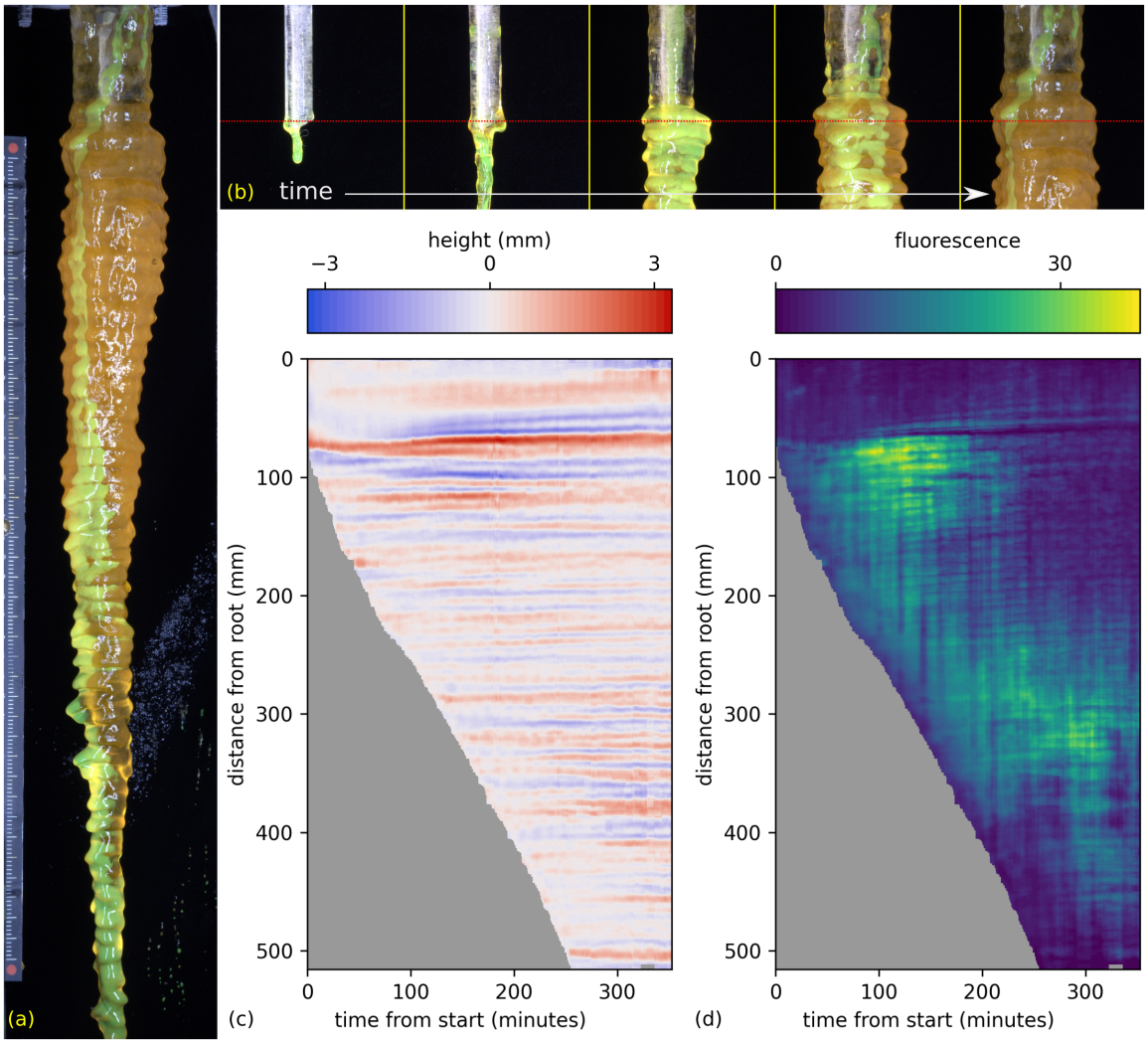

Figure 6.11: The *truncated* cylinder: (a) forms a typical icicle from its base, which grows thicker than the ice grown over the cylinder. (b) The first ripple starts just below the end of the cylinder, then migrates upward. New ripples form above the first, as shown in (b), and in (c), a space-time image of the topography. (d) A space-time image of the fluorescence shows that almost all the liquid is retained on the new ice, and correlates well to the ripples. The vertical bands in (d) are a result of only half the icicle being visible in any one image.

6.5 Discussion

A common assumption to all existing models of icicle growth is that the icicle is fully ensheathed by a thin flowing water film [41]. A uniform thin film flow is the basis of several theories to explain the ripple instability [19, 25, 26, 27, 28, 30, 31, 29], and the overall shape of icicles [44]. Within the thin film, a typical Reynolds number of 0.1 - 4.0 can be estimated for ordinary conditions [19], provided there is a laminar Poiseuille flow. However, the actual situation is that the flow is spatially and temporally intermittent, preferring to flow down the surface in rivulets, except for a short region near the tip.

The assumption of a completely wetted surface might seem to be justified in equilibrium because solid ice is known to support a "quasi-liquid" layer of water on its surface which would appear to favour complete wetting [48], and a hence a zero contact angle. However, some sources posit that the existence of a quasi-liquid layer does not imply a zero contact angle [72], and that, in fact, the surface tension balance at the contact line provides for a positive contact angle. At warmer temperatures, complete wetting may be observed because there is a liquid layer for another reason [7], and suggest this liquid layer disappears at about -13°C, near the temperature where our experiments were done. Other experiments on the structure of the ice surface find that there is a disordered surface as low as -90°C with additional layers melting above -16°C, and quasi-liquid drops and film above -2°C [71]. Our experiments do not shed light on the liquid layer, and in fact, the ice surface in the presence of water should never be more than a few degrees below the freezing point. Previous experiments [45, 12, 20] have shown that the ambient temperature does not strongly effect the emergence of ripples, other than to vary their overall speed of growth; there is no obvious change in the phenomena near -13°C.

The relevance of purely thermodynamic considerations is suspect, however, because the surface of a growing icicle is an open system driven far from equilibrium by latent heat release and flow, giving rise to large temperature and concentration gradients. Our observations indicate that the icicle surface is in a much more dynamic state with only partial liquid coverage of the surface. We now turn our attention to the existing continuum theories of icicle ripples, since our observations speak mainly to macroscopic phenomena.

The only mathematical model for icicle ripples is the thin-film model discussed in detail in Chapter 2. While the analysis of the model showed that it cannot predict icicle ripples, the observations of surface liquid above show a fundamental flaw in its

assumptions. All variations of the thin-film model begin with the assumption that the icicle is covered by a uniform sheath of flowing liquid water in the basic flow state. The basic flow state is assumed to be a simple, steady parabolic shear flow with surface tension and its internal fluid-mechanical instabilities are ignored.

In stark contrast to that model, the surface of an icicle is not fully ensheathed in a liquid film, except for a short region near the tip. Instead, the flow state consists of transient rivulets and longer lasting patches of liquid. The amount of liquid retained on the surface is tied to both concentration, and the size of ripples. With higher concentrations, more liquid is retained, and larger, more robust ripples form. This trend is consistent among different temperatures and flow rates. While a thin-film instability might be relevant near the tip, it is evident that the ripples grow from a much more stochastic flow pattern than is assumed by an axisymmetric model. The actual unsteady flow state does not reduce to a simple parabolic shear profile, even in time average. Thus it is more plausible that the concentration-dependent flow patterns couple positively with the topography evolution to cause ripples.

Furthermore, if the icicle is ensheathed in liquid water, as in axisymmetric models, it follows that the water must be supercooled, in order for latent heat released at the ice water interface be transported radially outward. This is not the case for the observed flow state, in which it is possible for the liquid in the rivulets to remain above freezing, while surrounding areas of bare ice may be colder. Significant azimuthal temperature gradients will certainly exist. Thus the temperature distribution, as well as the concentration distribution which is transported by the same flow, will be very different than allowed by any axisymmetric model. Further studies of the temperature distribution on growing icicles would help illuminate these points.

The liquid also preferentially dwells on the upper surface of ripples/topography, which would help explain the upward migration of ripples that has been previously observed [19, 45, 12, 20], reinforcing the hypothesis that the flow patterns provide positive feedback to the topography evolution. Topography would be expected to modulate the downslope effect of gravity, but there may also be other causes of this localization. Notably, the ice on the upper surfaces of the ripples has a rough texture, which may enhance the wetting there.

Our investigations using cylindrical substrates demonstrate that the flow of water over the surface of actively growing ice depends on surface texture, presence of impurities at the surface, gravity, and topography (both slopes, and cylinder terminations). On conventional icicles at high concentration, liquid is increasingly drawn onto rough areas of the surface and interacts with the topography differently than at

low concentration. The failure of the control cylinder to produce ripples despite sufficient feed-water concentration suggests a further potential positive feedback between topography, concentration, and the exposed (internal) structure of impure ice.

The *banded* and *roughened* cylinders show some spreading of liquid due to roughness and trapped impurities, leading to small-amplitude ripples. However, a stop in the flow as caused by a wide groove (*grooved* cylinder) or the end of the substrate (*truncated* cylinder) has a more significant effect. A notable difference between the surface effects (*banded* and *roughened* cylinders) and the topographic effects (*grooved* and *truncated* cylinders) is that ripples do not always wrap around the circumference to form ribs. For the ripples to wrap around the icicle, it appears that the liquid must first wrap around the whole icicle. This can be seen most clearly at the end of a surface (e.g. at the tip or above a groove). Most rippled icicles have ripples that wrap completely around the circumference, which suggests that the ripple is initiated at the tip, consistent with the ripples seen propagating up from the end of the *truncated* cylinder.

The very different shape evolution of the *truncated* cylinder and its pendant icicle points to a significant difference between the actively growing ice, and the "inactive" preformed ice. The ice actively growing from impure water may have a higher concentration of impurities trapped near the surface, and also the rough texture that was emulated in the *banded* and *roughened* cylinders. The liquid is also wider in those areas, suggesting that it spreads out around the surface more easily. Once some ice has completely frozen over, fully encapsulating the impurities, it behaves differently: the surface does not retain as much liquid, but instead allows it to freely flow in rivulets to the bottom of the ice. This suggests a further potential positive feedback between topography, concentration and the internal structure of the impure ice may be present. Experiments on the internal structure of icicles is presented in Chapter 7.

Freezing point depression due to the presence of impurities may still play a minor role in the actual rivulet-dominated flow. The rough surface texture observed on ripples can trap the impurities inside a spongy ice matrix. According to mushy layer theory [13], as the solid fraction increases without adequate transport of impurities, the local concentration increases, further depressing the freezing point. These mechanisms can cause additional changes to the local temperature and freezing rate that are not captured in a solid ice model. One such effect could be a slower freezing rate relative to the flow and spreading rates, enhancing the interaction between the incoming feed water and the "wet" areas on the surface. It is not possible to observe these dynamic effects directly with the current experiment due to its limited

time resolution and the difficulty of isolating transient rivulets on growing icicles. Experiments focussing on an individual, controlled rivulet may shed light on these small-scale processes. For example, one could measure the advancing contact angle and velocity of the front of a rivulet on an inclined plane of ice. Monier *et al.* have performed a similar experiment [68], but on aluminum with different temperature conditions.

Finally, our observations challenge the assumption that the ripples are the result of a linear instability. Rather, they suggest that small but finite perturbations might be required to trigger the appearance of ripples. A linear instability would have been expected to produce ripples on the *control* cylinder, but no ripples were observed. Ripples only appeared on the *grooved* cylinder when a sufficiently large topographic perturbation was encountered. On the other hand, rippling was also observed on the *roughened* cylinder without finite topography, as long as a sufficient amount of liquid was retained by the rough surface.

Chapter 7

Interior inclusions and grain structure

This chapter presents work that has been published in Physical Review E [2]. The experiments and analysis was performed by John Ladan. Stephen W. Morris contributed to the discussion of the results.

Rippled icicles grown with impurities in the source water often have a "foggy" appearance with small bubbles or inclusions trapped inside. Knight [38] and Maeno *et al.* [19, 18] suggested that these inclusions are air bubbles, which would be evidence of rapid freezing, forming spongy ice. Knight further reasoned that the rapid, dendritic growth implies that the basal plane of crystal grains in such icicles was perpendicular to the icicle surface, and the air bubbles are evidence of liquid draining from the ice.

In this chapter, we present the first detailed study of the pattern of inclusions in the interior of icicles, and discuss their implications for the mechanism of the ripple-forming instability. Our work extends earlier observations of natural icicles by Laudise and Brand [37] and Knight [38], and the laboratory work of Maeno *et al.* [18, 19]. Using laboratory-grown icicles and various species of impurities, including fluorescent dye, we show that a certain fraction of the impurities remain trapped inside the icicle, forming inclusions of liquid within the ice. These liquid inclusions are evidence of cellular or dendritic growth as described by the Mullins-Sekerka instability [22, 23]. However, the concentration of impurities in the source water is below the critical concentration, as discussed in Chapter 1. The inclusions are organized into chevron patterns aligned with the peaks of the ripples. Within the chevrons, a substructure of crescent-shaped structures is observed, reminiscent of growth rings in trees. We also examine the crystal grain structure of laboratory icicles, with and without impurities.

Impurities in ice are usually expected to collect at the grain boundaries [48], but in icicles, the grain structure does not align with the pattern of inclusions.

The polycrystalline nature of icicles is well known [41]. It has also long been observed that some icicles contain significant amounts of unfrozen liquid water within their ice matrix — so-called *spongy ice* [41, 38, 18, 19]. Knight [38] attributed the foggy appearance of rippled icicles to *air bubbles* trapped inside the ice, which he proposed was the result of more rapid cooling near the ripple peaks. Knight further suggested that the sponginess indicated a particular crystal orientation, the c-axis parallel to icicle axis, which conflicted with the observations of Laudise and Brand [37], who found that the c-axis was mainly perpendicular to the icicle axis. These reports on natural icicles were made before the strong connection between feed-water impurities and ripples was established [12].

We show in Section 7.2 that the foggy appearance is not due to trapped air bubbles, but rather due to small features we call *inclusions* which are actually pockets of highly impure liquid trapped inside the ice matrix. We examine the spatial distribution of the inclusions, which are organized into bands making a *chevron* pattern. Within the chevrons, we find that the inclusions are further organized into smaller substructures we call *crescents*. Chevron patterns in natural icicles were previously noted by Maeno *et al.* [18, 19]. The chevrons and crescents align closely with the growth and upward migration [12] of ripples on the icicle surface, as discussed in Section 7.2.3. In Section 7.2.6, we visualize the crystal grain structure within the ice and show that it is sometimes correlated with the ripple growth, with the liquid inclusions trapped within the crystallites, not at their boundaries.

In Section 7.3, we discuss how the pattern of inclusions may be related to the patchy nature of the surface liquid coverage [1], and how our observations could inform future models of icicle growth.

7.1 Experiment

A total of 51 icicles were grown for sectioning in the icicle machine described in Chapter 3. The source water was mixed, using distilled water with NaCl (30 icicles), Dextrose (5 icicles), or Sodium Fluorescein (16 icicles) as an impurity. The icicles were grown in several series, starting with the highest impurity concentration, followed by feed water diluted by half for each subsequent icicle. For one quarter of the icicles, the feed water was degassed under vacuum while stirred by a magnetic stirrer for 10 minutes directly before the icicle machine was started. In our tests,

this method reduced dissolved oxygen by $\sim 95\%$, with less than 0.01% loss of water. The typical feed-water flow rate was 3.0 g/min, apart from one series of three Sodium Fluorescein icicles. The air temperature was held at values between -14.0°C and -11.5°C, consistent within ± 0.25°C for each series (-11.5°C, -12.5°C, -13.5°C for Dextrose, and -14.0°C).

The ionic concentration of source water used ranged between 0.04 mMol/kg to 43.8 mMol/kg, which is equivalent to between 1.2 ppm NaCl to 1280 ppm NaCl. This range covers a wider range than would be expected for natural icicles. Chen *et al.* measured the concentration of melted snow from a rooftop as 0.25 mMol/kg, and 2.9 mMol/kg in tap water from Toronto, ON. [12]

7.1.1 Measuring the topography and inclusions

The topography of each icicle was extracted from the time-lapse photography during growth using the methods described in Chapter 4. Each icicle was imaged over 700 times during its growth, resulting in detected edges consisting of tens of thousands of data points. We thus have rather complete information about the evolution of the icicle's external topography during growth, which can then be compared to the distribution of impurity inclusions at the end of growth process, which could be obtained by sectioning the icicle at a known rotational position.

After growing, the icicle and its support were removed from the box, and the icicle was sawed off below the tip of the support cone. It was then stored in a freezer at -24°C until sectioning. Cross sections were taken parallel to the icicle axis by melting each icicle on aluminum plate to approximately 3 mm thickness. The section thickness was selected to ensure there were enough interior inclusions visible to see a clear pattern, without occlusions from off-center layers.

Images of the sections were taken in a chilled box with a unidirectional light source, which scattered off inclusions inside the ice. The sections were placed on a black rubber mat with a steel ruler placed beside so that the resolution of each image could be measured. Before imaging, the sections were wiped with a lint free paper towel to remove liquid on the surface and inside exposed inclusions. For the fluorescent dye, the icicles were illuminated with a strip of UV LEDs. The camera (a Canon EOS Rebel T2i SLR with a Canon EF-S 18-55 mm lens) was positioned above the chilled box on a frame, and the images were later measured using ImageJ [74]. The results of this analysis are presented in Section 7.2.3 below.

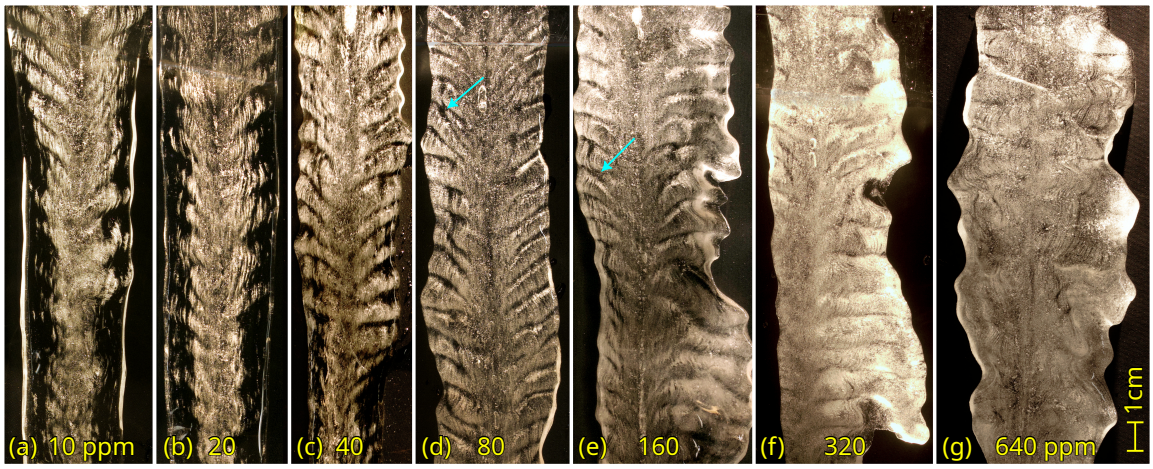

Figure 7.1: Inclusions are visible at a wide range of concentrations in NaCl icicles. At the lowest concentrations (a,b), the majority of the icicle is pure ice. As the concentration increases, trapped impurities collect in bands that exhibit a chevron pattern (c,d,e). The transitional concentration (f) has thin lines of almost pure ice. At high concentrations (g), the whole of the ice is foggy with inclusions. The blue arrows mark ripple stopping events.

7.2 Observations

Inclusions are seen at a wide range of concentrations in icicles grown with NaCl, as shown in Figure 7.1. As the impurity concentration in the feed water increases, the number of inclusions increases, as does the amplitude of the ripples. At the lowest concentrations, the majority of the icicle is a pure phase of ice (Ice Ih according to the freezing conditions). In these nearly pure icicles, the inclusions organize themselves into *crescent* shapes. These structures within the ice trace the shape of the ripple peaks and are faintly visible in the upper part of Figure 7.1(a) and more clearly in the microscopic view shown in Figure 7.2. The crescents are formed of elongated clusters of individual inclusions.

As the concentration increases, the crescents of inclusions layer radially upon one another forming visible *chevron bands* of mixed-phase ice separated by lines of pure ice. These are most clearly seen in Figure 7.1(c,d,e). The chevrons are angled upward, reflecting the upward migration of the ripples during growth at these concentrations. At 320 ppm NaCl, the single-phase ice is no longer present, and the icicles are saturated with inclusions, as shown in Figure 7.1(g). At these concentrations, crescents and chevrons are no longer distinguishable from the general fogginess of the ice.

The small spherical inclusions, which were previously thought to be *air bubbles* [18, 38], are actually pockets of liquid with a high concentration of impurities, as we will

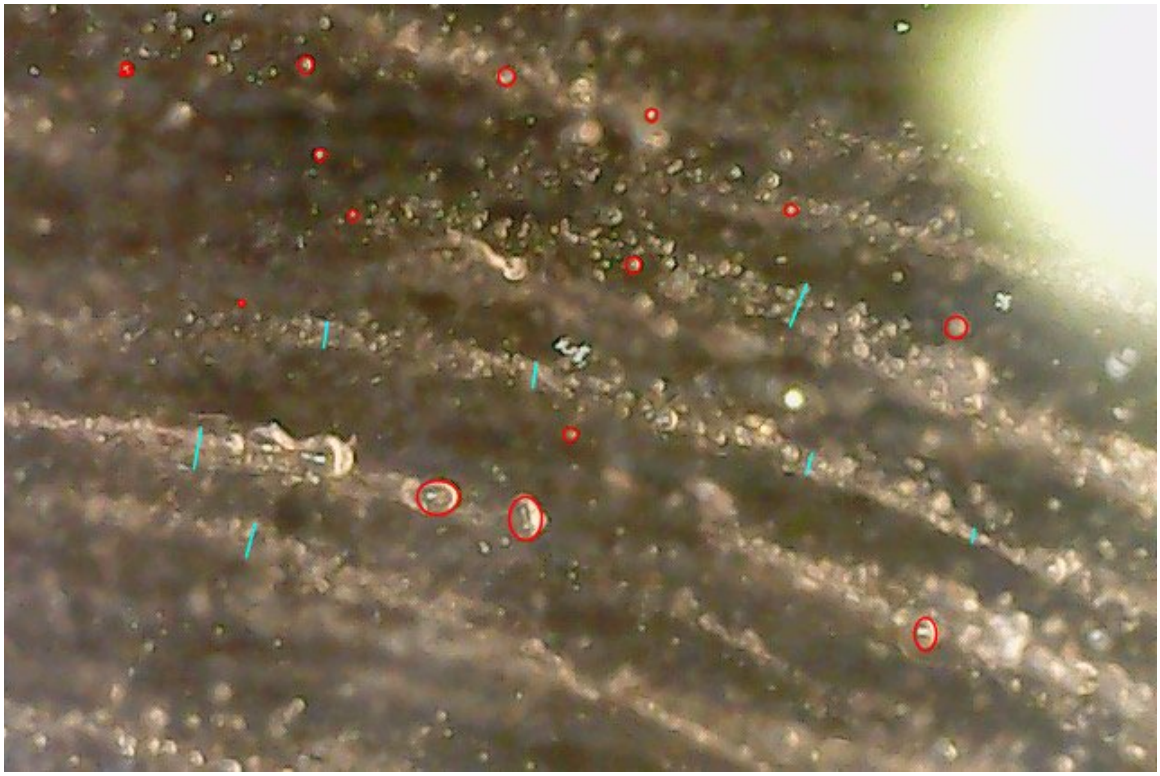

Figure 7.2: A measurement of the inclusions observed in a section of a 10 ppm NaCl icicle near the root. Downward is to the left. The inclusions vary significantly in size between 20 μm and 180 μm diameter. The crescents features, which appear as stripes of inclusions, at this scale have a typical width of 120 μm.

establish using dye in Section 7.2.1. Examining the inclusions in more detail, as in Figure 7.2, we find that the inclusions range in diameter between 20 μm and 180 μm. The crescent features are typically 120 μm in width, and are still present even at higher concentrations when the chevron bands form.

The inclusions most likely have a spherical shape because their contents never freeze completely due to the icicle being above the eutectic temperature (-21.1°C for H_2O + NaCl). They will continue to evolve into a spherical shape in equilibrium while the icicle freezes, and during the rise in temperature as the section is made by melting on the aluminum plate. Air bubbles would not undergo the same evolution.

If the cross-section is taken perpendicular to the icicle axis, as shown in Figure 7.3(c), the crescent formations of inclusions appear as rings tangential to the icicle surface, rather like the growth rings of a tree. These growth rings were observed by Knight [38].

The shapes of the crescents and chevrons in the longitudinal cross-sections clearly record important features of the growth process leading to the rippled exterior shape of

the icicle, including the upward migration of the ripples. We analyze the relationship between the pattern of inclusions and the shape in detail in Section 7.2.3. The approximate periodicity of the crescents, in particular, suggests that they are due to cyclic episodes of wetting and freezing, as we discuss in Section 7.3.

7.2.1 Content of inclusions

Using Sodium Fluorescein as a fluorescent impurity, we find that the dye is concentrated into the inclusions, as shown in Figure 7.3. The solid ice matrix is clear with no dye present. From this observation, we infer that the impurities are concentrated inside the inclusions. Because the icicle temperature is never below the eutectic temperature, the inclusions remain liquid.

Comparing the pattern of inclusions between fluorescein, NaCl and glucose at similar molal concentrations, we find that the inclusions are of similar size, shape and location. We conclude that the fogginess seen in rippled icicles is due primarily to scattering by inclusions — small pockets of liquid with higher concentrations of impurities — and not due to air bubbles. We conjecture that this will be true above the eutectic point for all species of dissolved impurities that cause constitutional undercooling.

We did not observe any air bubbles in any of our laboratory icicles. Air bubbles could only be discerned when a dye is used as the instability-triggering impurity. When fluorescein is used, there are so many dyed inclusions, that small non-fluorescent bubbles can not readily be seen. When the directional light source is added to the UV illumination, some inclusions exposed on the surface appear, but this is more likely a result from removal of liquid when the section is wiped than evidence of air bubbles. Maeno *et al.* observed oblong inclusions in the core of the icicle [40, 19], which could be air bubbles that emerge from the trapped liquid core (mode 3 growth in the nomenclature of Maeno *et al.* [19]). In our fluorescent dyed icicles, we observe a line of fluorescent inclusions along the central axis of the icicle where the liquid core freezes last. We discuss some possible differences between dissolved solids and gases in Section 7.3.

7.2.2 Na^+ concentration in the ice

The presence of impurities inside of icicles grown with NaCl was also confirmed using ion chromatography by optical emission spectroscopy (ICP-OES). The feed water,

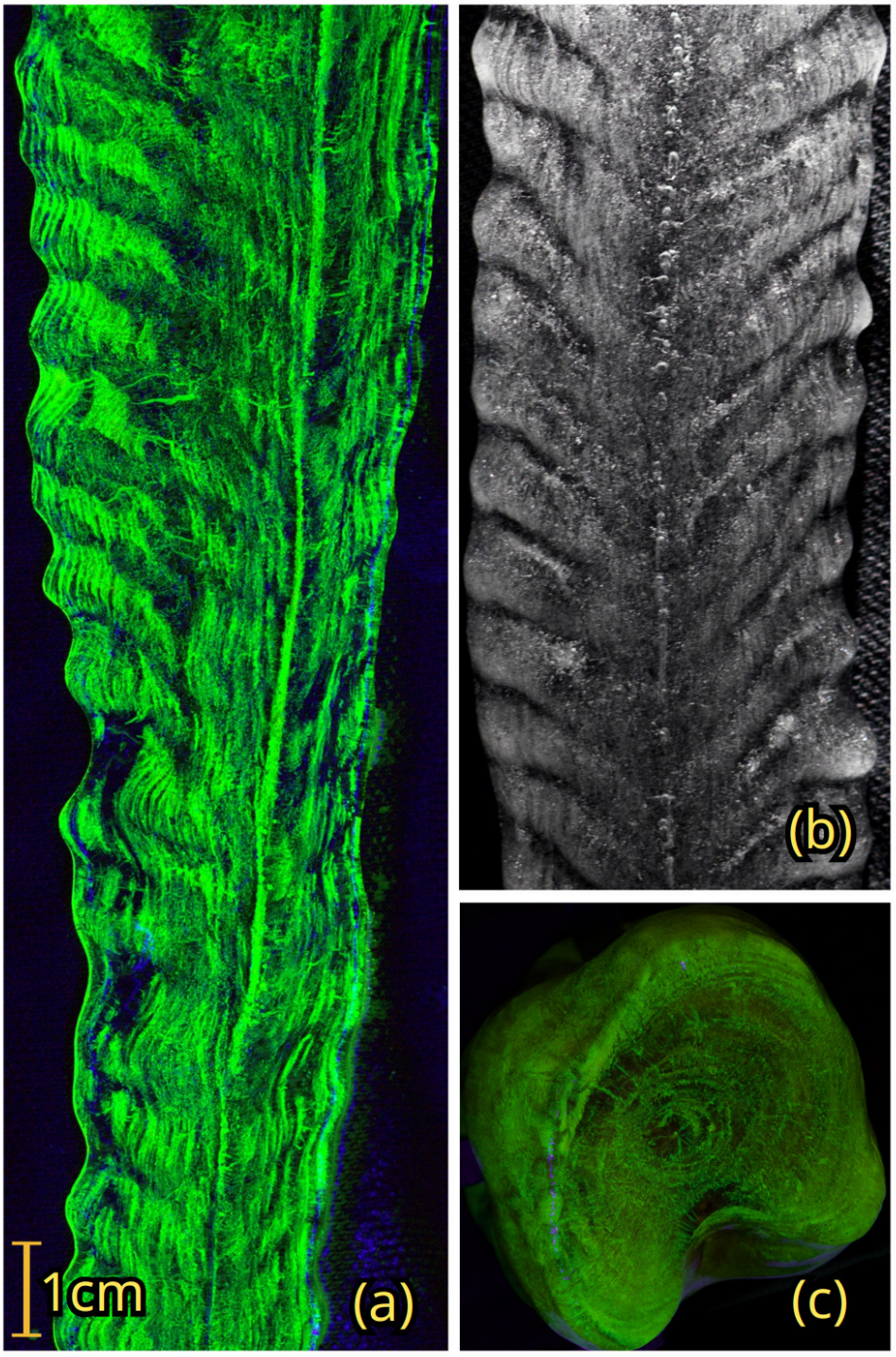

Figure 7.3: Using Sodium Fluorescein (a) at the same ionic concentration as used previously for NaCl, we observe that the inclusions glow under UV illumination. The pattern of inclusions qualitatively matches what is observed with (b) NaCl (and other chemical species). Some larger inclusions appear near the central line in (b) that may look like air bubbles, but the corresponding central line in (a) glows with dye. A cross-section perpendicular to the icicle axis (c) shows layers of inclusions that resemble the growth rings of a tree.

runoff and bulk in-ice concentration were measured for a series of icicles with ICP-OES [1]. The measured concentrations of Na^+ are presented in Figure 7.4.

The bulk concentration of Na+ that we observe is much higher than could be contained in single-phase ice. The segregation coefficient, k_0, which quantifies how much NaCl can be contained in ice at a given temperature, is essentially zero for ice Ih, meaning very little NaCl or other impurities can be contained in the solid ice. Instead, almost all of the impurities are sequestered into liquid inclusions. The ratio of bulk ice (including inclusions) and feed water concentrations was found to be nearly constant at 0.27 ± 0.05 over the whole range of concentrations, with only a very slight increasing trend. This value is remarkably close to the *effective solute distribution coefficient* $k^* = 0.26$ extrapolated by Weeks and Lofgren [75]. In their experiment, Weeks and Lofgren used much higher concentrations from 1% to 3.3% NaCl. The value k^* is the effective value of k_0 if the ice remains mixed-phase for a slowly advancing ice front.

We did not find a saturation of the bulk ice concentration at high concentration, as might have been expected. Instead, the bulk ice concentration increases linearly, so the amount of liquid contained in the ice matrix must also increase linearly with feed water concentration, even as the icicle becomes crowded with liquid inclusions. It is possible that there is a saturation point above the highest measured concentration of 640 ppm NaCl. Sea water, for example, is known to form icicles [14], but has a far higher NaCl concentration of about 35 000 ppm.

7.2.3 Connection between inclusions and rippled topography

Examining Figure 7.1, it is obvious to the eye that the bands of impurities inside the icicle are closely lined up with the exterior ripples. The peaked shapes of the crescent structures match up with the shapes of the ripple peaks, and the lines of pure ice align with the valleys between peaks. Using time-lapse images taken during the icicle growth, we can follow the time evolution of the topography and correlate it with a cross sectional image of the final distribution of inclusions. Figure 7.5 illustrates this close correspondence.

It is frequently observed that ripples exhibit wavelength selection effects during their evolution: ripples crowd one another causing ripples to disappear, or ripples

[1] Thermo Scientific iCAP Pro ICP OES at the Analytical Laboratory for Environmental Science Research and Training (ANALEST), Department of Chemistry, University of Toronto.

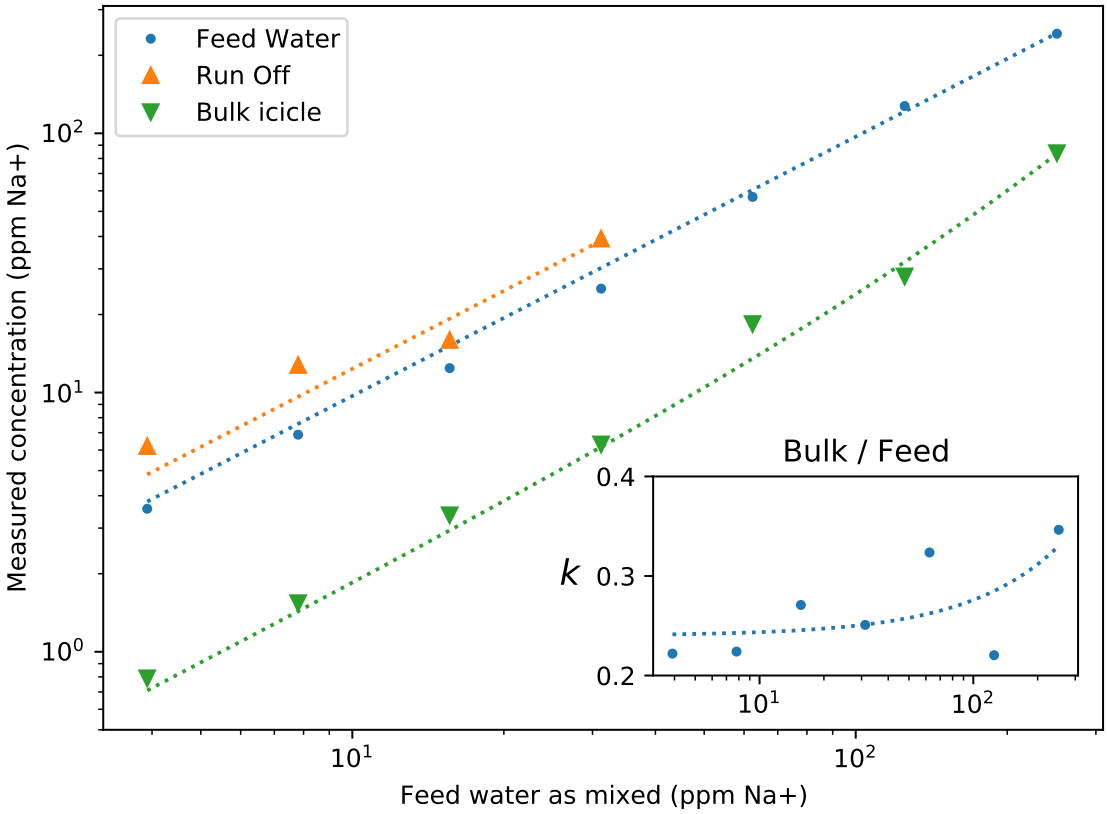

Figure 7.4: Na^+ concentrations in the feed water, in runoff water, and in cross sections for a series of NaCl icicles, measured with ICP-OES. The feed water concentration agrees with what is expected from the amount of NaCl added. The runoff water shows only a slightly increased concentration over the feed water. The ratio of concentration in the bulk to that of the feed water is nearly constant at 0.27 ± 0.05 , but may increase slightly at higher concentrations. The inset shows this ratio. The dotted line in the inset is the fit $0.05 \log_{10}(c) + 0.19$.

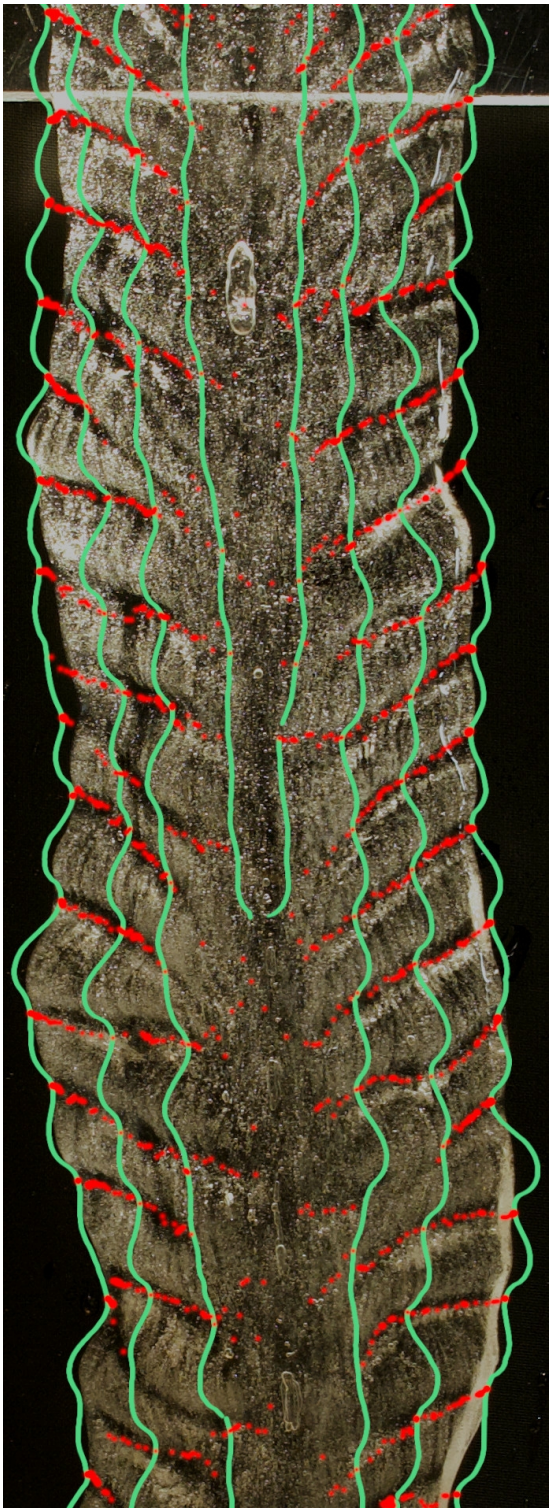

Figure 7.5: An overlay of a cross sectional image with the edge-detected surface shape taken every 10 rotations shows that the bands of inclusions and crescent shapes closely aligns with the topography. The valleys between the ripples, highlighted in red, match up well with the lines of pure ice seen in the cross section.

split, causing new ripples to appear between two existing ripples. These processes can be seen in Figure 5.9, which shows the topography with peak tracking. Similar ripple creation and destruction events are traced out by bands of inclusions in cross sectional images, as in Figs. 7.1 and 7.7. These effects are most pronounced at the highest concentrations, when the icicle is densely filled with liquid inclusions.

In Secs. 7.2.4 and 7.2.5 below, we quantitatively compare the chevron pattern of inclusions to the rippled topography through their wavelengths and the migration of ripples up the icicle.

7.2.4 Ripple wavelengths

An estimate of the chevron band wavelength can be obtained from cross sectional images. Longitudinal cross sections were analyzed using ImageJ [74]. The lines of pure ice between bands of inclusions were traced by hand, and the distances between adjacent lines were measured. The average of the distance measurements was taken to be the wavelength. In practice, this rather manual procedure was limited to a "well behaved" concentration range where it was possible to easily distinguish and annotate the pure ice regions. Below about 7 ppm NaCl, coherent bands do not form, so annotations are unreliable, while above 500 ppm NaCl the ice is saturated with inclusions, so distinct chevron bands can no longer be picked out by eye. A sample measurement of the band wavelengths from cross sections in the well behaved region is shown in Figure 7.7.

In order to have a direct comparison, the topographic wavelengths were also find found for the set of 52 icicles considered in this chapter. The topographic ripple wavelengths were determined using the same statistical approach described in Section 4.3.1. The full results for both the chevron bands and ripples are shown in Figure 7.6.

We found the wavelength of the chevron band features to be 8.54 ± 0.66 mm for the 25 measured cross-sections in the well behaved concentration range. As expected, the wavelength of the bands of inclusions (see Table 5.1) agrees with the wavelength derived from the topography. Both agree with the earlier estimate of 9.0 mm by Maeno *et al.* [19] and are slightly smaller than the Fourier value of 10.4 ± 0.8 mm for the topography found by Chen *et al.* [12].

There is a slight trend toward longer wavelength at higher concentrations seen in the cross section measurements, which was also observed by Chen *et al.* [12], but it is not significant given our number of measurements, and not reflected in the

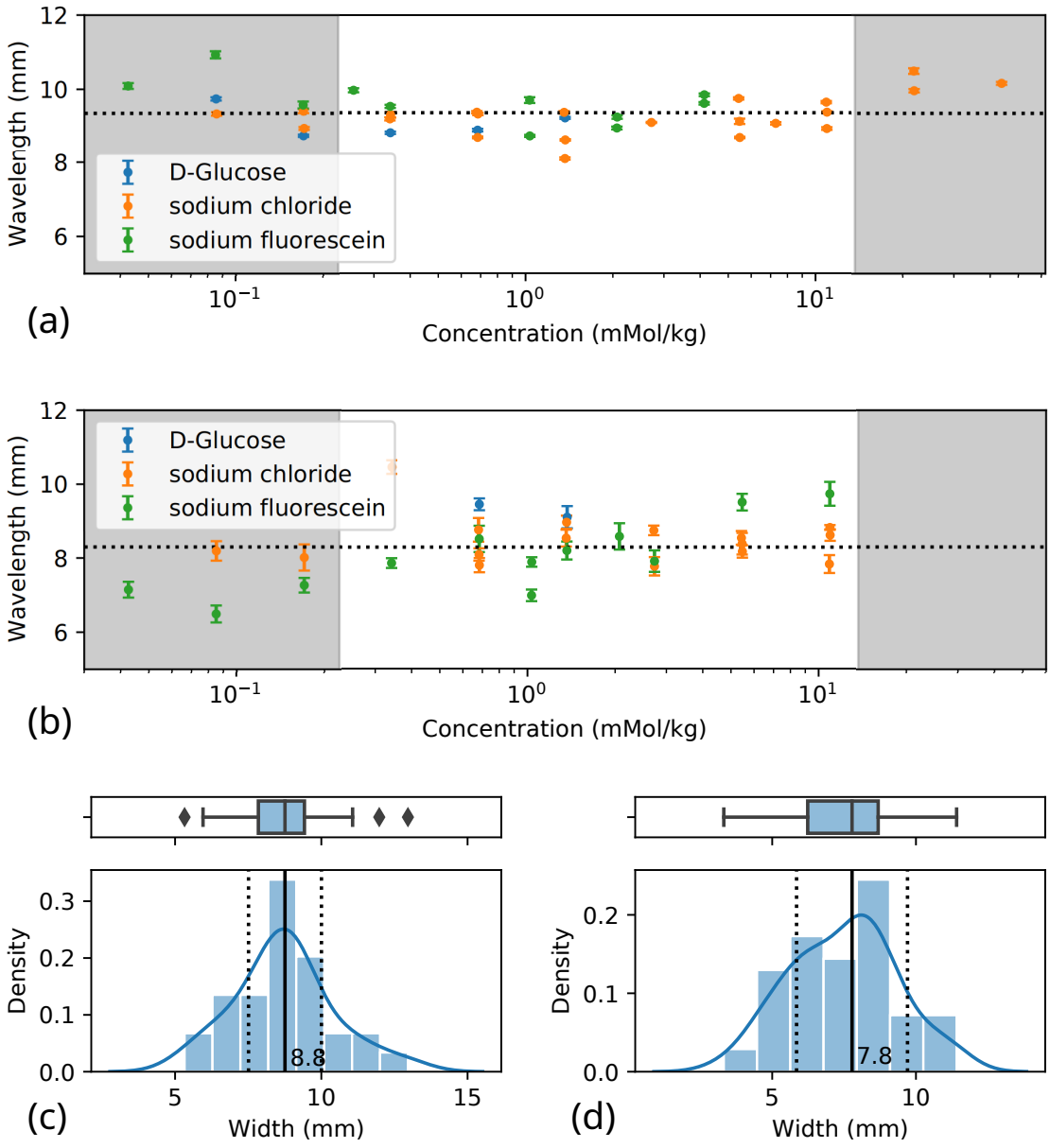

Figure 7.6: Ripple wavelengths of icicles as measured from the (a) topography, and (b) cross-sections. Grey regions indicate concentrations where ripples are not "well-behaved" — not forming at low concentrations, or exhibiting uncontrolled dynamics at higher concentrations, when the interior is fully saturated with inclusions. The error bars indicate the *standard error of the mean* for each wavelength measurement. Sample distributions of individual ripple widths shown for (c) a single edge, and (d) one cross-section. Both distributions are for icicles with 80 ppm NaCl.

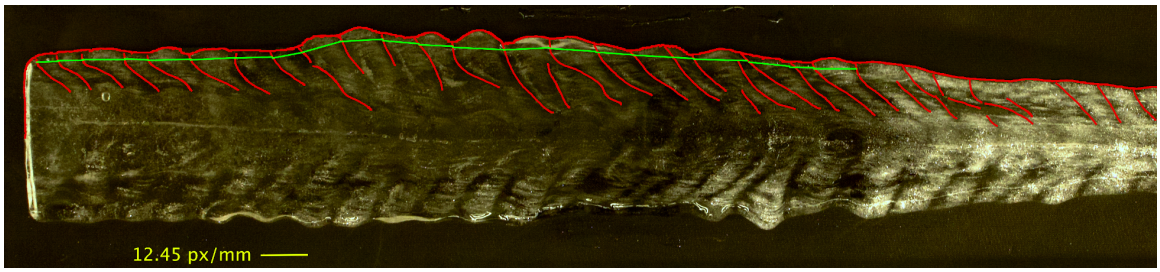

Figure 7.7: An example of measuring an icicle cross section. The icicle is illuminated with a unidirectional light source to the right. The pure ice that separates bands of impurities are highlighted with red lines. The feature-widths (green lines) are measured by the distance between each band of inclusions. The distribution of widths can then be used to find the mean and variance of band-to-band distances.

wavelengths measured from the topography during growth. In the topography and in Chen's measurements, the increase in wavelength is observed above the inclusion saturation point of about 500 ppm NaCl.

7.2.5 Migration of the ripple peaks

In Figure 7.5, it is clear that the bands of inclusions closely coincide with the topography throughout the growth of the icicle, and the upward tilt of the chevron bands tracks the motion of the rippled topography. In order to quantify this effect, we compared the slope of the chevron bands to the positions of the ripple peaks over time.

It is only possible to determine the angles made by chevron bands in cross sections taken at intermediate concentrations, for which clear, well behaved bands are traceable. Using the same traced lines of pure ice shown in an example in Figure 7.7, the typical angle of of the chevron bands was found to be $58 \pm 2.8°$ to the icicle axis. Above 160 ppm NaCl, we observed much higher angle variability within each icicle. Below 160 ppm NaCl, the standard deviation was typically 10°, while above 160 ppm NaCl it could be as high as 35°. Thus, the speed of migration of the ripples becomes more variable well before the icicle becomes saturated with inclusions.

By tracking the peaks in the topography as in Figure 5.9, we can extract the position of the peak relative to the icicle axis at each point in time. Fitting a line to those measurements gives a typical angle of $56 \pm 2°$ to the icicle axis, which is consistent with the angle made by the chevron bands seen in the cross-section.

In icicles a higher concentrations that are saturated with liquid inclusions, we no

longer observe lines of pure ice in the cross sections. This occurs at a concentration where Chen *et al.* [12] found the direction of ripple migration became more unpredictable and was often downwards. When we track the peaks in the topography, we observe the same unpredictable ripple migration at these concentrations. Ripple migration on saturated icicles is much more dynamic than at lower concentration: peaks may split, consume neighbors, or spontaneously form in valleys, as shown in Figure 5.9(c).

We propose in Section 7.3 that the direction of peak migration may be understood to be a consequence of the distribution of surface liquid on icicles.

7.2.6 Crystal grain structure

We used the same cross sectioning technique to examine the crystal structure of icicle sections at various concentrations. A selection of icicles viewed with cross-polarized filters are shown in Figure 7.8. We found two consistent features in the grain structure of laboratory-grown icicles. First, the core of the icicle near its axis was one long continuous crystallite. There is generally a single crystal with its c-axis perpendicular to the icicle axis down the core, where the central column of liquid water freezes last. Secondly, outside the core, the crystallites near the root of the icicle are smaller than those lower down the icicle. The smaller crystallites near the root could be caused by the more rapid flow conditions encouraging more nucleation sites.

These two observations are consistent with what Laudise *et al.* reported for natural icicles [37], although their sample of natural icicles showed much more variety, which is likely due to the uncontrolled growth conditions. Laudise *et al.* also found that the slower growing c-axis was never parallel to the icicle axis and that it was often nearly perpendicular. In general, outside the core, the crystal orientations of the crystallites are rather random.

A third feature that was less consistent for rippled icicles was that the crystallites and grain boundaries outside the core were sometimes oriented with an upward bias, in a pattern similar to the chevron bands of impurities. These features are visible in Figure 7.8(a,b). The grain boundaries were somewhat more likely to coincide with the lines of *pure ice*, with the trapped impurities clearly visible within the crystallites, not at the grain boundaries. Non-rippled icicles do not exhibit an upward bias in their grain shape. Instead, their grain boundaries are mostly perpendicular to the icicle axis, as in Figure 7.8(c).

The correlation between the ripples and the grain structure is not strong, however. Often a crystallite will span multiple ripples, as in Figure 7.8(d), or the there will be many small grains within a ripple, with only a barely discernible tendency towards a chevron-like pattern.

Our lab-grown icicles show the same ripples as natural icicles with the advantage of being able to control the water source and growing conditions. We have shown that the inclusions are primarily pockets of highly concentrated liquid trapped inside of crystallites. These inclusions form a record of the icicle growth — both of the formation of the rippled morphology, and of the cyclic wetting/freezing process.

7.3 Discussion

In this Section, we situate our observations in the context of previous work, and discuss how the inclusion patterns in the interior of an icicle may be related to previous observations of the flow pattern of liquid at the surface during growth reported in Chapter 6.

Although foggy, rippled natural icicles are commonplace, there have been relatively few published descriptions of their internal structure. Knight [38] observed sponginess and what he called "air bubbles" in icicles that have a "wrinkled" (*i.e.* rippled) appearance, and observed rings of inclusions in *transverse* cross sections. Maeno *et al.* [18, 19] observed foggy features inside of icicles coinciding with the ripples on the surface in a longitudinal cross section of an icicle collected in Sapporo during the winter in 1984, and likewise attributed the features to air bubbles. Both these studies were made before the crucial connection between ripples and impurities became clear in laboratory experiments [12].

Under the assumption that the inclusions were air bubbles, Knight thought that the spongy ice was primarily due to draining of liquid, while Maeno *et al.* suggested that "air bubbles" were evidence of rapid crystal growth. In addition, Maeno *et al.* assumed that the whole surface was wetted, so ripples would have to be from more rapid cooling at the protuberances. This explanation led to models of icicle morphology [44, 11] and linear stability theories of icicle ripples [25, 26, 27, 28, 30, 31, 29] which assumed that the icicle is completely covered by a thin flowing film of supercooled water. Subsequent experimental work [1] has shown that this is not the case and that the water actually flows over the surface in a complex pattern of transient rivulets.

Our observation that the inclusions are pockets of liquid indicates that a different

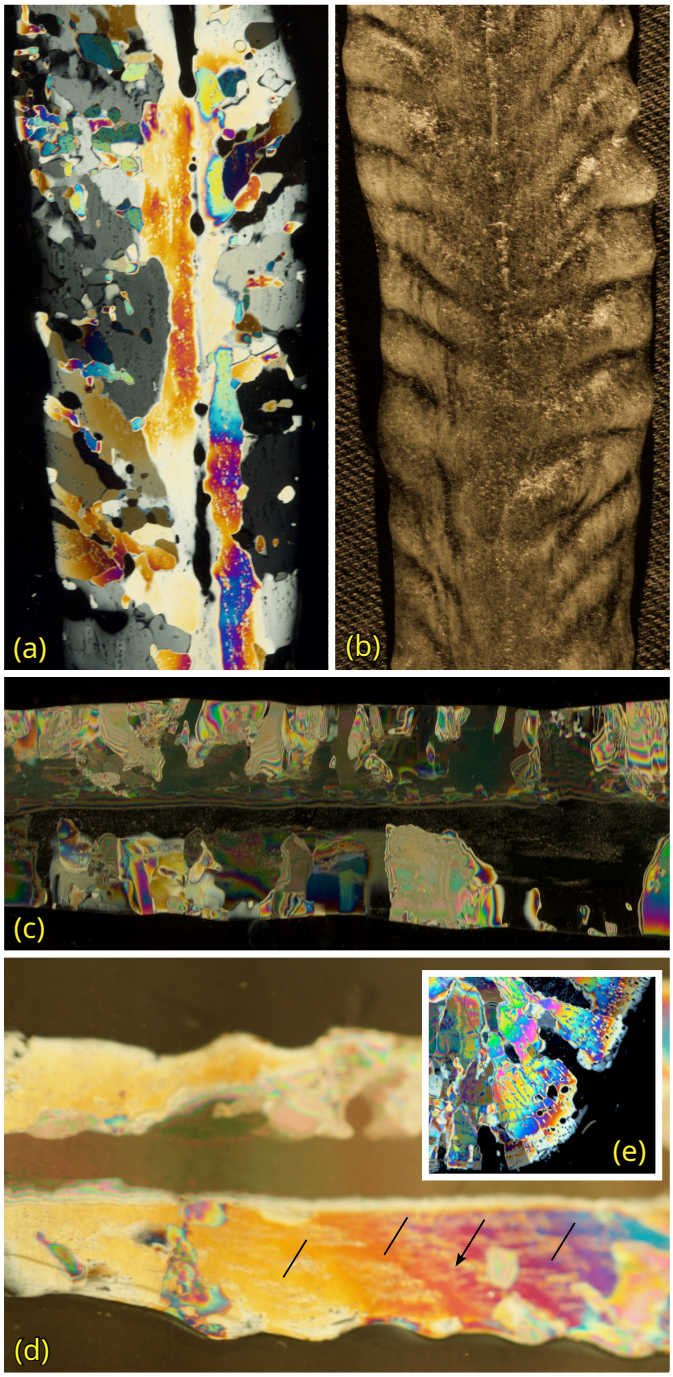

Figure 7.8: Images of icicle cross sections between crossed polarisers. The upward angle of grains in a rippled icicle (80 ppm NaCl) can be seen in (a), with its corresponding non-polarized view in (b). When an icicle is grown with a low impurity concentration (20 ppm NaCl) no ripples form (c), and the grains do not exhibit an upward angle. The liquid inclusions are apparent in (d) (40 ppm NaCl), which is also an example of a crystallite spanning multiple ripples. Arrows in (d) point to individual bands of inclusions seen within the single crystallite. The inset (e) shows grains with internal inclusions in an axial cross-section.

process is involved in ripply icicle formation. The foggy, spongy ice is not due to draining of liquid from spongy ice, but actually the trapping of impure liquid. Thus, the inclusions are *not* evidence of rapid crystal growth, and may not be used to infer rapid cooling at protuberances.

While dissolved solids remain trapped in the liquid inclusions, dissolved gasses can escape to the atmosphere. For gasses to be trapped as bubbles, there would indeed have to be very rapid cooling, or some process that entrains and traps bubbles as the ice forms. Such a trapping process does occur in the core of the icicle, where the water can remain liquid well away from the tip, forming a long hollow region. This core water only freezes later by a sort of pipe-filling process, called mode 3 by Maeno *et al.* [19]. The shapes of bubbles formed during this process were observed by Maeno *et al.* However, we have observed using dye that liquid inclusions may still form in the core. Most of the body of an icicle is formed from liquid flowing and pooling on the outer surface of the icicle [1], where it is presumably in sufficient contact with the surrounding air that dissolved gases can escape before bubbles are formed.

We suggest that the location and trapping of impurities can best be understood by taking into account the way liquid flows and is otherwise deposited on the surface of an icicle. Previous experiments [1], which studied this process in detail, have shown that the flow proceeds by a series of intermittent rivulets accompanied by areas of stagnant surface wetting, rather than completely ensheathing the icicle. The nature of these flows is strongly dependent on the concentration of impurities, which change the wetting properties of the surface. It was observed directly that the liquid tends to reside preferentially on the upper surface of a ripple peak [1]. The wetting of an icicle is highly intermittent, which indicates a cyclic wetting/freezing process, as Knight suggested when he observed rings of inclusions in his transverse cross-sections.

The layering of the inclusions into the crescent structures may be interpreted as evidence of an iterated wetting/freezing process in the following way. The liquid that remains on the surface after a rivulet has passed is confined to a small wetted region. When that liquid is first deposited, it has the low initial concentration of the feed water, and pure ice can form unimpeded. Rejection of the impurities from the ice surface into the small volume of surface water would cause a rise in concentration in the liquid. Mushy ice [16, 49] can then start to form, trapping some impurities as inclusions while the remaining impurities continue to build up in the surface liquid. The next rivulet of liquid would then wash away or dilute the concentrated liquid, leaving a deposit with a lower concentration again. The freezing process can then repeat, forming a stack of crescent-shaped mixed-phase ice and pure ice, which organize

into bands of impurities matching the rippled topography of the icicle.

The lines of pure ice that we observe in the cross sections are collocated with the mostly unwetted regions on the ice surface, while the areas with the most inclusions collocate with the areas that are wetted with surface liquid for the largest fraction of the time. In addition, the surface wetting and rivulet flow process is modified by the presence of impurities in such a way that even for constant overall flow rate, much more surface water is present at higher concentrations [1].

The rather low feed water concentration is far below the threshold for a mushy layer to form. However, because the liquid is confined on the surface, as it freezes, the concentration will rise above the critical concentration, and thus a mushy layer can form in a transient way. The confinement of impurities allows the value of $k^* = 0.26$ to be reached, which would normally not be possible for such low concentrations with a larger volume or flux of source water. All of these ice deposition effects conspire to cause a concentration-dependent rippling instability that corrugates the icicle topography into a pattern of ripples with a near universal wavelength. Obviously, there is much that we do not understand about the exact nature of this instability.

We also examined the crystal grain structure, because of anecdotal suggestions [41] that grain orientations may be connected to ripple growth. For example, Knight [38] observed that a knife blade could be inserted into the hollows of a ripply icicle, implying that the spongy parts were in the hollows. That simple observation led Knight to suggest that the preferred crystal orientation would have the c-axis parallel to the icicle axis. The liquid could then drain from between the basal sheets leading to trapped air bubbles. When we tried to perform the same knife blade observation on finished icicles, we found that, contrary to Knight, we could not insert a knife blade into the hollows, and that in fact the ice was mushiest near the peaks of the ripples. Knight acknowledged that previous work [37] had found that the c-axis was never parallel to the icicle axis. We hope that our observations help to clarify the relationship between mushy regions, crystal orientations and ripples.

The traces of the ripple pattern that we observe in the crystal grain structure might also be interpreted as an effect of the surface liquid dynamics. The observed incommensurability of the grain structure with the ripple topography shows that the ripples and their migration are not caused by the crystal orientation setting a preferred growth direction. Instead, we suggest that the growth of the ripples from the corresponding liquid deposits restrict the growth of the grains.

The large uninterrupted crystal can form in the core of the icicle, because the outside of the tip is always coated and its core is filled with liquid, which permits a

slow, steady growth. The smaller grains near the top of the icicle are likely linked to the rapid change in temperature and/or flow in that region, which causes more rapid freezing. These inlet effects would be peculiar to our icicle machine, which is why the natural icicles observed by Laudise *et al.* [37] had much more variety in their grain structure.

The slight upward bias in the grain shape could be due to the liquid deposits being preferentially found on the top side of ripple peaks. If a new crystal nucleates on the top of a ripple peak, it has access to a large pool of water to steadily grow, whereas the "dry" area on the underside creates a barrier that limits grain growth downwards. Of course, all these effects are highly stochastic so that only a rather weak correlations between the ripples and crystal structure are observed.

Chapter 8

Conclusions

We have shown through theory and experiment that the mechanisms of ripple formation are much more complex than previously thought. A linear stability analysis of the extension of Ueno's model of ripple formation in Chapter 2 showed that it cannot accurately predict ripple formation in fresh-water icicles. Through a series of experiments growing icicles in the laboratory, we established a deep connection between the stochastic flow of water on the surface of icicles, and pockets of brine trapped inside the ice, to the rippled morphology of icicles grown with impurities. These processes are all mediated by the concentration of impurities in the source water. By growing icicles with various species of impurities, we showed that the change to icicle morphology caused by impurities is a colligative phenomenon.

There is a gap of knowledge in wet ice growth between pure water icing, and seawater icing. As seen in Chapter 5.2, the morphology of wet ice growth responds differently to lower concentrations of impurities than seawater concentrations. The morphology of pure water icing is obviously different due to the lack of ripples. The observations of the wetting dynamics and inclusions on the surface of icicles bring new insights into wet ice growth. The distribution of liquid on actively growing wet ice is thicker and covers more of the surface when greater amounts of impurities are present. This leads to faster lateral growth. The impure inclusions arranged in bands inside of icicles are evidence of local areas of cellular or dendritic growth, and align with the rippled morphology. At concentrations above 0.4 ppt NaCl, the icicle interior is completely filled with brine inclusions, becoming mushy and more fragile.

In the following sections, we discuss the results of the linear stability theory and experiments, and how they relate to each other. The findings in this thesis reveal novel mechanisms involved icicle formation that can be used in models of wet ice growth. A potential model of wet ice growth is described in Section 8.5, along with

some suggestions for future experiments that could provide a more detailed view of the cyclic wetting and freezing on icicles.

8.1 Thin-film theory

We extended the Ueno thin-film model in Chapter 2 to include effects from impurities in the source water. In particular, constitutional undercooling couples the temperature and concentration fields at the ice surface. Performing a linear stability analysis on this generalized model showed that it cannot accurately predict icicle ripple formation. The ice surface is unstable for all wavelengths, and the dispersion relation is insensitive to changes in source water concentration. The insensitivity to concentration is due to the weakness of the coupling introduced by constitutional undercooling, even when accumulation of impurities magnifies the concentration perturbations. The surface tension of water was also found to have a greater effect on the stability of the model than any other parameter, placing the model in further conflict with the experimental observations of Chen and Morris [12, 20].

Stability analysis of the generalized thin-film model requires some troublesome assumptions. Perhaps the greatest is that the flow of the liquid film is stable. Another notable approximation is to neglect accumulation of impurities, and consumption of water down the length of an icicle. Using linear stability analysis, the accumulation can be incorporated to some extent, and the terms associated with it are small. Bertagni notes that the x-dependence introduced by accumulation of impurities prevents a weakly nonlinear stability analysis of impure icicles through gradient expansion [47]. Without accounting for accumulation of impurities, the concentration cannot contribute to the weakly nonlinear problem.

Even worse, the failure of the thin-film model is not simply due to simplifications used in the analysis. The fundamental assumption that a uniform thin-film flow covers the icicle in no way resembles the actual distribution observed in Chapter 6. The failure of the thin-film model with impurities and the observations of the surface liquid suggests another approach must be used to understand the formation of ripples on icicles. The observations of surface liquid and patterns of inclusions inside icicles provide new insight into possible mechanisms in ripple formation.

8.2 Morphology

Our study of the morphology of icicles extended the work of Chen and Morris by considering more chemical species for the ripple triggering impurity in Chapter 5. Perhaps the most important conclusion to this experiment is that the morphology of icicles was not affected by the chemical species used, regardless of ionic charge or molecular weight. Icicles grown with different impurities were shown to have similar morphologies, as long as they were grown from the same molar concentration, so changes to icicle morphology due to impurities in the source water is a colligative phenomenon.

The distribution of water on an icicle's surface plays no role in the conclusions of the morphological models proposed by Makkonen [11] or Chung and Lozowski [14], but a uniform coating of liquid is a fundamental assumption of the models for the rippled morphology. Because of that, the radius and length of lab grown icicles are in reasonable agreement with Makkonen's model, but the ripple amplitude and wavelength do not agree with the models of either Ogawa *et al.* [25] or Ueno *et al.* [26, 27, 28, 29, 30, 31, 32].

Another curious observation was that wet ice accretion from water with concentrations below 10 ppt NaCl (34 mMol/kg) exhibits different morphological trends with concentration than marine icicles. In particular, the elongation and radial growth rates both increase with concentration in this range. The Chung/Lozowski model [14] for saline icicles always predicts a decrease in elongation rate with increasing concentration, because it depends on the accumulation of salt down the length of an icicle. Thus Chen's observations [20], and those presented in Chapter 5.2 behave opposite of Chung's model for low-salinity icicles. Another mechanism is likely involved for low-salinity icicles.

It is possible that the surface water distribution provides an explanation for the global morphology. When interpreted through Makkonen's model [11], our observations of increased radial growth and elongation rates indicate a reduction in water flux over the surface of the icicle, particularly above the icicle tip. This aligns with the surface water retention discussed in Chapter 6: when water is retained on the surface, there is necessarily a lower water flux, and more water is retained at higher concentrations. The largest change in water retention occurs higher on the icicle surface, while water near the tip is retained at all concentrations.

Our observations of the rippled morphology are consistent with Chen's previous experiment [12]. The relatively low variation in ripple wavelength indicates that

none of the temperature, flow-rate, or concentration affect the ripple wavelength. The ripple amplitude is also seen to increase with concentration, and shows negligible dependence on either temperature or flow rate. None of these observations are directly explained by the existing theories.

8.3 Surface liquid

We have shown through experiment that the flow of liquid over icicles is a much more dynamic and stochastic process than was previously thought. In particular, we uncovered the effect that small levels of impurities have on the wetting properties of the ice surface. These observations, reported in Chapter 6, include the fact that icicles are never fully ensheathed in a liquid film, except at a short region near the tip. Instead, the water descends the icicle in rivulets, with preference to areas where liquid water is still present on the surface. In general, impurities cause the ice surface to retain more water, and to change the overall pattern of flow toward wider rivulets and more discrete patches of liquid.

The often non-uniform flow of water was acknowledged in a few observational papers [19, 14, 39]. For example, Geer, Maeno, Chung *et al.* noted that the water could be seen to descend in preferred paths down the icicle surface, but this behaviour was not studied in detail, and morphological models ignored the complicated flow. We performed the first detailed study of liquid flow on icicles using fluorescent dye [1], as reported in Chapter 6. In icicles grown from impure water, the distribution of liquid on the surface closely matches the growth of the rippled topography, preferring to sit on the upper surface of the ripples. Gravity has a strong influence on the distribution, but the surface properties of the ice also play a role.

Using cylindrical ice substrates for wet ice growth, it was shown that the amount of liquid retained was increased with both the addition of salt (Sodium Fluorescein) to the cylinder surface and roughening the cylinder with emery cloth. The increased liquid coverage from these surface modifications also led to ripple formation in the early stages of wet ice accretion. The most drastic change in morphology was seen on a truncated cylinder. Liquid flowed quickly over the ice cylinder, and a conventional icicle formed at its tip, which had high water retention. The radial growth of the icicle at the tip was faster than the radial growth of the cylinder, and the icicle's radius quickly became larger. The ripples that formed on the icicle were significantly larger than on the cylinder, and began to propagate up the cylinder of ice.

The observations of the distribution of liquid on the icicle surface in Chapter 6

suggest a different mechanism of ripple formation. There is a feed-back loop in which deposits of impure water attract and retain more of the liquid that flows over the surface. The truncated cylinder shows a striking contrast in the flow and freezing dynamics between the surface of actively growing ice, and a fully frozen ice surface.

8.4 Inclusions

We conducted the most complete analysis to date of the foggy patterns of inclusions in the interior of icicles and their connection to ripples on the surface. The observations in Chapter 7 show that the inclusions are not air bubbles, but are actually pockets of liquid water with high concentrations of impurities. The inclusions in the ice are organized into chevron bands, with crescent shaped substructures that match the growth and migration of ripples on the surface. The impurities trapped in the ice do not coincide with crystal grain boundaries, but the orientation and shape of the grains are slightly influenced by the growth mechanisms of the ripples.

The location and pattern of trapped impurities records the complex dynamics of the liquid on the surface of an icicle during growth. The inclusions collect in layered crescents, reflecting the intermittent wetting and freezing of liquid on the surface. Higher concentrations of liquid are achieved through the stagnation of liquid on the surface. This liquid tends to linger on the upper surface of ripples, where the highest concentration of impurities is trapped in the ice.

The pattern of inclusions can be understood through the surface wetting observed in Chapter 6. As the pools of liquid freeze, the concentration of impurities increases to the point that dendritic growth occurs. This dendritic forms a thin mushy layer, trapping the impurities inside the icicle. Because the pools of liquid tend to sit on the upper side of the ripples, the trapped impurities are concentrated around the peaks of the ripples.

The amount of inclusions were seen to increase with source water concentration, eventually filling the entire icicle at concentrations above 400 ppm NaCl, the same critical concentration above which migration of ripples becomes much more dynamic and unpredictable. The lines of pure ice between the bands of inclusions have a controlling effect on the ripple migration. We propose that the control is through the surface liquid distribution: the pure planar ice exposed on the surface holds little to no water, and isolates the patches of liquid. Water is not able to flow between the patches of liquid, so they freeze in a more predictable manner.

8.5 Future Work

Rather than continue with a thin-film model, we propose the development of a stochastic model of icicle growth based on cyclic wetting and freezing as illustrated in Figure 8.1. Such a model would need to include the effects of impurities on the dynamic wetting of ice described in Chapter 6. The wetting is affected by impurities on the ice surface, patches of dendritic ice, and the existing distribution of liquid water on the surface. After each rivulet of water flows over the surface, more water is deposited on the upper surface of ripples. These pools of water gradually freeze, first with planar ice growth, then with dendritic growth as the concentration increases. The remaining pools of water and exposed dendritic ice will retain more water when rivulet of water flows over the surface.

We note that the stochastic computational model by Lozowski *et al.* has produced ripples on marine icicles [17]. That computational model repeatedly simulates droplets impinging and flowing on the ice surface driven by gravity, but does not include the differential wetting that we observed in Chapter 6.

The proposed cyclic wetting and freezing model explains the long-term growth of ripples, but does not explain the initial emergence. In consideration of the trapped pockets of impurities established in Chapter 7, it would be reasonable to extend the thin-film model further using mushy layer theory [49]. A thin-film theory with mushy ice may still explain the initial emergence of ripples near the tip of the icicle, where it is entirely covered in liquid. Including a mushy layer should increase the role of impurities, and reduce the problem of impurity accumulation down the length of the liquid film. There are potential problems with this approach: the range of concentrations observed in fresh water icicles are much less than what is commonly accepted as necessary to form a mushy layer. The low concentration might be enough to form a mushy layer due to the direction of latent heat transport through the film to the air, and also the thinness of the liquid film.

Our study of inclusions of impurities inside of icicles in Chapter 7 shows that they are intrinsically connected to the rippled morphology. We hypothesized that the inclusions form when the water confined on the surface gradually freezes, increasing the concentration above the critical value for the constitutional undercooling instability, causing cellular ice growth. However, we were unable to see dendritic growth directly during icicle growth, because it is at a much smaller length and time scale than observed in our experiments. Future experiments could validate that hypothesis. As an example, one could record the freezing process of a drop of water dyed with

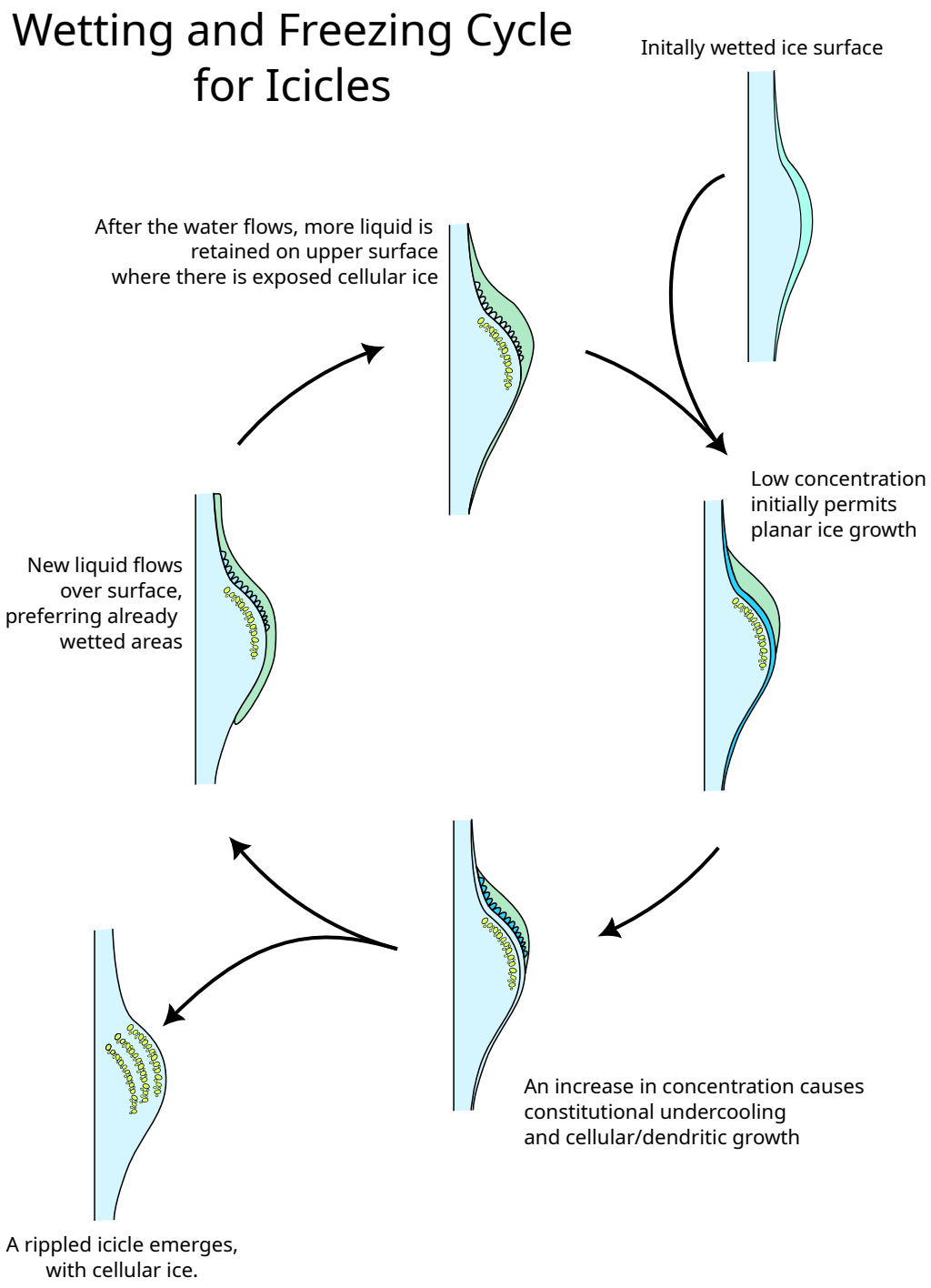

Figure 8.1: The proposed cyclic wetting and freezing mechanism of icicle growth with impurities. The positive feedback between the surface liquid distribution and exposed cellular ice leads to ripple formation.

fluorescein with microscopy. We expect that the initial layer of ice would be pure, and subsequent layers would form mixed-phase cellular or dendritic ice. Monier *et al.* performed a similar experiment using a steady flow of water dyed with Fluorescein [68], but the constant flow prevents an increase in concentration. That experiment could be modified to use an intermittent flow, which would allow for a local increase in concentration, and by extension cellular ice.

Appendix A

Physical model details

As discussed in Chapter 2, the thin-film model we used for ripple-growth is an extension of the model proposed by Ogawa and Furukawa [25], which was later modified and analyzed by Ueno *et al.* [26, 27, 28, 29, 30, 31, 32]. We extended the model to include effects of impurities, and physically accurate thermal boundary conditions as described by Neufeld [46].

The derivation of the thin-film model of icicles with impurities is outlined below. A non-dimensionalization of the model is derived in Appendix B, and a summarized in Chapter 2.2.

A.1 The icicle domain

According to Maeno's explanation of icicle growth [40], and Makkonen's model [11], the icicle grows in radius through a film of water on its exterior surface. While it has been noted that water tends to descend in rivulets along preferred paths [14, 39, 19, 1], the common assumption is that liquid water flows in a uniform layer around whole circumference. This assumption greatly simplifies the model of icicle growth.

The uniform film provides axial symmetry, so that a 2-dimensional slice can be considered instead of the fully 3-dimensional problem. If the radius of the conical icicle is sufficiently large compared to the film thickness, azimuthal effects can be neglected, and the thin-film can be modelled accurately in a Cartesian plane.

As shown in Figure 2.1, we use coordinates with x in the direction down the length of the icicle, and y pointing out from the ice surface. The thin film's boundaries are the ice at $y = \eta(x,t)$, and the air at $y = \xi(x,t)$. The model is derived in a fixed reference frame, so η and ξ are moving boundaries. Using a fixed reference frame simplifies the application of conservation laws for the boundary conditions. A refer-

ence frame moving with the ice wall will be adopted for the non-dimensionalization in Appendix B.

A.2 Fluid flow

The governing equations for the flow are the gravity-driven incompressible Navier-Stokes equations,

$$\vec{u}_t + (\vec{u}\cdot\nabla)\vec{u} = -\frac{1}{\rho_{\mathrm{w}}}\nabla p + \nu\nabla^2\vec{u} + \vec{g}\,, \tag{A.1a}$$

$$\nabla\cdot\vec{u} = 0\,. \tag{A.1b}$$

The boundary conditions for the flow on the exterior are those of an open-channel flow, however the moving ice wall, $y = \eta(x,t)$ requires a separation of the no-slip condition into tangential and normal components. The boundary conditions for the flow are,

$$\text{no-slip:} \qquad \hat{\mathbf{t}}\cdot\vec{u}|_{y=\eta} = 0\,, \tag{A.2a}$$

$$\text{freezing liquid:} \qquad \hat{\mathbf{n}}\cdot\vec{\tilde{u}}|_{y=\eta} = (1-r_\rho)\tilde{\eta}_{\tilde{t}} \tag{A.2b}$$

$$\text{kinematic:} \qquad \xi_t + (u|_{y=\xi})\xi_x = v|_{y=\xi}\,, \tag{A.2c}$$

$$\text{lateral stress:} \qquad \hat{\mathbf{n}}\cdot\underline{\tau}\cdot\hat{\mathbf{t}} = 0$$

$$\big[u_y + v_x\big]_{y=\xi} \approx 0\,, \tag{A.2d}$$

$$\text{normal stress:} \qquad \hat{\mathbf{n}}\cdot\underline{\tau}\cdot\hat{\mathbf{n}} + \gamma\mathcal{K} = -p_{\mathrm{atm}}$$

$$\big[-p + 2\rho_{\mathrm{w}}\nu_{\mathrm{w}}v_y\big]_{y=\xi} - \gamma\xi_{xx} \approx -p_{\mathrm{atm}}\,, \tag{A.2e}$$

The no-slip condition forces the tangential fluid velocity to be zero at the ice boundary $y = \eta(x,t)$. The "freezing" condition describes a flow of water outwards from the wall as water freezes. The ratio of densities between ice and water, $r_\rho = \rho_{\mathrm{i}}/\rho_{\mathrm{w}} \approx 0.92$, accounts for the mass adsorbed onto the ice. The freezing condition comes from mushy layer theory [49] which was derived from conservation of mass at the ice-water interface. For the solid icicle case, we use solid fraction $\varphi = 0$ in the water and $\varphi = 1$ in the ice. The "freezing liquid" condition is particular to solidification models, and differentiates it from a solid wall; we use Equation (2.15) from [49], which is derived from a conservation of mass at the ice-water interface. Here, ϕ is the solid fraction (1 in ice, and 0 in water), and r_ρ is the ratio of densities, $r_\rho = \rho_{\mathrm{i}}/\rho_{\mathrm{w}} \approx 0.92$. We

will see in Section 2.2 that liquid freezing on the surface appears as a small outward flow in the thin film. , and the kinematic condition is derived from the general form as detailed by Acheson [54] and Kundu [53], applied at the water-air interface ($y = \xi(x,t)$). For the stress-free conditions, we start with the same general form as Camporeale *et al.* [34], which permits a careful treatment of the rippled topography. The approximations shown for the stress-free conditions are more commonly used in cases where the boundaries are essentially flat. In the stress-free conditions, τ is the stress tensor, and $\mathcal{K}$ is the mean curvature of the air-water interface,

$$\mathcal{K} = \frac{\xi_{xx}}{2(1+\xi_x^2)^{3/2}}\,. \tag{A.3}$$

The mean curvature of the ice surface, which will be seen in the temperature boundary conditions has the same form, replacing ξ with η. Knowing that the rippled topography will be a small perturbation, we omit the quadratic terms of η and ξ in equations (A.2d) and (A.2e).

These boundary conditions, and the ones that follow incorporate the normal and tangent vectors defined as,

$$\hat{\mathbf{n}} = \frac{1}{\sqrt{1+\eta_x^2}}\begin{pmatrix}-\eta_x\\ 1\end{pmatrix} \qquad \text{and} \qquad \hat{\mathbf{t}} = \frac{1}{\sqrt{1+\eta_x^2}}\begin{pmatrix}1\\ \eta_x\end{pmatrix} \tag{A.4}$$

for the ice surface. The normal and tangent vectors for the water-air interface are the same, replacing η with ξ.

A.3 Impurity concentration

Because the boundary conditions for concentration are simpler, we present them before the thermal boundary conditions. The dissolved solids are treated as a passive tracer, and thus follow the advection diffusion equation,

$$C_t + (\vec{u}\cdot\nabla)C = D_\mathrm{s}\nabla^2 C\,, \tag{A.5}$$

where D_s is the diffusion coefficient for the impurity (salt).

The boundary conditions are both derived from conservation of mass. For rigour and future consistency with mushy layer theory, we start with equation (2.16) in [49],

$$r_\rho(1-k)C[\phi]V = [\bar{D}\hat{\mathbf{n}}\cdot\nabla C]\,, \tag{A.6}$$

where ϕ is the solid fraction, r_ρ is the ratio of densities, $r_\rho = \rho_\mathrm{i}/\rho_\mathrm{w}$, and the segregation coefficient k relates the solid concentration to the liquid $C_\mathrm{s} = kC$. This equation states that any impurities rejected from the ice during freezing must be transported away from the ice surface. It is very similar to the Stéfan condition (A.14) in the thermal boundary conditions. For water, we can assume $k = 0$. Using the values $\phi = 1$ and $C = 0$ for ice, and $\phi = 0$ for water, equation (A.6) becomes,

$$r_\rho C V = -D\hat{\mathbf{n}} \cdot \nabla C \,. \tag{A.7}$$

At the air-water interface, all dissolved solids must be contained in the liquid, so there is a zero-flux condition,

$$\hat{\mathbf{n}} \cdot \nabla C|_{y=\xi} = 0 \,. \tag{A.8}$$

Because the impurities are entirely contained in the water, these boundary conditions lead to a gradual accumulation of salt in the thin-film. A third boundary condition for concentration is necessary to make the problem well-defined. At the root of the icicle, the concentration is the feed-water concentration,

$$C(x = 0, y, t) = C_0 \,. \tag{A.9}$$

We show in Section 2.3.1 that this (along with consumption of water along the icicle) greatly complicates the linear stability analysis, because the domain is no longer infinite.

A.4 Temperature

For temperature, the governing equation is the standard advection-diffusion equation,

$$T_t + (\vec{u} \cdot \nabla)T = \kappa \nabla^2 T \tag{A.10}$$

where κ is the thermal diffusion coefficient. This equation applies both in the water and the ice. However, because the ice is fully-ensheathed in a liquid film, local thermal equilibrium at the ice-water interface forces the interior of the icicle to have $T_\mathrm{i} = T_\mathrm{m}$, so we do not need to model the temperature inside the icicle.

A.4.1 Temperature at ice surface

There are two conditions at the ice-water interface, which come from local thermal equilibrium and conservation of thermal energy. First, local thermal equilibrium appears as temperature continuity and incorporates *constitutional undercooling* and *capillary undercooling*. Constitutional undercooling requires that the temperature at the interface is equal to the *liquidus temperature* at the water's concentration,

$$T|_{y=\eta} = T_L(C) = T_L(C_0) + m(C|_{y=\eta} - C_0)\,, \tag{A.11}$$

where m is the slope of the liquidus, and C_0 is a reference concentration. Capilliary undercooling introduces a corrective factor to the melting point from the interfacial free energy, γ_i. This corrective factor is proportional to the local curvature, $\mathcal{K}$, which is a deviation from the flat equilibrium.

$$T|_{y=\eta} = T_\mathrm{m}\left(1 + 2\mathcal{K}\frac{\gamma_\mathrm{i}}{\rho_\mathrm{i} L}\right)\,, \tag{A.12}$$

where T_m is the melting temperature at equilibrium. Accounting for constitutional undercooling the melting temperature is the liquidus temperature at the liquid concentration, $T_\mathrm{m} = T_L(C)$. Combining the two effects results in the undercooling condition,

$$T|_{y=\eta} = \left(T_L(C_0) + m(C|_{y=\eta} - C_0)\right)\left(1 + 2\mathcal{K}\frac{\gamma_\mathrm{i}}{\rho_\mathrm{i} L}\right) \tag{A.13}$$

In (A.13), the $2\mathcal{K}\frac{\gamma_\mathrm{i}}{\rho_\mathrm{i} L}$ term is the correction for *capillary undercooling* (the Gibbs-Thomson effect) [55, 76], where L is the latent heat of fusion and $T_L(c)$ is the slope of the liquidus, which accounts for the constitutional undercooling. For the analysis, we treat T_L is constant, and the capillary undercooling will be seen to be negligible. A third correction for rapid freezing could be included, but the surface growth rate is quite low, so we're confident that it can be ignored. This was originally considered because of the assumption that *air bubbles* in rippled icicles indicated rapid freezing, but our experiments in Chapter 7 show that the inclusions are actually pockets of brine.

The second boundary condition at the ice surface is the Stéfan condition [55],

$$(\rho_\mathrm{i} L + 2\mathcal{K}\gamma_\mathrm{i})V = (\Lambda_\mathrm{i}\nabla T_\mathrm{i} - \Lambda_\mathrm{w}\nabla T_\mathrm{w})\cdot\hat{\mathbf{n}}\,, \tag{A.14}$$

where Λ is the thermal conductivity, and the second term on the left ($2\mathcal{K}\gamma_\mathrm{i}$) is a

correction for curvature similar to the Gibbs-Thompson effect. As is usually the case, we neglect the curvature correction, because its effect is quite small for our application.

A.4.2 Temperature at the air

There two conditions at the air-water interface. The first condition, temperature continuity, is quite simple,

$$T_{\mathrm{w}}|_{y=\xi} = T_{\mathrm{a}}|_{y=\xi}\,. \tag{A.15}$$

However, the heat flux across the interface is quite complicated. For a full treatment, the advection and diffusion in the air needs to be modelled as well as the effects of evaporative cooling and radiative cooling. The fluxes in our model are based on the work by Neufeld [46], which accurately model the 3 sources of heat-flux across a thin boundary-layer above ice. The thickness of the boundary layer is taken from Short *et al.* [44] who modelled the air boundary-layer on the surface of icicles.

The temperature boundary condition for heat flux at the air is,

$$-\Lambda_{\mathrm{w}}\hat{\mathbf{n}}\cdot\nabla T|_{y=\xi} = J_{AD} + J_R + J_H\,, \tag{A.16}$$

where J_{AD}, J_R and J_H are the heat fluxes from advection-diffusion, radiation and evaporation, respectively. The values of the three heat fluxes, based on Neufeld [46] are,

$$J_{AD}(x,t) = H(T\,|_{y=\xi} - T_{\mathrm{a}}^{\mathrm{mix}})\,, \tag{A.17}$$

$$J_R(x,t) = \sigma_B\big((T\,|_{y=\xi})^4 - T_{\mathrm{wall}}^4\big)\,, \tag{A.18}$$

$$J_H(x,t) = H_{\mathrm{v}}\Delta\rho_{\mathrm{v}} \tag{A.19}$$

The values H and H_{v} are parameters that approximate the heat flux from the boundary layer thickness and assumptions of a turbulent air flow. $\Delta\rho_{\mathrm{v}}$ is the difference in vapour density, across the air boundary layer. This model of the fluxes reduces the complicated three-dimensional air temperature problem into a much simpler (though still complex) one-dimensional model.

The parameter H is based on simple diffusion of heat across the boundary layer into a well-mixed atmosphere,

$$H = \frac{\Lambda_{\mathrm{a}}}{\delta}\mathrm{Nu}\,, \tag{A.20}$$

where δ is the thickness of the boundary layer, and the dimensionless Nusselt number

$\mathrm{Nu} \geq 1$ accounts (*or corrects*) for turbulent flow in the atmosphere.

The parameter H_v which models the effects of evaporative cooling can be related directly to H, because water vapour will undergo the same advective-diffusive behaviour as heat;

$$H_v = \frac{L_\mathrm{v}}{\rho_\mathrm{a} c_\mathrm{p,a}} H \,. \tag{A.21}$$

For determining the difference in vapour density, $\Delta\rho_\mathrm{v}$, across the boundary layer, we assume the air is fully saturated at the ice surface and subtract the vapour pressure in the mixed air,

$$\Delta\rho_\mathrm{v} = \rho_\mathrm{sat}(T|_{y=\xi}) - R_H \rho_\mathrm{sat}(T_\mathrm{a}^\mathrm{mix}) \,, \tag{A.22}$$

where R_H is the relative humidity in the air, and saturation vapour density is calculated as

$$\rho_\mathrm{sat}(T) = \rho_\mathrm{sat}(T_m) \frac{T_m}{T} \exp\left(-\frac{\mathcal{M} L_\mathrm{v}}{\mathcal{R}} \left[\frac{1}{T} - \frac{1}{T_\mathrm{m}} \right] \right) \,, \tag{A.23}$$

where $\mathcal{M}$ is the molar mass of water, and $\mathcal{R}$ is the gas constant.

Appendix B

Thin film non-dimensionalization

The full extension of the thin-film model as seen in Section 2.1 has many variables, $u, v, p, T, c, x, y, \eta, \xi$ and physical parameters. As such, the non-dimensionalization is quite involved, with many choices of relevant scales, and how best to define the dimensionless numbers. Choice of dimensionless numbers is essential for determining which terms can be left out, which assumptions (like quasi-static flow) can be made, and what the possible limits of the model are.

A key feature of the non-dimensionalization presented here is the separation of length and time scales. The thickness of the thin-film of liquid is much smaller than the typical ripple wavelength, so length scales are separated with an aspect ratio, μ. The velocity of the ice surface is much slower than the velocity of the fluid flow, so they are separated with another ratio $\bar{\text{v}}$, which also relates the hydrodynamic timescale to the freezing timescale. Finally, the amplitude of ripples on the surface are much smaller than the ripple wavelength, so they are separated with the ratio δ, which also serves as the perturbation parameter used in Section 2.3 for linear stability analysis.

To non-dimensionalize the thin-film model, we start by establishing the re-scaled variables in Section B.1 which will be used in all dimensionless equations. The reason for our choice of scales and dimensionless numbers are explained in that section, with further explanations of the dimensionless numbers as they appear in subsequent sections. This appendix is then divided into sections for the equations related to fluid flow, temperature and concentration. The Navier-Stokes equations, and related boundary conditions are non-dimensionalized in Section B.2. Temperature non-dimensionalization is presented in Section B.3, and the non-dimensionalized concentration equations are in Section B.4.

B.1 Dimensionless variables

In order to non-dimensionalize the problem, we chose separate scales for x, y, u, and v. This is conventional for low aspect-ratio problems like shallow water waves, because the there are two vastly different length-scales involved. Separating the horizontal and vertical scales provides many simplifications in low-aspect flows. A cautious approach is to leave all the length, time, and velocity scales independent, and then define their relations only after they have been substituted into the model. This is the approach that we followed originally, but the resulting conclusions are presented here from the beginning.

A further consideration is the moving reference frame. While the Navier-Stokes and advection-diffusion equations are invariant under Gallilean shifts, the mushy-layer equations are not, because of the solid fraction, ϕ. In order to be particularly careful, we include the moving reference frame in the non-dimensional variables (y, v, η, and ξ), ensuring that it is accounted for in the boundary conditions, and allowing the same non-dimensionalization to be applied to a mushy-layer based theory.

The variable scales are defined as follows, with tildes indicating the dimensional (physical) quantities.

$$\begin{aligned}
\tilde{x} &= x\frac{h}{\mu} & \tilde{y} &= hy + \bar{V}\tilde{t} & \tilde{t} &= \tau_F t = \frac{h}{\bar{V}}t \\
\tilde{u} &= Uu & \tilde{v} &= \mu U v + \bar{V} & \tilde{p} &= Pp + p_0 \\
\tilde{T} &= \Delta T T + T_{\mathrm{m}} & C &= \Delta C c\,, &&
\end{aligned}$$

where h is the depth if the water film, and $\bar{V}$ is the average velocity of the ice surface (i.e. average radial growth rate of the icicle). For mushy layer theory [16, 61], it is common to use a reference temperature C_0 as the eutectic concentration, but that is a much higher concentration than is reached in the liquid on icicles. Another possibility would be to use the feed-water concentration as C_0, but this adds many extra terms to the boundary conditions for concentration. Instead, we set $C_0 = 0$, which subsumes the feed water concentration into $c(x, y, t)$ and ensures all concentrations are positive.

The characteristic scale U is chosen as the surface velocity of water along the icicle, and ΔT is the temperature difference across the liquid film, typically a few milli-Kelvin. We follow the convention in mushy layer theory [16, 61], in defining ΔC according to the liquidus slope, $\Delta C = \Delta T/m$, where m is the slope of the liquidus. These scales give most dimensionless variables values between 0 and 1 inside the liquid film. The exception is concentration, which now provides the change in the freezing

point.

We have also encountered our first choice for aspect ratio, and the relevant time scale,

$$\mu = kh\,, \qquad\qquad \tau_F = \frac{h}{\bar{V}}\,.$$

The aspect ratio, μ, is best understood as the ratio between film thickness (h) and the characteristic wave number (k), which we expect to match the ripple wavelength ($\lambda = 2\pi/k \approx 1$ cm). It is similar to the shallow-water approximation for gravity waves, where k would be the wavelength of a surface wave. We chose the symbol μ to be consistent with Ogawa & Furukawa [25], who used $\mu = kh$ with k as the ripple wavenumber, left unfixed in analysis, but understood to be $\lambda \approx$1 cm.

The time scale $h/\bar{V}$ is chosen based on the Stéfan condition B.3.1 at the ice-water boundary. It is the amount of time taken for the ice to grow through one film thickness. Considering this time-scale, we define another small parameter, $\bar{\mathrm{v}} = \bar{V}/U \ll 1$, which establishes the quasi-static approximation for the thin-film flow.

Another time scale is also possible, $\tau = h/\mu U$, which would ensure that the length, time and velocity scales are congruent. That is, $\tilde{u} = \frac{\partial \tilde{x}}{\partial \tilde{t}}$ and $\tilde{v} = \frac{\partial \tilde{y}}{\partial \tilde{t}}$. Thus, τ is the hydrodynamic timescale, defined as the time taken for water on the surface to travel the length of one ripple, (scaled by 2π).

By using τ_F instead of τ, the quasi-steady approximation for fluid flow is made explicit in the Navier Stokes equations, meaning that the flow would reach equilibrium much faster than the ice freezes. This approximation is quantified by another small parameter, $\bar{\mathrm{v}} = \mu\tau/\tau_F = \bar{V}/U \approx 4.8 \times 10^{-5}$, which establishes the quasi-static approximation for the thin-film flow.

The other variables which need to be non-dimensionalized are related to the moving boundaries, $y = \eta(x,t)$, and $y = \xi(x,t)$. Because the normal and tangent vector are used in many boundary conditions, we also non-dimensionalize them here. The ice and water surfaces are defined by the functions,

$$\tilde{\eta}(\tilde{x},\tilde{t}) = \bar{V}\tilde{t} + \eta_0\eta \qquad\qquad \tilde{\xi}(\tilde{x},\tilde{t}) = h + \bar{V}\tilde{t} + \eta_0\xi\,,$$

where η_0 is the non-dimensional amplitude of η, and we assume that ξ has a similar size of variation. This introduces the third length scale η_0, and the aspect ratio for it is against the wavenumber, $\delta = k\eta_0$. The linear perturbation will be performed on δ, using the form $\eta(x,t) = \delta e^{\sigma t}\cos(kx - \omega t)$, which means that it applies only when ripple amplitudes are small compared ripple wavelength.

The normal and tangent vectors are

$$\tilde{\mathbf{n}} = \frac{1}{\sqrt{1+(\delta\eta_x)^2}}\begin{pmatrix}-\delta\eta_x\\1\end{pmatrix} \qquad \tilde{\mathbf{t}} = \frac{1}{\sqrt{1+(\delta\eta_x)^2}}\begin{pmatrix}1\\\delta\eta_x\end{pmatrix}, \tag{B.1}$$

for the ice-water interface, and have a similar form for the water-air interface, except with ξ instead of η. Because we will use linear stability theory to analyse the thin-film theory, quadratic terms in δ can be ignored. Using a binomial expansion, $\left(1+(\delta\eta_x)^2\right)^{-1/2} = 1+\mathcal{O}(\delta^2)$, so that factor can be ignored in the non-dimensionalization calculations.

B.2 The Flow

We begin with the incompressible Navier-Stokes equations for the water, as defined in equation (2.1a),

$$\vec{\tilde{u}}_{\tilde{t}} + \vec{\tilde{u}}\cdot\tilde{\nabla}\vec{\tilde{u}} = -\rho_{\mathrm{w}}\tilde{\nabla}p + \nu\tilde{\nabla}^2\vec{\tilde{u}} + \vec{\tilde{g}}\,, \tag{B.2}$$

$$\tilde{\nabla}\cdot\vec{\tilde{u}} = 0\,. \tag{B.3}$$

The non-dimensionalization is simply a coordinate transform, where the chain rule is used to relate the derivatives of the dimensional variables to the non-dimensional variables. Normally, this is simple to do, but because of the moving reference frame, the time derivative is less trivial. A sample of the derivatives of $\tilde{u}$ is,

$$\begin{aligned}
\tilde{u} &= Uu & \tilde{u}_{\tilde{t}} &= \frac{U}{\tau}u_t + \frac{\partial\tilde{u}}{\partial u}\frac{\partial y}{\partial\tilde{t}}u_y\\
\tilde{u}_{\tilde{x}} &= U\frac{\mu}{h}u_x & &= \frac{U}{\tau}u_t - \frac{U\bar{V}}{h}u_y\\
\tilde{u}_{\tilde{x}\tilde{x}} &= U\frac{\mu^2}{h^2}u_{xx} & &= \frac{U\bar{V}}{h}\left(u_t+u_y\right)
\end{aligned}$$

Note that the time derivative has an extra $-u_y$, which will cancel out with the advection term in Gallilean-invarient equations.

The first equation considered is the conservation of mass (B.3),

$$\begin{aligned}
\tilde{u}_{\tilde{x}} + \tilde{v}_{\tilde{y}} &= 0\\
U\frac{\mu}{h}u_x + \frac{\mu U}{h}v_y &= 0\\
u_x + u_y &= 0\,.
\end{aligned} \tag{B.4}$$

This condition justifies the aspect ratio $\mu = kh$ applying to both length scales $(x,\, y)$ and velocities $(u,\, v)$. If they had different aspect ratios, then the u_x and u_y terms would not balance properly, and conservation of mass could not be realized.

B.2.1 Navier Stokes

Continuing with the Navier-Stokes equations (B.2), the governing equation for $u(x, y, t)$ is,

$$\begin{aligned}
\tilde{u}_{\tilde{t}} + \tilde{u}\tilde{u}_{\tilde{x}} + \tilde{v}\tilde{u}_{\tilde{y}} &= -\frac{\tilde{p}_{\tilde{x}}}{\rho_{\mathrm{w}}} + \nu(\tilde{u}_{\tilde{x}\tilde{x}} + \tilde{u}_{\tilde{y}\tilde{y}}) \\
\frac{U\bar{V}}{h}(u_t - u_y) + \frac{U^2\mu}{h}uu_x + \frac{U}{h}(\mu U v + \bar{V})u_y &= -\frac{P\mu}{\rho_w h}p_x + \nu(\frac{U\mu^2}{h^2}u_{xx} + \frac{U}{h^2}u_{yy}) + g\cos(\theta) \\
\bar{\mathrm{v}}u_t + \mu uu_x + \mu vu_y &= -\frac{P\mu}{\rho_w U^2}p_x + \frac{\nu}{Uh}(\mu^2 u_{xx} + u_{yy}) + \frac{hg\cos(\theta)}{U^2} \\
\bar{\mathrm{v}}u_t + \mu(uu_x + vu_y) &= -\mu p_x + \frac{1}{\mathrm{Re}}(\mu^2 u_{xx} + u_{yy} + 2)\,. \qquad \text{(B.5)}
\end{aligned}$$

In the last line, the pressure scale was chosen as $P = \rho_w U^2$. The velocity $U = gh^2\cos(\theta)/2\nu$ is selected from the parabolic shear flow solution and greatly simplifies the equation. For consistency with the other papers [19, 25, 26, 27, 28, 29, 30, 31, 32], we define $\mathrm{Re} = Uh/\nu$. That choice is also based on the coefficient of the leading order viscous term, u_{yy}.

Applying the same procedure to equation (B.2) for v (details omitted) results in

$$\bar{\mathrm{v}}\mu v_t + \mu^2(uv_x + vv_y) = -p_y + \frac{\mu}{\mathrm{Re}}\left(\mu^2 v_{xx} + v_{yy} + 2\tan(\theta)\right)\,. \qquad \text{(B.6)}$$

Of note, all terms apart from p_y are of order μ or smaller. In the case of a vertical wall, $\theta = 0$ implies $\tan(\theta) = 0$, which is the case for the bulk of our analysis.

B.2.2 Ice surface

There are two boundary conditions for liquid flow on the ice surface, "no-slip", and "freezing liquid".

No-slip

The standard boundary condition for viscous flow beside a wall is the "no-slip" condition, $\vec{u} = 0$. However, the moving boundary condition requires splitting the condition

into normal and tangential parts. Tangential to the ice surface, the flow must be zero,

$$\begin{aligned}
\tilde{\mathbf{t}} \cdot \vec{\tilde{u}} &= 0 \\
\frac{1}{\sqrt{1+(\delta\eta_x)^2}} \begin{pmatrix} 1 \\ \delta\eta_x \end{pmatrix} \cdot \begin{pmatrix} \tilde{u} \\ \tilde{v} \end{pmatrix} &= 0 \\
U u + \delta\eta_x(\mu U v + \bar{V}) &= 0 \\
u + \delta\eta_x \left(\mu v + \frac{\bar{V}}{U} \right) &= 0 \\
u + \delta\eta_x \left(\mu v + \bar{\mathrm{v}} \right) &= 0 \,, \qquad \text{(B.7)}
\end{aligned}$$

where we use the time-scale ratio, $\bar{\mathrm{v}} = \bar{V}/U$. Note that in the absence of perturbation $\delta = 0$ and equation (B.7) becomes $u = 0$.

Freezing liquid

The normal velocity at the ice surface also includes a mass-flux as liquid freezes and is absorbed into the icicle. The different densities of water and ice [49] ($r_\rho = \rho_\mathrm{i}/\rho_\mathrm{w}$), result in a small mass flux.

$$\begin{aligned}
\left[\hat{\mathbf{n}} \cdot \vec{\tilde{u}} \right]_i^w &= -(1-r_\rho)\tilde{\eta}_{\tilde{t}}[\phi]_i^w \\
\hat{\mathbf{n}} \cdot [\vec{\tilde{u}} - \vec{0}] &= -(1-r_\rho)\tilde{\eta}_{\tilde{t}}[0-1] \\
-\mu\delta\eta_x U u + (\mu U v + \bar{V}) &= (1-r_\rho)\bar{V}(1+\frac{\eta_0}{h}\eta_t) \\
\mu v - \delta u \eta_x + \frac{\bar{V}}{U} &= \frac{\bar{V}}{U}(1-r_\rho)\left(1+\frac{\delta}{\mu}\eta_t\right) \\
\mu v - \delta u \eta_x &= -r_\rho \bar{\mathrm{v}} + \frac{\bar{\mathrm{v}}}{\mu}\delta(1-r_\rho)\eta_t \,, \qquad \text{(B.8)}
\end{aligned}$$

after quadratic terms in δ are omitted. Note that when the interface is flat, $\delta = 0$, the velocity is negative,

$$v = -r_\rho \frac{\bar{V}}{\mu U} \,, \quad \text{or} \quad v = -r_\rho \frac{\bar{\mathrm{v}}}{\mu} \,.$$

This result is different from the usual case of an impermeable wall. Keeping in mind that our reference frame is moving with the ice surface, an impermeable wall would have $v = 0$, but if all liquid is absorbed into the ice as it grows, then $\tilde{v} = 0 \Rightarrow v = -\bar{V}/(\mu U)$. The density ratio, $r_\rho \approx 0.92$, shows that we're closer to full absorption.

Given that the hydrodynamics happen much faster than freezing ($\bar{\mathrm{v}} = \mu\tau/\tau_F \ll 1$), this effect is very small. It is worth noting from table 2.2 that $\bar{\mathrm{v}} \sim \mu^4$.

B.2.3 Free surface

On the free surface, there are both kinematic and dynamic conditions. The normal and tangent vectors are the same as in (B.1), except with ξ instead of η for the surface. We begin with the kinematic condition.

B.2.4 Kinematic condition

According to Acheson [54] and Kundu [53], the general kinematic condition is,

$$\begin{aligned} 0 &= \frac{D}{D\tilde{t}}(\tilde{\xi} - \tilde{y}) \\ 0 &= \tilde{\xi}_{\tilde{t}} + \tilde{u}\tilde{\xi}_{\tilde{x}} - \tilde{y}_{\tilde{t}} - \tilde{v} \\ 0 &= \left(\bar{V} + \frac{\xi_0 \bar{V}}{h}\xi_t\right) + \delta U u \xi_x - \bar{V} - \mu U v \\ \mu v &= \delta\left(\frac{\bar{\mathrm{v}}}{\mu}\xi_t + u\xi_x\right). \end{aligned} \tag{B.9}$$

Setting $\delta = 0$ to remove the perturbation gives $v|_{y=\xi} = 0$, as expected given that we assume a constant film thickness, h. However, given a constant flow rate, and acknowledging loss of liquid water due to freezing (see equation (B.8)), the film thickness should actually decrease if the radius is constant. Modelling the thinning film would require a more general form of $\xi(x,t)$ where the x-dependence is not entirely proportional to δ. However, in the linear stability analysis, we ignore the adsorption of water, because it is negligible compared to the rest of the flow. This may be further justified by the decrease in radius in x, which in turn increases the water flux per unit area.

Lateral stress

The lateral and normal stress conditions must be non-dimensionalized from the tensor form, because the normal and tangent vectors are not constant. The stress tensor is

defined as,

$$\begin{aligned}\tilde{\underline{\tau}} &= -\tilde{p}\begin{bmatrix}1 & 0\\ 0 & 1\end{bmatrix} + 2\rho\nu\begin{bmatrix}\tilde{u}_{\tilde{x}} & \frac{1}{2}(\tilde{u}_{\tilde{y}}+\tilde{v}_{\tilde{x}})\\ \frac{1}{2}(\tilde{u}_{\tilde{y}}+\tilde{v}_{\tilde{x}}) & \tilde{v}_{\tilde{y}}\end{bmatrix}\\ &= -(Pp+p_{\text{atm}})\begin{bmatrix}1 & 0\\ 0 & 1\end{bmatrix} + \frac{\rho\nu U}{h}\begin{bmatrix}2\mu u_x & (u_y+\mu^2 v_x)\\ (u_y+\mu^2 v_x) & 2\mu v_y\end{bmatrix}. \end{aligned} \tag{B.10}$$

Using this definition in the lateral stress condition (2.2d), we find

$$\begin{aligned}\tilde{\mathbf{n}}\cdot\tilde{\underline{\tau}}\cdot\tilde{\mathbf{t}} &= 0\\ \begin{pmatrix}-\delta\xi_x & 1\end{pmatrix}\left(\frac{\rho\nu U}{h}\begin{bmatrix}2\mu u_x & (u_y+\mu^2 v_x)\\ (u_y+\mu^2 v_x) & 2\mu v_y\end{bmatrix}\right)\begin{pmatrix}1\\ \delta\xi_x\end{pmatrix} &= 0\\ \begin{pmatrix}\delta\xi_x & -1\end{pmatrix}\begin{pmatrix}2\mu u_x-\delta\xi_x(u_y+\mu^2 v_x)\\ (u_y+\mu^2 v_x)+2\mu\delta v_y\xi_x\end{pmatrix} &= 0\\ 2\mu\delta u_x\xi_x-(\delta\xi_x)^2(u_y+\mu^2 v_x)-(u_y+\mu^2 v_x)-2\mu\delta v_y\xi_x &= 0\\ (u_y+\mu^2 v_x)+2\mu\delta\xi_x(v_y-u_x) &= 0\,, \end{aligned} \tag{B.11}$$

where terms of order $\mathcal{O}(\delta^2)$ are dropped. Note that the perturbation term with coefficient δ is not present in the typical approximation of this boundary equation in (A.2d).

Normal Stress

Using the stress tensor (B.10) in the normal stress boundary (2.2e),

$$\begin{aligned}\tilde{\mathbf{n}}\cdot\tilde{\underline{\tau}}\cdot\tilde{\mathbf{n}}+\gamma\mathcal{K} &= -p_{\text{atm}}\\ -(Pp+p_{\text{atm}})+\frac{\rho\nu U}{h}\begin{pmatrix}\delta\xi_x\\ -1\end{pmatrix}\cdot\begin{pmatrix}2\mu u_x\delta\xi_x-(u_y+\mu^2 v_x)\\ \delta\xi_x(u_y+\mu^2 v_x)-2\mu v_y\end{pmatrix}-\mu\frac{\gamma}{h}\delta\xi_{xx} &= -p_{\text{atm}}\\ -Pp+\frac{\rho\nu U}{h}\left[-2\delta\xi_x(u_y+\mu^2 v_x)+2\mu v_y\right]-\mu\frac{\gamma}{h}\delta\xi_{xx} &= 0\\ -p+2\frac{\nu}{Uh}\left[\mu v_y-\delta(u_y+\mu^2 v_x)\xi_x\right]-\mu\frac{\gamma}{\rho U^2 h}\delta\xi_{xx} &= 0\,, \end{aligned}$$

where quadratic terms in δ were omitted throughout calculations. After substituting $\text{Re}=\nu/Uh$ and $\text{We}=\gamma/\rho U^2 h$, we find the familiar form,

$$-p+\frac{2}{\text{Re}}\left[\mu v_y-\delta\xi_x(u_y+\mu^2 v_x)\right]-\mu\frac{1}{\text{We}}\delta\xi_{xx}=0\,. \tag{B.12}$$

This differs slightly from the typical form of the normal stress condition due to the aspect ratios μ and δ. A common approach when linearizing boundary conditions is to "pull-back" $u(x,\xi,t)$ and $v(x,\xi,t)$ to $y=0$ through a Taylor approximation. Doing this would have the same effect.

B.3 Temperature

The non-dimensionalization of the temperature governing equation is quite straightforward. Substituting the scaled temperature into (2.1c), we find

$$\begin{aligned}
\tilde{T}_{\tilde{t}} + \tilde{u}\tilde{T}_{\tilde{x}} + \tilde{v}\tilde{T}_{\tilde{y}} &= \kappa(\tilde{T}_{\tilde{x}\tilde{x}} + \tilde{T}_{\tilde{y}\tilde{y}}) \\
\frac{\Delta T\bar{V}}{h}T_t - \cancel{\frac{\Delta T\bar{V}}{h}} + \mu\frac{\Delta TU}{h}uT_x + \frac{\Delta T}{h}\left(\mu Uv + \cancel{\bar{V}}\right)T_y &= \frac{\kappa\Delta T}{h^2}(\mu^2 T_{xx} + T_{yy}) \\
\bar{\mathrm{v}}T_t + \mu(uT_x + vT_y) &= \frac{1}{\mathrm{Pe}}(\mu^2 T_{xx} + T_{yy})\,, \qquad \text{(B.13)}
\end{aligned}$$

where the Peclet number $\mathrm{Pe} = Uh/\kappa_w$ is the ratio between advective and diffusive transport. This equation is exactly what we'd expect, with diffusion in the y-direction being the dominant transport, due to the thinness of the liquid film.

B.3.1 Temperature at ice surface

Stéfan Condition

The Stéfan condition is the most complicated in terms of physical parameters. It justifies the time-scale $h/\bar{V}$ and the perturbation parameter $\delta = k\eta_0$. Using the Stéfan condition as defined by Worster [49] and the definitions of the normal vector in (B.1),

$$\begin{aligned}
\rho_{\mathrm{i}}L\frac{\partial\tilde{\eta}}{\partial\tilde{t}} &= \left[\Lambda\hat{\mathbf{n}}\cdot\tilde{\nabla}\tilde{T}|_{\tilde{y}=\tilde{\eta}}\right]_w^i \\
\rho_{\mathrm{i}}L\left(\bar{V} + \frac{\eta_0\bar{V}}{h}\eta_t\right) &= \left[\frac{\Lambda\Delta T}{h}\begin{pmatrix}-\delta\eta_x\\1\end{pmatrix}\cdot\begin{pmatrix}\mu T_x\\T_y\end{pmatrix}\right]_i - \left[\frac{\Lambda\Delta T}{h}\begin{pmatrix}-\delta\eta_x\\1\end{pmatrix}\cdot\begin{pmatrix}\mu T_x\\T_y\end{pmatrix}\right]_w \\
\frac{\rho_{\mathrm{i}}LUh}{\Delta T}\frac{\bar{V}}{U}\left(1 + \frac{\delta}{\mu}\eta_t\right) &= \Lambda_{\mathrm{i}}\left(\theta_y - \delta\mu\eta_x\theta_x\right) - \Lambda_{\mathrm{w}}\left(T_y - \delta\mu\eta_x T_x\right)\,, \qquad \text{(B.14)}
\end{aligned}$$

where θ represents the temperature in the ice, while T is the temperature in the water. Equation (B.14) has many physical parameters, some of them with both liquid and solid versions. To continue with the non-dimensionalization of the Stéfan condition,

we use the next non-dimensional number, the Stéfan number commonly defined [16] as $\mathcal{S} = \frac{L}{c_{pw}\Delta T}$. The Stefan number is the ratio between the amount of heat generated at the surface due to freezing, and the sensible heat required to cool the liquid.

In order to arrange the physical parameters, we keep in mind the relation $\kappa = \Lambda/\rho c_p$, and define the ratios $r_\rho = \rho_\mathrm{i}/\rho_\mathrm{w}$ and $r_\Lambda = \Lambda_\mathrm{i}/\Lambda_\mathrm{w}$.

$$
\begin{aligned}
-\frac{\rho_\mathrm{w} LUh}{\Delta T \Lambda_\mathrm{w}} \frac{\rho_\mathrm{i}}{\rho_\mathrm{w}} \bar{\mathrm{v}} \left(1 + \frac{\delta}{\mu}\eta_t\right) &= \left(T_y - \frac{\Lambda_\mathrm{i}}{\Lambda_\mathrm{w}}\theta_y\right) - \mu\delta\eta_x \left(T_x - \frac{\Lambda_\mathrm{i}}{\Lambda_\mathrm{w}}\theta_x\right) \\
-r_\rho \mathcal{S} \frac{Uh}{\kappa_w} \bar{\mathrm{v}}(\mu + \delta\eta_t) &= \mu\left(T_y - r_\Lambda\theta_y\right) - \mu^2\delta\eta_x\left(T_x - r_\Lambda\theta_x\right) \\
-r_\rho \mathrm{Pe}\, \mathcal{S}\, \bar{\mathrm{v}}(\mu + \delta\eta_t) &= \mu\left(T_y - r_\Lambda\theta_y\right) - \mu^2\delta\eta_x\left(T_x - r_\Lambda\theta_x\right) . \qquad \text{(B.15)}
\end{aligned}
$$

The ratio of densities must be introduced so that $\mathcal{S}$ uses the heat capacity of water instead of ice. Because the temperature inside the ice is assumed constant with $\tilde{T}_\mathrm{i} = T_L(C_0)$ (see Appendix A.4), $\theta_x = \theta_y = 0$, and the Stéfan condition is significantly simpler,

$$
-r_\rho \mathrm{Pe}\, \mathcal{S}\, \bar{\mathrm{v}}(\mu + \delta\eta_t) = \mu T_y - \mu^2\delta\eta_x T_x \,. \qquad \text{(B.16)}
$$

The Stéfan condition provides the reason for the freezing timescale $\tau_F = h/\bar{V}$, as it defines the rate of freezing from the temperature gradient. Setting $\delta = 0$ to remove the perturbation, and using the temperature scaling, which implies $T_y = -1$ in the unperturbed state,

$$
(r_\rho \mathrm{Pe}\, \mathcal{S}\,)\bar{\mathrm{v}} = 1
$$

Thus, the unperturbed Stéfan condition relates the two timescales ($\bar{\mathrm{v}} = \mu\tau/\tau_F$) through other dimensionless numbers:

$$
\bar{\mathrm{v}} = (r_\rho \mathrm{Pe}\, \mathcal{S}\,)^{-1} \approx 5 \times 10^{-5} \,, \qquad \text{(B.17)}
$$

using the values in Table 2.2. Note that is is common to approximate $r_\rho = 1$ to ignore the expansion of ice [16, 49].

Undercooling

The undercooling condition is boundary condition that most strongly couples the temperature field to the concentration field. We include the Gibbs-Thomson effect in the physical model for the sake of completeness, but non-dimensionalization shows that this term is insignificant compared to the constitutional undercooling.

Starting with equation (2.3b),

$$\begin{aligned}\tilde{T}|_{y=\eta} &= \left(T_\mathrm{m} + m\tilde{C}|_{y=\eta}\right)\left(1 + 2\mathcal{K}\frac{\gamma_\mathrm{i}}{\rho_\mathrm{i}L}\right)\\ \Delta T T + T_\mathrm{m} &= \left(T_\mathrm{m} + m\Delta C c|_{y=\eta}\right)\left(1 + 2\frac{\mu\delta}{h}\frac{\gamma_\mathrm{i}}{\rho_\mathrm{i}L}\eta_{xx}\right)\\ T &= c + 2\mu\delta\Gamma\eta_{xx}\left(\frac{T_\mathrm{m}}{\Delta T}\right)\,, \end{aligned} \tag{B.18}$$

where $\Gamma = \frac{\gamma_\mathrm{i}}{\rho_\mathrm{i}Lh}$ is a dimensionless number characterizing the Gibbs-Thomson effect. We calculate $\Gamma \approx 6.5 \times 10^{-7}$, so the Gibbs-Thomson effect is insignificant, even with $T_\mathrm{m}/\Delta T \approx 10^5$.

Ignoring the Gibbs-Thomson effect, the undercooling condition becomes,

$$T(x, y{=}\eta, t) = c(x, y{=}\eta, t)\,. \tag{B.19}$$

B.3.2 Temperature at free surface

The temperature continuity condition at the free surface is unaffected by the non-dimensionalization,

$$T_\mathrm{w}|_{y=\xi} = T_\mathrm{a}|_{y=\xi}\,. \tag{B.20}$$

The thermal flux between the water and the air is much more complicated. If the full forms of all three fluxes were written out completely, then it would be quite lengthy. However, the average heat flux will be calculated from experimental data, so we simply need to scale it after the calculation. After scaling, the heat flux condition is,

$$T_y - \mu\delta T_y\eta_x = \frac{h}{\Lambda_\mathrm{w}\Delta T}(J_{AD} + J_R + J_H)\,. \tag{B.21}$$

B.4 Concentration

Similarly to temperature, the governing equation for concentration is the advection-diffusion equation (2.1d), so the non-dimensionalization follows the same procedure,

$$\begin{aligned}
\tilde{C}_{\tilde{t}} + \tilde{u}\tilde{C}_{\tilde{x}} + \tilde{v}\tilde{C}_{\tilde{y}} &= D_s(\tilde{C}_{\tilde{x}\tilde{x}} + \tilde{C}_{\tilde{y}\tilde{y}}) \\
\frac{\Delta C\bar{V}}{h}C_t - \cancel{\frac{\Delta C\bar{V}}{h}} + \mu\frac{\Delta CU}{h}uC_x + \frac{\Delta C}{h}\left(\mu Uv + \cancel{\bar{V}}\right)C_y &= \frac{D_s\Delta C}{h^2}(\mu^2 C_{xx} + C_{yy}) \\
\bar{\mathrm{v}}C_t + \mu(uC_x + vC_y) &= \frac{1}{\mathrm{Le}\,\mathrm{Pe}}(\mu^2 C_{xx} + C_{yy})\,,
\end{aligned} \tag{B.22}$$

where Le is the Lewis number, which relates thermal diffusivity to mass diffusivity, $\mathrm{Le} = \frac{\kappa}{D_s}$.

B.4.1 Concentration at ice surface

All of the impurities at the ice surface are rejected from the ice, as explained in Section A.3. Starting from equation (2.3e),

$$\begin{aligned}
r_\rho\tilde{C}\tilde{\eta}_{\tilde{t}} &= -D\tilde{\mathbf{n}}\cdot\tilde{\nabla}\tilde{C} \\
r_\rho\Delta Cc\left(\bar{V} + \frac{\bar{V}\delta}{\mu}\eta_t\right) &= -\frac{D\Delta C}{h}(c_y - \mu\delta c_x\eta_x) \\
r_\rho\mathrm{Le}\,\mathrm{Pe}\,\frac{\bar{V}}{U}\left(1 + \frac{\delta}{\mu}\eta_t\right)c &= -c_y + \mu\delta c_x\eta_x \\
r_\rho\mathrm{Le}\,\mathrm{Pe}\,\bar{\mathrm{v}}\,(\mu + \delta\eta_t)\,c &= -\mu c_y + \mu^2\delta c_x\eta_x\,.
\end{aligned} \tag{B.23}$$

The coefficient on the left-hand side of (B.23) can be rewritten by considering the value of $\bar{\mathrm{v}}$ found for the Stéfan condition in Section B.3.1. If $\bar{\mathrm{v}} = (r_\rho\mathrm{Pe}\,\mathcal{S})^{-1}$, then $r_\rho\mathrm{Pe}\,\bar{\mathrm{v}} = \mathcal{S}^{-1}$, and equation (B.23) can be rewritten as,

$$(\mu + \delta\eta_t)\,c = -\mu\frac{\mathcal{S}}{\mathrm{Le}}\,(c_y - \mu\delta c_x\eta_x)\,. \tag{B.24}$$

This boundary condition results in an accumulation of impurities as the liquid water descends down the icicle. This accumulation is quite slow according to the $\mu\bar{\mathrm{v}}$ term. Without the perturbation, there is a direct relation between the concentration and its gradient at the surface.

B.4.2 Concentration at air-water interface

At the air-water interface, dissolved solids cannot escape into the surrounding air, which also contributes to the accumulation of impurities in the liquid water. This boundary condition is simpler than at the ice surface. Starting with equation (2.3f),

$$\begin{aligned} \tilde{\mathbf{n}} \cdot \tilde{\nabla} \tilde{C}|_{y=\xi} &= 0 \\ c_y - \mu \delta c_x \xi_x &= 0 \,. \end{aligned} \tag{B.25}$$

So, in a flat unperturbed surface, the concentration gradient is zero. The effects from the perturbation are limited further by the factor of μ in the second term.

B.5 Summary

The whole non-dimensionalized model is collected in this section for reference. In the non-dimensionalized model, there are three small dimensionless ratios,

$$\mu = kh \qquad \bar{\mathrm{v}} = \frac{\bar{V}}{U} \,, \qquad \delta = k\eta_0 \,. \tag{B.26}$$

The aspect ratio μ is the small-aspect ratio approximation of the thin-film, related to the hydrodynamics. The time ratio $\bar{\mathrm{v}}$ separates the time scales for the moving ice surface and the fluid velocity. The aspect ratio δ is for the ice surface, so small δ implies the ripple hight is very small compared to its wavelength. This will be used in the perturbation of icicles.

The governing equations for the flow are,

$$\bar{\mathrm{v}} u_t + \mu(u u_x + v u_y) = -\mu p_x + \frac{1}{\mathrm{Re}}(\mu^2 u_{xx} + u_{yy} + 2) \,, \tag{B.27a}$$

$$\bar{\mathrm{v}} \mu v_t + \mu^2(u v_x + v v_y) = -p_y + \frac{\mu}{\mathrm{Re}} \left(\mu^2 v_{xx} + v_{yy} + 2\tan(\theta)\right) \,, \tag{B.27b}$$

$$u_x + u_y = 0 \,, \tag{B.27c}$$

with boundary conditions,

$$u + \delta\eta_x\left(\mu v + \bar{\mathrm{v}}\right) = 0\,, \tag{B.28a}$$

$$\mu v - \delta u\eta_x = -r_\rho\bar{\mathrm{v}} + \frac{\bar{\mathrm{v}}}{\mu}\delta(1-r_\rho)\eta_t\,, \tag{B.28b}$$

$$\mu v = \delta\left(\frac{\bar{\mathrm{v}}}{\mu}\xi_t + u\xi_x\right)\,, \tag{B.28c}$$

$$(u_y + \mu^2 v_x) + 2\mu\delta\xi_x(v_y - u_x) = 0\,, \tag{B.28d}$$

$$-p + \frac{2}{\mathrm{Re}}\left[\mu v_y - \delta\xi_x(u_y + \mu^2 v_x)\right] - \mu\frac{1}{\mathrm{We}}\delta\xi_{xx} = 0\,. \tag{B.28e}$$

The growth of an icicle is dictated by the temperature and concentration of the thin film. They follow the relatively rapid flow as passive tracers, with governing equations,

$$\bar{\mathrm{v}}T_t + \mu(uT_x + vT_y) = \frac{1}{\mathrm{Pe}}(\mu^2 T_{xx} + T_{yy})\,, \tag{B.29a}$$

$$\bar{\mathrm{v}}C_t + \mu(uC_x + vC_y) = \frac{1}{\mathrm{Le}\,\mathrm{Pe}}(\mu^2 C_{xx} + C_{yy})\,. \tag{B.29b}$$

The entirety of the icicle growth is modelled through the boundary conditions of the temperature and concentration fields,

$$T = c + 2\mu\delta\Gamma\eta_{xx}\left(\frac{T_\mathrm{m}}{\Delta T}\right)\,, \tag{B.30a}$$

$$T(x, y{=}\eta, t) = c(x, y{=}\eta, t)\,. \tag{B.30b}$$

$$-r_\rho\mathrm{Pe}\,\mathcal{S}\,\bar{\mathrm{v}}(\mu + \delta\eta_t) = \mu T_y - \mu^2\delta\eta_x T_x\,. \tag{B.30c}$$

$$T_y + \mu\delta\eta_x T_x = \hat{j}(x,t) \tag{B.30d}$$

$$r_\rho\mathrm{Le}\,\mathrm{Pe}\,\bar{\mathrm{v}}\left(\mu + \delta\eta_t\right)c = -\mu c_y + \mu^2\delta c_x\eta_x\,. \tag{B.30e}$$

$$\left(\mu + \delta\eta_t\right)c = -\mu\frac{\mathcal{S}}{\mathrm{Le}}\left(c_y - \mu\delta c_x\eta_x\right)\,. \tag{B.30f}$$

The full model is has five variables, five governing equations and eleven boundary conditions. These dynamics happen at two radically different time-scales, and length-scales, which necessitates careful treatment in the analysis carried out in Chapter 2.

Bibliography

[1] J. Ladan and S.W. Morris. Experiments on the dynamic wetting of growing icicles. *New Journal of Physics*, 23(12):123017, December 2021.

[2] J. Ladan and S.W. Morris. Pattern of inclusions inside rippled icicles. *Physical Review E*, 106(5):054211, November 2022.

[3] Masoud Farzaneh, editor. *Atmospheric Icing of Power Networks*. Springer, Dordrecht, 2008.

[4] O. Gohardani, editor. *Progress in Aircraft Icing and Aircraft Erosion Research*. Aerospace and System Engineering and Research. Nova Science Publishers, 2017.

[5] K. Szilder, S. Mcilwain, and E.P. Lozowski. Numerical Simulation of Complex Ice Shapes on Swept Wings. *ICAS-Secretariat - 25th Congress of the International Council of the Aeronautical Sciences 2006*, 3, January 2006.

[6] T. Rashid, H. A. Khawaja, and K. Edvardsen. Review of marine icing and anti-/de-icing systems. *Journal of Marine Engineering & Technology*, 15(2):79–87, May 2016.

[7] L. Makkonen. Surface Melting of Ice. *The Journal of Physical Chemistry B*, 101(32):6196–6200, August 1997.

[8] L. Makkonen. Modeling power line icing in freezing precipitation. *Atmospheric Research*, 46(1-2):131–142, April 1998.

[9] G.B. Lesins and R. List. Sponginess and Drop Shedding of Gyrating Hailstones in a Pressure-Controlled Icing Wind Tunnel. *Journal of the Atmospheric Sciences*, 43(23):2813–2825, December 1986.

[10] R.D. Adams-Selin and C.L. Ziegler. Forecasting Hail Using a One-Dimensional Hail Growth Model within WRF. *Monthly Weather Review*, 144(12):4919–4939, August 2016.

[11] L. Makkonen. A Model of Icicle Growth. *Journal of Glaciology*, 34(116):64–70, 1988/ed.

[12] A. Chen and S.W. Morris. On the origin and evolution of icicle ripples. *New Journal of Physics*, 15(10):103012, October 2013.

[13] D.L. Feltham, N. Untersteiner, J.S. Wettlaufer, and M.G. Worster. Sea ice is a mushy layer. *Geophysical Research Letters*, 33(14), 2006.

[14] K.K. Chung and E.P. Lozowski. On the growth of marine icicles. *Atmosphere-Ocean*, 28(4):393–408, December 1990.

[15] L. Makkonen. Salinity and growth rate of ice formed by sea spray. *Cold Regions Science and Technology*, 14(2):163–171, August 1987.

[16] M. G. Worster and J. S. Wettlaufer. Natural Convection, Solute Trapping, and Channel Formation during Solidification of Saltwater. *The Journal of Physical Chemistry B*, 101(32):6132–6136, August 1997.

[17] E.P. Lozowski, K. Szilder, and L. Makkonen. Computer simulation of marine ice accretion. *Philosophical Transactions of the Royal Society of London. Series A: Mathematical, Physical and Engineering Sciences*, 358(1776):2811–2845, November 2000.

[18] N. Maeno and T. Takahashi. Studies on icicles. II. Wave-forms, spikes and bent icicles. *IJIW Temp. Sci., Ser. A*, 43:139–147, 1984.

[19] N. Maeno, L. Makkonen, K. Nishimura, K. Kosugi, and T. Takahashi. Growth rates of icicles. *Journal of Glaciology*, 40(135):319–326, 1994/ed.

[20] A. Chen. *Experiments on the Growth and Form of Icicles.* PhD thesis, The University of Toronto, The Dept. of Physics, 60 St George St., Toronto ON, Canada, M5S 1A7, 2013.

[21] P. W. Atkins. *Atkins' Physical Chemistry / Peter Atkins, Julio de Paula.* W. H. Freeman and Co., New York, 9th ed. edition, 2010.

[22] R. F. Sekerka. A Stability Function for Explicit Evaluation of the Mullins-Sekerka Interface Stability Criterion. *Journal of Applied Physics*, 36(1):264–268, January 1965.

[23] J. S Wettlaufer. Directional Solidification of Salt Water: Deep and Shallow Cells. *Europhysics Letters (EPL)*, 19(4):337–342, June 1992.

[24] L. Makkonen. Solid fraction in dendritic solidification of a liquid. *Applied Physics Letters*, 96(9):091910, March 2010.

[25] N. Ogawa and Y. Furukawa. Surface Instability of Icicles. *Physical Review E*, 66(4):041202, October 2002.

[26] K. Ueno. Pattern formation in crystal growth under parabolic shear flow. *Physical Review E*, 68(2):021603, August 2003.

[27] K. Ueno. Pattern formation in crystal growth under parabolic shear flow. II. *Physical Review E*, 69(5):051604, May 2004.

[28] K. Ueno. Characteristics of the wavelength of ripples on icicles. *Physics of Fluids*, 19(9):093602, September 2007.

[29] K. Ueno and M. Farzaneh. Linear stability analysis of ice growth under supercooled water film driven by a laminar airflow. *Physics of Fluids*, 23(4):042103, April 2011.

[30] K. Ueno, M. Farzaneh, S. Yamaguchi, and H. Tsuji. Numerical and experimental verification of a theoretical model of ripple formation in ice growth under supercooled water film flow. *Fluid Dynamics Research*, 42(2):025508, April 2010.

[31] K. Ueno and M. Farzaneh. Morphological instability of the solid-liquid interface in crystal growth under supercooled liquid film flow and natural convection airflow. *Physics of Fluids*, 22(1):017102, January 2010.

[32] K. Ueno and M. Farzaneh. Roughness characteristics of an ice surface grown in the presence of a supercooled water film driven by gravity and wind drag. *arXiv:1103.4141 [physics]*, March 2011.

[33] M. Yokokawa, N. Izumi, K. Naito, G. Parker, T. Yamada, and R. Greve. Cyclic steps on ice. *Journal of Geophysical Research: Earth Surface*, 121(5):1023–1048, May 2016.

[34] C. Camporeale and L. Ridolfi. Hydrodynamic-Driven Stability Analysis of Morphological Patterns on Stalactites and Implications for Cave Paleoflow Reconstructions. *Physical Review Letters*, 108(23):238501, June 2012.

[35] T. Terada. *Collected Essays of Torahiko Terada*. Iwanami, Tokyo, 1947.

[36] H. Hatakeyama and S. Nemoto. A Note on the Formation of Horizontal Stripes on Icicle. *Geophysical Magazine*, 28:479–484, 1958.

[37] R.A. Laudise and R.L. Barns. Are icicles single crystals? *Journal of Crystal Growth*, 46(3):379–386, March 1979.

[38] C.A. Knight. Icicles as crystallization phenomena. *Journal of Crystal Growth*, 49(1):193–198, May 1980.

[39] I.W. Geer. The Not-So-Ordinary Icicle. *Weatherwise*, 34(6):257–259, December 1981.

[40] N. Maeno and T. Takahashi. Studies on icicles. I. General aspects of the structure and growth of an icicle. *Low Temperature Science*, 43:125–138, 1984.

[41] J. Walker. The Amateur Scientist: Icicles ensheathe a number of puzzles: Just how does the water freeze? *Scientific American*, 258(5):114–117, 1988.

[42] K. Johnson and E.P. Lozowski. The simulation of experimental fresh water icicle growth with a simple numerical model. *Proc. IAHR Ice Syrup*, pages 425–435, 1988.

[43] K. Szilder and E. P. Lozowski. An analytical model of icicle growth. *Annals of Glaciology*, 19:141–145, 1994/ed.

[44] M. B. Short, J. C. Baygents, and R. E. Goldstein. A free-boundary theory for the shape of the ideal dripping icicle. *Physics of Fluids*, 18(8):083101, August 2006.

[45] A. Chen and S.W. Morris. Experiments on the morphology of icicles. *Physical Review E*, 83(2):026307, February 2011.

[46] J. A. Neufeld, Raymond E. Goldstein, and M.G. Worster. On the mechanisms of icicle evolution. *Journal of Fluid Mechanics*, 647:287–308, March 2010.

[47] M.B. Bertagni. *Linear and Weakly Nonlinear Analyses of Morphological Patterns*. PhD thesis, Politecnico di Torino, 2019.

[48] J.G. Dash, A.W. Rempel, and J.S. Wettlaufer. The physics of premelted ice and its geophysical consequences. *Reviews of Modern Physics*, 78(3):695–741, July 2006.

[49] M. G. Worster. The Dynamics of Mushy Layers. In S. H. Davis, H. E. Huppert, U. Müller, and M. G. Worster, editors, *Interactive Dynamics of Convection and Solidification*, NATO ASI Series, pages 113–138. Springer Netherlands, Dordrecht, 1992.

[50] J. Ladan. Icicle ripples: Toward a model with impurities. *14th International conference on the physics and chemistry of ice*, 2018.

[51] R.V. Craster and O.K. Matar. Dynamics and stability of thin liquid films. *Reviews of Modern Physics*, 81(3):1131–1198, August 2009.

[52] S. Kalliadasis. *Falling Liquid Films*. Applied Mathematical Sciences, 176. Springer London, London, 1st ed. 2012. edition, 2012.

[53] P.K. Kundu. *Fluid Mechanics*. Elsevier Academic Press, Amsterdam ;, 3rd ed. edition, 2004.

[54] D. J. Acheson. *Elementary Fluid Dynamics*. Oxford Applied Mathematics and Computing Science Series. Clarendon Press, Oxford, 1990.

[55] S.H. Davis. *Theory of Solidification*. Cambridge University Press, first edition, October 2001.

[56] M. Abramowitz and I. A. Stegun. *Handbook of Mathematical Functions with Formulas, Graphs, and Mathematical Tables*. United States National Bureau of Standards. Applied Mathematics Series, 55. Washington U.S. Government Print. Off., Washington, DC, 1965.

[57] C. Camporeale and L. Ridolfi. Ice ripple formation at large Reynolds numbers. *Journal of Fluid Mechanics*, 694:225–251, March 2012.

[58] P. Huerre and P.A. Monkewitz. Local and Global Instabilities in Spatially Developing Flows. *Annual Review of Fluid Mechanics*, 22(1):473–537, 1990.

[59] P. J. Schmid. *Stability and Transition in Shear Flows*. Number 142 in Applied Mathematical Sciences. Springer-Verlag, New York, 2001.

[60] A.O.P. Chiareli and M.G. Worster. Flow focusing instability in a solidifying mushy layer. *Journal of Fluid Mechanics*, 297:293–305, August 1995.

[61] J. A. Neufeld and J. S. Wettlaufer. An experimental study of shear-enhanced convection in a mushy layer. *Journal of Fluid Mechanics*, 612:363–385, October 2008.

[62] M. G. Worster. Instabilities of the liquid and mushy regions during solidification of alloys. *Journal of Fluid Mechanics*, 237:649–669, April 1992.

[63] L. Makkonen. Comments on "A Method for Rescaling Humidity Sensors at Temperatures Well below Freezing". *Journal of Atmospheric and Oceanic Technology*, 13(4):911–912, August 1996.

[64] S. van der Walt, J. L. Schönberger, J. Nunez-Iglesias, F. Boulogne, J. D. Warner, N. Yager, E. Gouillart, and T. Yu. Scikit-image: Image processing in Python. *PeerJ*, 2:e453, June 2014.

[65] P. Virtanen, R. Gommers, T. E. Oliphant, M. Haberland, T. Reddy, D. Cournapeau, E. Burovski, P. Peterson, W. Weckesser, J. Bright, S. J. van der Walt, M. Brett, J. Wilson, K. J. Millman, N. Mayorov, A. R. J. Nelson, E. Jones, R. Kern, E. Larson, C. J. Carey, I. Polat, Y. Feng, E. W. Moore, J. VanderPlas, D. Laxalde, J. Perktold, R. Cimrman, I. Henriksen, E. A. Quintero, C. R. Harris, A. M. Archibald, A. H. Ribeiro, F. Pedregosa, P. van Mulbregt, and SciPy 1.0 Contributors. SciPy 1.0: Fundamental algorithms for scientific computing in python. *Nature Methods*, 17:261–272, 2020.

[66] R. Sjöback, J. Nygren, and M. Kubista. Absorption and fluorescence properties of fluorescein. *Spectrochimica Acta Part A: Molecular and Biomolecular Spectroscopy*, 51(6):L7–L21, June 1995.

[67] M. Marcellini, C. Noirjean, D. Dedovets, J. Maria, and S. Deville. Time-Lapse, in Situ Imaging of Ice Crystal Growth Using Confocal Microscopy. *ACS Omega*, 1(5):1019–1026, November 2016.

[68] A. Monier, A. Huerre, C. Josserand, and T. Séon. Freezing a rivulet. *Physical Review Fluids*, 5(6):062301, June 2020.

[69] A. Marmur. Wetting on hydrophobic rough surfaces:? To be heterogeneous or not to be? *Langmuir : the ACS journal of surfaces and colloids*, 19(20):8343–8348, 2003.

[70] D. Bonn, J. Eggers, J. Indekeu, J. Meunier, and E. Rolley. Wetting and spreading. *Reviews of Modern Physics*, 81(2):739–805, May 2009.

[71] Y. Nagata, T. Hama, E. H. G. Backus, M. Mezger, D. Bonn, M. Bonn, and G. Sazaki. The Surface of Ice under Equilibrium and Nonequilibrium Conditions. *Accounts of Chemical Research*, 52(4):1006–1015, April 2019.

[72] V. F. Petrenko and R. W. Whitworth. *Physics of Ice*. Oxford University Press, Oxford, 2002.

[73] J. S. Wettlaufer. Impurity Effects in the Premelting of Ice. *Physical Review Letters*, 82(12):2516–2519, March 1999.

[74] J. Schindelin, I. Arganda-Carreras, E. Frise, V. Kaynig, M. Longair, T. Pietzsch, S. Preibisch, C. Rueden, S. Saalfeld, B. Schmid, J. Tinevez, D. J. White, V. Hartenstein, K. Eliceiri, P. Tomancak, and A. Cardona. Fiji: An open-source platform for biological-image analysis. *Nature Methods*, 9(7):676–682, July 2012.

[75] W. F. Weeks and G. Lofgren. The Effective Solute Distribution Coefficient During the Freezing of NaCl Solutions. In *Physics of Snow and Ice*, volume 1(1), pages 579–597, Sapporo, Japan, 1967.

[76] J. S. Wettlaufer and M. G. Worster. Dynamics of premelted films: Frost heave in a capillary. *Physical Review E*, 51(5):4679–4689, May 1995.